TECHNISCHE UNIVERSITÄT MÜNCHEN

Lehrstuhl für Hochfrequenztechnik

Analysis and Design of Open Periodic Metamaterials

Sakineh Tooni

Vollständiger Abdruck der von der Fakultät für Elektrotechnik und Informationstechnik der Technischen Universität München zur Erlangung des akademischen Grades eines

- *Doktor-Ingenieurs* -

genehmigten Dissertation

Vorsitzender: 1. Prof. Dr.-Ing. Norbert Hanik

Prüfer der Dissertation: 1. Prof. Dr.-Ing. Thomas Eibert

2. Prof. Dr.-Ing. Volkert Hansen

Die Dissertation wurde am 27.04.2016 bei der Technischen Universität München eingereicht und durch die Fakultät für Elektrotechnik und Informationstechnik am 12.07.2016 angenommen.

Acknowledgement

First and foremost, I would like to express my sincere appreciate to my supervisor Prof. Dr. Ing. Thomas Eibert for providing the opportunity to conduct this work and for his continuous support and advice. The completion of this work would not have been possible without the support and encouragements I received from him. I thank Dr. Larissa Vietzorreck who helped me by reviewing the papers, scientific discussions and critical comments. I would also like to thank the members of the examining committee, Prof. Volkert Hansen and Prof. Hanik for dedicating their valuable time for reviewing this thesis. Part of my thesis was supported by DAAD and a part of the work was supported by Technical University of Munich. I would like to appreciate the efforts of these organizations for their invaluable supports.

I would also like to thank my brother and my sisters, they were always supporting me and encouraging me with their best wishes. The last but not least, I wish to express my deepest thanks to my parents. Their unconditional love and support, which cannot be put into words are always the source of hope and inspiration for me.

Contents

List of Abbreviations

ABC	Absorbing boundary condition
AMC	Artificial magnetic conductor
BI	Boundary integral
BVP	Boundary value problem
CFIE	Combined field integral equation
CMP	Characteristic material parameter
CRLH	Composite right/left handed
CST MWS	Computer simulation technology microwave studio
EBG	Electromagnetic band gap
EFIE	Electric field integral equation
ELC	Electric (LC) resonator
EMP	Effective material parameter
ENZ	Epsilon near zero
FDFD	Finite difference frequency domain
FDTD	Finite difference time domain
FEM	Finite element method
FEBI	Finite element boundary integral
HFSS	High frequency structure simulator
HIS	High impedance surface
IE	Integral equation
LHM	Left hand material
MFIE	Magnetic field integral equation
MNZ	μ near zero
MoM	Method of moment
NR	Newton Raphson
NM	Nelder Mead
OBC	Open boundary condition
PBC	Periodic boundary condition
PEC	Perfect electric conductor
PMC	Perfect magnetic conductor
PML	Perfectly matched layer
pv	Caushy principal value
RHM	Right hand material
RWG	Rao Wilton Glisson
SLP3	Sturm Liouville problem type 3
SMA	Scattering matrix approach
SNG	Single negative

SRR	Split ring resonator
TE	Transverse electric
TEM	Transverse electromagnetic
TLM	Transmission line method
TM	Transverse magnetic

List of symbols

a	Inward normalized complex power wave amplitude
b	Outward normalized complex power wave amplitude
$\boldsymbol{B}$	Magnetic flux density
C	Capacitance
$\boldsymbol{D}$	Electric displacement vector
$\boldsymbol{E}$	Electric field intensity
G	Scalar Green's function
$\boldsymbol{H}$	Magnetic field intensity
$\Im$	Imaginary part
$\boldsymbol{J}$	Electric current density
$\boldsymbol{J}_s$	Electric surface current density
$\boldsymbol{k}$	propagation wave vector
L	Inductance
$\boldsymbol{M}$	Magnetic current density
$\boldsymbol{M}_s$	Magnetic surface current density
$\boldsymbol{n}$	Unit normal vector
N_{eff}	Effective refractive index
p	Period or periodical length
R	reflection coefficient
$\boldsymbol{r}$	Position vector
$\Re$	Real part
$\mathbb{R}$	Real numbers
$\boldsymbol{S}$	Poynting vector
S_{ij}	scattering parameter, relation between inward wave at port j to outgoing wave at port i
T	Transmission coefficient
T_{matrix}	Transfer matrix
x^*	Conjugate complex of a number x

Y	Admittance
Z	Impedance
Z_{eff}	Effective wave impedance
α	Attenuation constant
$\boldsymbol{\alpha}$	Whitney edge element basis function
β	Phase constant
$\boldsymbol{\beta}$	RWG basis function
δ	Dirac impulse, delta function distribution
ε_0	$= 8.85 \cdot 10^{-12} As/(Vm)$, Permittivity of free space
$\mathbf{\Phi}$	Eigenmode vector basis function
γ	Propagation constant
λ	Wavelength
μ_0	$= 4\pi \cdot 10^{-7}$, Permeability of free space
ρ_e	Electric charge density
ρ_m	Magnetic charge density
σ	Electric conductivity
$\text{Sgn}(\cdot)$	Signum function
ω	Angular frequency
ω_p	Plasma angular frequency
ω_{0m}	Magnetic resonance angular frequency
ψ	Eigenmode scalar basis function
ζ	Dissipation factor
∇	Nabla operator, gradient
$\nabla\cdot$	Divergence operator
$\nabla\times$	Curl operator
$\Delta = \nabla^2$	Laplace operator

1. Abstract

The main goal of this thesis is to extend the numerical methods for analyzing general open periodic structures both in the radiation and scattering states. Especially, metamaterials made up of subwavelength constructing unit cells are investigated in order to study the electromagnetic wave manipulation with the inhomogeneous periodic structures.

The work is started by studying the basic definition of metamaterial and initial realization of the desired dispersive features by using metamaterials properties. Ranging from low frequencies up to the light frequencies and for the applications of dispersive media we seek a mathematical and physical explanation of metamaterials. Therefore, understanding the wave behavior in dispersive structures is the first step in the field of metamaterials. Since metamaterials can be designed to show the desired dispersion in arbitrary frequency bands, there are a variety of applications for these artificial structures like as flat lenses for evanescent wave enhancement and subwavelength super resolution focusing. Using metamaterials, below cutoff waveguide and beam steering leaky wave antennas could be presented in a new paradigm. Moreover, decoupling of the antenna elements over an artificial ground as well as enhancing the gain of resonant antennas by eliminating surface waves of the substrate have been introduced. However, still there are plenty of other properties that cannot be easily explained based on the material properties and demand a more accurate method.

Since realizing these structures is performed by using subwavelength unit cells in periodic arrangement, source free eigenproblems are among the most efficient asserted methods to analyze their properties. However, treating eigenvalue computations in periodic structures is usually complicated. Moreover, including open boundaries in periodic structures will add more challenges due to nonlinearity of the dispersion equation.

The most recent numerical methods based on the moment method decomposition of the unit cells are generally restricted to periodic Green's function computations of the unit cell. In this thesis it is tried to pave a way to explain some scattering phenomena from metanaterials in the spectral domain.

2. introduction

2.1. Background

By introducing the negative permittivity and negative permeability to the classic Maxwell's equations by Russian physicist Victor Veselago in 1967 [Veselago and Narimanov, 2006], some fascinating wave propagation effects could be observed and explained more feasibly. The first deduction of the negative index material is the negative phase velocity of a monochromatic propagating plane wave, which describes the propagation of the wave fronts in a group, is opposite to the energy flux direction represented by Poynting vector. However, until 30 years the concept was discussed only in theory. In 2001, a group of physicists [Shelby et al., 2001b] could realize the negative refractive index in microwave frequencies by employing the combination of two types of microwave electric and magnetic resonators placed in a periodic arrangement. The idea was originating from the introducing extra ordinary permeability by using non-magnetic resonant particles [Pendry et al., 1999] together with the introduced plasma like behavior of closely placed square array of wires [Pendry et al., 1996]. Combining these two particles in different configurations results in the negative refractive index materials known as left handed materials [Smith et al., 2000b, Shelby et al., 2001a]. Also, epsilon near zero (ENZ) materials first introduced in [Silveirinha and Engheta, 2006] and μ near zero (MNZ) materials [Engheta et al., 2006, Sihvola et al., 2007] are the other interesting behaviors of metamaterials as bulk material properties.

The most important feature of metamaterials is their dispersive behavior. From the entropy condition, it is shown that the left handed media have to be dispersive to keep the condition [Caloz and Itoh, 2005]. From the continuity of the tangential fields at the boundary of two media, it is concluded that normal component of the Poynting vector is continuous. On the other hand, the tangential component of the Poynting vector is not affected by the dispersivity of the media. Therefore, the time expression for the Poynting vector is held in general dispersive media. By taking the time average of the divergence of the Poynting vector, the rate of change of the energy per volume in a desired volume is computed. For fields whose amplitude varies sufficiently slowly with time, it has been shown that by some approximations in the left handed media

the stored energy is resulting in that the left handed medium is necessarily dispersive. This feature helps to design new devices based on the dispersion engineering of metamaterials.

In physics, it is tried to explain the behavior of this so called metamaterials as bulk materials by extracting the material properties using the scattered field. While, in engineering the macroscopic behavior of the metamaterials are more interesting. Therefore, the equivalent circuit models were realized by lumped elements to imitate the dispersion properties of the metamaterials [Caloz and Itoh, 2004]. Implementation of metamaterials by lumped or distributed elements resulted in some new planar waveguide structures called composite right left handed (CRLH) transmission lines. These CRLH transmission lines later were extended to bulk 3D metamaterials [Grbic and Eleftheriades, 2005]. The advantage of transmission lines over resonant particles is their broader band widths as well as possible linear dispersion behaviors.

To analyze transmission lines, supposing the periodic repetition of the unit cells, different techniques are employed. Among them, distributed circuits on the microstrip technology are using currents and voltages of the unit cell terminals by transmission line method (TLM) in the time domain [So et al., 2005] or in the frequency domain [Eleftheriades et al., 2002, Caloz and Itoh, 2004, Oliner, 2003] to obtain the dispersion curves. This method is restricted to the fundamental quasi TEM mode of the structures because of the definition of the current and voltage for these modes. Using the scattering parameters could be an alternative to take all the possible excited terminal modes into account which is called scattering matrix approach (SMA) [Valerio et al., 2011, Cao et al., 2002].

In general, to compute the dispersion curves of the transmission lines, the source free waveguide sections are analyzed subjected to the corresponding boundary conditions. The field distribution of eigensolutions, inside the unit cell, is calculated. Afterwards, the eigenvalues of the guiding structures are computed using Bloch theory applied to the terminal's field [Collin, 1991]. Using the Bloch theory, the periodicity is automatically applied to the field values in the terminals. The resulting guided waves are called Bloch modes. This method can be employed for multimode guiding structures in closed boundary waveguides. To employ the Bloch theory for every periodic closed waveguide, the inhomogeneous part of the problem is discretized by using a numerical method, usually finite element (FEM) [Jin, 2014], finite difference time domain (FDTD) [Kunz and Luebbers, 1993], finite difference frequency domain (FDFD) [Xu et al., 2003] and so on. The resulting variational equation together with the periodic boundary condition will make a boundary value problem. In cylindrical waveguides, the field distribution on the port is initially solved as

a 2D eigenproblem and the all possible eigenmodes of the port are computed. Afterwards, these eigenmode field distributions are applied to the internal field problem as the boundary conditions over the port region. The coefficients of every eigenmode are obtained from the final equation together with the corresponding boundaries as a function of the eigenvalue and are known as the scattering parameters. The last step is to assign the periodic boundary condition to the scattering parameters and compute the eigenvalues corresponding to every mode [Bongard et al., 2009].

The Bloch theory will guarantee the exact periodic eigenvalues when the field is expanded based on an infinite number of modes at the terminal. However, it is not possible to take infinite number of modes into account and some truncation errors should be accepted. Moreover, in practical waveguiding applications the first propagating mode is desired for which some first modes are enough to compute the eigenvalues effectively.

The Sturm Liouville problems are the linear eigenvalue problem for differential equations which is equivalent to the solution of Maxwell equations in the source free problem [Felsen and Marcuvitz, 1994]. From the excitation problems, the Green's function is the response of the impulse excitation of a differential equation in the space domain. This excitation problem is solved for a source free region part of the problem and the excitation is considered as a jump condition [Dudley, 1994]. The resulting spectral representation of the point source with closed boundary conditions, Neumann or Dirichlet, is a summation of all possible discrete eigenmodes. For a problem with open boundary conditions, there exist continuous egienmodes in the spectrum and therefore an integral is representing these continuums [Felsen and Marcuvitz, 1994].

In field decomposition problems based on complete entire domain basis, the choice of basis functions is depending on the solution domain and boundary conditions. In closed waveguides, the most feasible solution domain is the waveguide cross section. However, in open traveling wave structures, the waveguide cross section has an infinite domain. Therefore, the modes will have a continuum spectrum besides the possible discrete modes where the continuous part represents the radiation modes [Dudley, 1994]. This continuous part when employed in mode matching techniques will result in Sommerfeld type integral computations which in turn will slow down the computation procedure. To conquer this difficulty, enclosing the open boundary with reflection less boundary conditions in a way that the field distribution of the guided modes and therefore corresponding eigenvalues are not affected strongly is an alternative [Derudder et al., 2001a]. The perfectly matched layers (PML)are one group of reflection less boundary conditions [Gedney, 1996]. Physically, PMLs are realized as layers of uniaxially anisotropic media. To terminate the thickness of

the absorbing layer, PML is backed by a perfectly electric conductor. Yet this termination yields some reflections. To avoid these reflections, a small amount of loss is added to the PML layer. The mathematical interpretation of PMLs might be better explained by complex coordinate stretching [Chew et al., 1997, Chew and Weedon, 1994]. In this presentation, the finite dimensions of the PML are transformed into a complex coordinate to imitate the absorption.

Employing the PML layers to terminate the open boundary in layered media will discretize the branch line in spectral domain Green's function such that the radiation part of the spectrum can be represented as a summation of complex eigenmodes called quasi leaky modes [Olyslager, 2004]. These leaky modes are more concentrated inside the layered waveguide. In addition to the leaky modes, another type of complex modes called Berenger modes will arise because of PML layer. These modes are more concentrated inside the PML layer. Therefore, it is possible to use finite number of discrete leaky and Berenger modes to approximate the field distribution in an open waveguide port.

The most effective numerical technique to model the open boundaries in scattering and radiation problems is utilizing the integral equation based methods over the open boundary. These so called boundary integral (BI) methods are modeling the equivalent source current utilizing the equivalent principle [Harrington and Harrington, 1996]. These integral equation (IE) methods are solved by the method of moment and the advantage of them over differential methods is that they automatically incorporate the radiation condition. Therefore, despite the finite element method (FEM) and finite difference time domain (FDTD), IEs do not require absorbing boundary conditions. To incorporate the radiation condition through the Sommerfeld radiation condition, an appropriate Green's function is used in the integral equation. The disadvantage of IE methods is the difficulty of their implementation into the complex objects besides the full matrix production whose treatment requires large storage and computation time. To overcome these disadvantages, a hybrid method of the combination of FEM and IE has been developed [Silvester and Hsieh, 1971]. This hybrid method is called finite element boundary integral (FEBI) method and make use of the advantage of FEM to model inhomogeneities and having sparse matrices as well as the advantage of IE to satisfy the radiation condition effectively.

FEM methods are usually developed in frequency domain therefore more appropriate for eigenvalue computation and waveguide applications. On the other hand, IE methods are more appropriate for excitation based open problems like as scattering problems. In this thesis, it is tried to use the excitation to compute for eigenvalues in open structures in periodic stratified media. Therefore, the concept of eigenvalues in open periodic stratified media is demanded to be

developed. In this purpose, the theory of Green's function for layered media is employed to extract the eigenvalues and eigenmodes for infinite 2D periodic media.

2.2. Motivation

Concealing scatterers by making them invisible to an external electromagnetic detector using the compensation of the scattered field is known as cloaking [Pendry et al., 2008]. Beyond the scattering suppression application, the scattering free sensors and detectors are also among the devices which may serve as the realization of metamaterial cloaks. Ranging from microwaves and millimeter waves to terahertz and optical frequencies, the cloaking devices and absorbers are widely investigated [Alu and Engheta, 2008, Schurig et al., 2006a, Engheta, 2002b]. The main endeavor in these designs is to realize cloaking by isotropic lossless structures.

Some other interesting applications of open metamaterials are in leaky wave antennas for the continuous beam steering in the whole spatial angle, high impedance surfaces (HIS) for resonant antenna substrates to remove undesired surface wave modes and improving the antenna functionality, super resolution near field imaging devices and etc.

The popularity of metamaterial applications motivated us to find an efficient method to analyze and explain some physical behaviors of 2D periodic structures. Especially, the focus in this thesis is on the scattering from subwavelength unit cells to solve for the eigenproblem in periodic configurations. In comparison to mathematical eigenvalue computation methods, the introduced method in this thesis is excitation of eigenmodes using physical behavior of the open resonators which eliminates the mathematical eigenvalue decomposition complexities of conventional methods. There are two general methods of excitation, internal excitation and external excitation methods depending on the location of the exciting source. In this thesis, plane waves are employed to model the external excitation of a spectral impulse function suited for eigenvalue sweeping.

2.3. Organization

In this work, after the introduction of metamaterials, a brief review over the previous methods of modeling of metamaterials and dispersion engineering using these materials is given. In chapter 4, the Bloch method for closed structures is employed to extract the eigenvalues of one unit cell in a periodic ar-

rangement. The behavior of complex modes in closed structures is investigated and it is shown that these modes do not carry any net power along the waveguide. The effect of higher order modes over the fundamental propagating mode is taken into account by considering the highest possible number of eigenvectors over the terminals of the unit cell. The method of scattering matrix is then extended to open waveguides by enclosing them using PML layers. The transformation of the continuous spectrum to discrete modes is investigated in the following and it is demonstrated that the modal decomposition in open structures can be performed by accepting some approximations.

To compute the eigenvaleus of open structures more accurate, the boundary integral technique is employed to model the radiation condition efficiently. In chapter 5, the hybrid finite element boundary integral method is explained mathematically and the scattered field yielded from the equivalent surface current through the Huygens principle is computed. In order to implement periodic boundary conditions, the 2D periodic Green's function of free space is considered over the open boundary, while the periodicity in finite element part is considered as the complex phase shifts along the unit cell on the parallel edge walls over corresponding mesh cells.

In the following, in chapter 6, the Sturm Liouville problems as the connection between the eigenvalue problem (oscillatory response of the problem without excitation) and the Green's function (excited travelling wave response of the problem) are reviewed. The approximation of periodic subwavelength structures as homogeneous layered media are explored and the singularities of the Green's function of layered media are computed by the excitation method. The method is examined for homogeneous slab waveguides and the properties of the complex leaky modes as well as real surface wave modes are investigated.

In chapter 7, the method of excitation of eigenvalues is inspected for periodic structures. Moreover, the other fascinating behaviors of the scattered field from periodic loss less structures are studied. The proper and improper behavior of the complex modes in the fast wave region of the dispersion diagram for right handed and left handed modes is explained explicitly in this chapter.

3. Metamaterials

The term metamaterial refers to artificial materials exhibiting some extraordinary behaviors in the presence of electromagnetic waves. The initial introduction into these materials by Veselago [Veselago, 1968], conceptually considered homogeneous materials with negative ε and negative μ to make a left handed material (LHM). The direct consequence of LHMs is the opposite direction of phase and group velocities which stimulates some fascinating applications like as

- Reversal of Doppler effect,
- Reversal of the Vavilov-Cerenkov radiation,
- Negative refractive index at the interface between a right handed medium (RHM) and a LHM,
- Perfect lens behavior of a slab with refractive index $n = -1$,

and some other fundamental phenomena like necessary frequency dispersion of constitutive material parameters to keep the entropy condition, plasmonic expressions of the constitutive parameters in resonant type LH media and so on. Metamaterials, based on their effective bulk material properties for the time dependence $\mathrm{e}^{-\mathrm{j}\omega t}$, are categorized into four general categories, Fig. 3.1.

3.1. Electromagnetic parameter retrieval in homogeneous slabs

Practical metamaterials are made up of periodic arrangement of inclusions with the unit cell dimensions less than a quarter of the operating wavelength therefore they are not originally continuous media. Henceforth, defining the material properties for these structures can be interpreted with two concepts. The conventional method of effective material parameters (EMP) and an alternative concept of characteristic material parameters (CMP) will describe the behavior of metamaterials [Simovski, 2011]. The CM parameters are independent of the external sources and therefore do not depend on the electromagnetic

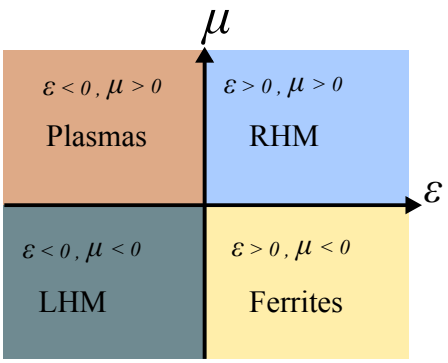

Figure 3.1.: Permittivity – permeability ($\varepsilon - \mu$) diagram.

field distribution in the material sample. However, EMP are retrieved from the reflection and transmission of plane waves, Scattering S-parameters, from the homogeneous slabs of material. The procedure of introducing material parameters to the media of particles is called homogenization. In this approach the sample formed by an array of artificial particles in the dielectric matrix is replaced by a body of the same shape and size filled with uniform continuous magneto-dielectric medium with unknown ε and μ. These two complex quantities are then retrieved from S-parameters at a specific angle of the wave incidence and polarization. These quantities are apparently applicable only to the same case of the wave incidence in which they were retrieved. In 2005, Smith introduced a method to retrieve EMP for slabs of materials [Smith et al., 2005]. This theory replaces the electromagnetic response of the complicated metamaterial structure with the electromagnetic response of a homogeneous isotropic or anisotropic slab.

To model metamaterials by full wave methods, the unit cell of the 3D periodic metamaterial can be treated as a two-port structure with incoming and outgoing waves, the amplitudes of which are related to each other by the scattering matrix. The fundamental mode in the ports is the TEM-mode, equivalent to a plane wave illuminating the structure. This so-called scattering matrix approach (SMA) is very often used in the retrieval process for effective material parameters. To imitate the TEM behavior of the incident wave in a single unit cell of a 3D periodic structure, the PEC/PMC boundary condition can be employed as shown in Fig. 3.2.

The mathematical solution of this problem is generally not unique. To get a unique solution, physically justified constrains must be imposed. Moreover, the retrieval algorithm has two limitations. In order to determine the real part of

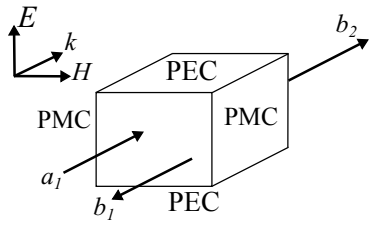

Figure 3.2.: Modeling of a periodic array by simulating of a single unit cell with appropriate excitation and boundary conditions.

the refractive index, a complicated iterative method based on a Taylor series is required. Besides, by imposing the passivity condition, $\Im(\varepsilon) \leqslant 0$ and $\Im(\mu) \leqslant 0$ for time dependency of $\mathrm{e}^{-\mathrm{j}\omega t}$, the method cannot find any effective material parameters for some frequency regions.

To retrieve the effective parameters of the unit cell, the scattering parameters are computed using a full wave solver. As presented in [Smith et al., 2005], for a plane wave with normal incidence on a homogeneous slab, the wave impedance and the refractive index are related to the S-parameters as follows

$$S_{11} = \frac{R_{01}(1 - \mathrm{e}^{\mathrm{j}2N_{\mathrm{eff}}k_0 d_{\mathrm{eff}}})}{1 - R_{01}^2 \mathrm{e}^{\mathrm{j}2N_{\mathrm{eff}}k_0 d_{\mathrm{eff}}}}, \tag{3.1}$$

$$S_{21} = \frac{(1 - R_{01}^2)\mathrm{e}^{\mathrm{j}2N_{\mathrm{eff}}k_0 d_{\mathrm{eff}}}}{1 - R_{01}^2 \mathrm{e}^{\mathrm{j}2N_{\mathrm{eff}}k_0 d_{\mathrm{eff}}}}, \tag{3.2}$$

where the reflection coefficient from the slab is expressed based on the complex wave impedance as

$$R_{01} = \frac{Z_{\mathrm{eff}} - 1}{Z_{\mathrm{eff}} + 1}. \tag{3.3}$$

N_{eff} is the complex refractive index, k_0 the free space wavenumber, d_{eff} is the thickness of the slab and ω the angular frequency. Therefore, the effective impedance and complex refractive index can be computed as

$$Z_{\mathrm{eff}} = \pm \sqrt{\frac{(1 + S_{11}^2) - S_{21}^2}{(1 - S_{11}^2) - S_{21}^2}} \tag{3.4}$$

$$N_{\mathrm{eff}} = \frac{1}{k_0 d_{\mathrm{eff}}} \{\Im[\ln(\mathrm{e}^{\mathrm{j}N_{\mathrm{eff}}k_0 d_{\mathrm{eff}}})] + 2m\pi - \mathrm{j}\Re[\ln(\mathrm{e}^{\mathrm{j}N_{\mathrm{eff}}k_0 d_{\mathrm{eff}}})]\}. \tag{3.5}$$

To assign the sign of Z_{eff} and choose the correct branch in the logarithm in the formulation of N_{eff} which is determined by m, two physical constraints namely causality and passivity conditions are read as

$$\Im(N_{\text{eff}}) \geqslant 0, \tag{3.6}$$
$$\Im(Z_{\text{eff}}) \geqslant 0. \tag{3.7}$$

The first condition is equivalent to $|\mathrm{e}^{\mathrm{j}N_{\text{eff}}k_0d_{\text{eff}}}| < 1$. Separating the real and imaginary parts of the refractive index yields

$$n_{\text{eff},real} = \frac{\Im[\ln(\mathrm{e}^{\mathrm{j}N_{\text{eff}}k_0d_{\text{eff}}})]}{k_0d_{\text{eff}}} + \frac{2m\pi}{k_0d_{\text{eff}}} = n_{\text{eff}}^0 + \frac{2m\pi}{k_0d_{\text{eff}}} \tag{3.8}$$
$$n_{\text{eff},imag} = \frac{-\Re[\ln(\mathrm{e}^{\mathrm{j}N_{\text{eff}}k_0d_{\text{eff}}})]}{k_0d_{\text{eff}}}. \tag{3.9}$$

As it is seen from (3.9), the imaginary part of the refractive index is not affected by the branches of the logarithmic function. Therefore, it can be calculated without ambiguity. Knowing the imaginary part of the refractive index, one can determine the real part by applying the Kramers-Kronig relation [Szabo et al., 2010]. Moreover, this method enforces the continuity of the refractive index versus frequency.

3.2. Kramers-Kronig relation

For a causal system, the impulse response of the system should have the form of

$$g(t) = \text{sgn}(t)h(t), \tag{3.10}$$

to confirm the existence of the response for $t > 0$ where sgn is the sign function. Fourier transform of this response function results in a convolution in the frequency domain

$$G(\mathrm{j}\omega) = \frac{1}{\mathrm{j}\pi}\text{pv}\int_{-\infty}^{+\infty}\frac{H(\mathrm{j}\omega')}{\omega-\omega'}d\omega'. \tag{3.11}$$

pv is the Cauchy principal value of the integral. Splitting (3.11) into real and imaginary parts results in

$$U(\omega) = \frac{1}{\pi}\mathrm{pv}\int_{-\infty}^{+\infty}\frac{V(\omega')}{\omega-\omega'}d\omega' \tag{3.12}$$

$$V(\omega) = \frac{-1}{\pi}\mathrm{pv}\int_{-\infty}^{+\infty}\frac{U(\omega')}{\omega-\omega'}d\omega', \tag{3.13}$$

and $G(\mathrm{j}\omega) = U + \mathrm{j}V$. Applying this relation which is known as Kramers-Kronig relation to imaginary part of the refractive index yields the continuous and un-ambiguous refractive index. Finally, effective material parameters can be obtained as

$$\varepsilon_{\mathrm{eff}} = \frac{N_{\mathrm{eff}}}{Z_{\mathrm{eff}}}, \tag{3.14}$$

$$\mu_{\mathrm{eff}} = N_{\mathrm{eff}} Z_{\mathrm{eff}}. \tag{3.15}$$

3.3. Parameters of periodic metamaterials

Long after the theoretical introduction to LHM, the first practical implementations of metamaterial were proposed by Pendry's group [Smith et al., 2000a, Shelby et al., 2001b]. This realization of metamaterials was inspired by reducing the plasma frequency of artificial dielectrics in metallic grids [Pendry et al., 1996] giving a negative ε below the plasma frequency somewhere in the gigahertz together with the artificial magnetism introduced by electric conductors [Pendry et al., 1999]. The significant assumption in making these artificial materials is that the dimensions of the resonant inclusions is much smaller than the wavelength such that they can be considered as homogeneous materials. The artificial magnetism arises from the resonant behavior of the inclusions in the presence of electromagnetic field.

Artificial plasma realized by long but closely spaced wires are excited by electric field parallel to the wire. Therefore, the wave propagating through the slab made up of the wires like as shown in Fig. 3.3, will experience a dispersive medium with negative ε in the direction parallel to the wire length. This is because that the polarizability of the wires is only possible along their longitude. The wire medium therefore shows a permittivity in the form of

$$\frac{\varepsilon_z}{\varepsilon_0} = 1 - \frac{\omega_p^2}{\omega^2 + \mathrm{j}\zeta\omega} \tag{3.16}$$

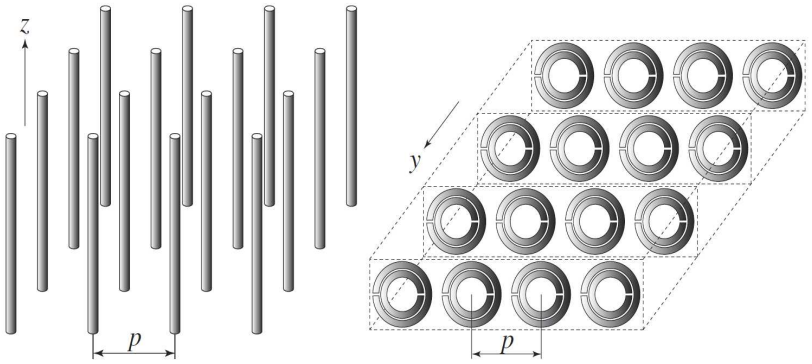

Figure 3.3.: Periodic arrangement of metallic subwavelength inclusions to realize metamaterial, left: negative ε_z, right: negative μ_y.

where ω_p is the plasma frequency which is related to the wire radius and ζ is the dissipation factor depending on the conductivity of the metal [Pendry et al., 1996]. The dispersion relation in (3.16) is known as the Drude dispersion which has no resonant behavior, hence a broad band phenomenon.

To achieve the dispersion behavior of magnetic resonator, the exciting magnetic field has to be perpendicular to the surface of the magnetic resonator. These resonators are generally known as *split ring resonators* (SRR) where they have a split in the metallic ring to realize the resonance. The effective magnetic permeability is as

$$\frac{\mu_y}{\mu_0} = 1 - \frac{F\omega_p^2}{\omega^2 - \omega_{0m}^2 + \mathrm{j}\zeta\omega} \tag{3.17}$$

where ω_{0m} is the resonant frequency of the resulting capacitance due to the splits and the inductance due to the metallic ring [Smith et al., 2000a]. The dispersion relation (3.17) is known as Lorentz dispersion where the negative permeability is achieved for frequencies $\omega_{0m} < \omega < \frac{\omega_{0m}}{\sqrt{1-F}}$ and therefore a narrow band resonant phenomenon. It should be noted that the other material components are the same as the background material.

By this explanation, it is obvious that to obtain the material properties of the periodic inclusions with the aforementioned Kramers-Kronig relations, the orientation of the metallic inclusions in the electromagnetic field is of importance. For transverse electromagnetic (TEM) modes inside a slab of 3D periodic meta-

material, Fig. 3.2 can effectively model the field distribution around one unit cell to obtain the scattering parameters.

The combination of SRR-wire has been extensively utilized to realize negative index materials. This construction is convenient because it is more easy to overlap the narrow band resonant negative permeability of SRR with broadband non-resonant negative permittivity of wire. An alternative artificial electric medium was introduced in [Schurig et al., 2006b] known as electric LC resonator (ELC), in which the resonance of the medium was set by the internal inductance and capacitance of the unit cell. For the unit cells shown in Fig. 3.4, the material parameters are retrieved for TEM incidence with E_z, H_y and propagating in the x direction. Therefore, the computed permittivity is ε_z for electric resonator and the computed permeability is μ_y for magnetic resonator, Fig. 3.6. These resonators have a resonant frequency at 11.4 GHz which can be seen from S-parameters in Fig. 3.5.

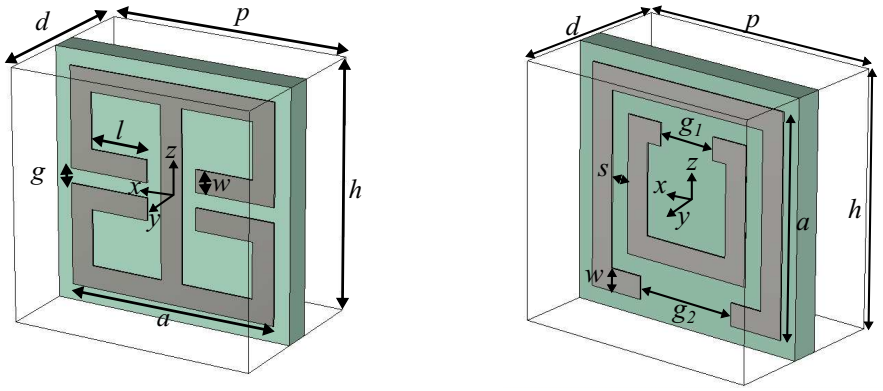

(a) Electric resonator (b) Magnetic resonator

Figure 3.4.: $h = p = \frac{10}{3}$ mm, $d = 2.381$ mm, $w = 0.3$ mm, $s = 0.25$ mm, $l = 0.8$ mm, $a = 2.9$ mm, $g = 0.2$ mm, $g_1 = 0.8$ mm, $g_2 = 1.4$ mm, substrate thickness is 0.381 mm with $\varepsilon_r = 2.33$.

As it is depicted in Fig. 3.6, the ELC unit cell is behaving like as a negative permittivity after the resonant frequency while before the resonant frequency it is a complex valued permittivity and permeability. Also, the SRR shows the negative permeability after its resonant frequency. These resonant particles, which show band stop around their resonant frequencies, are called single negative materials (SNG). As mentioned in this section, the retrieval of material parameters is restricted to the fundamental mode of the guiding medium. On the other hand, most of the resonant particles are very narrow band and it is

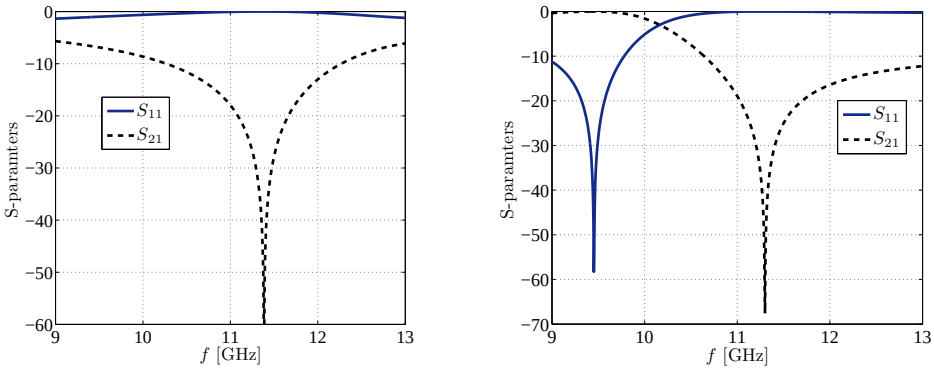

(a) S-parameters of ELC (b) S-parameters of SRR

Figure 3.5.: Amplitude of the scattering parameters of resonators in Fig. 3.4 computed for TEM wave incidence.

very hard to adjust their resonant frequency especially to make LHM from two separate resonators. One of the fascinating applications of the resonant particles is in below cutoff waveguides and cavity miniaturization [Hrabar et al., 2005, Belov and Simovski, 2005].

It can be easily shown that these resonators behave completely different when loaded in below cutoff waveguides and make some pass bands when resonating. These pass bands cannot be explained by material properties anymore. The best to now explanation for these behaviors is computation of dispersion diagram of the constructing unit cell using the image theory of dipoles [Belov and Simovski, 2005, 2006], where every resonator is modeled as an electric or magnetic dipole. However, modeling the resonators with only one polarized dipole in most cases is not possible. Besides, by complicating the resonators configuration, modeling them as single dipoles in not straightforward. The other challenge in the modeling of periodic structures by material properties, is the lack of considering higher order modes which can degrade the behavior of the unit cell even in fundamental TEM mode [Bandlow et al., 2008].

The next section is devoted to the analysis of periodic waveguides by employing the modal decomposition of the field distribution over specific planes transverse to the direction of wave propagation to compute the dispersion properties of periodic structures.

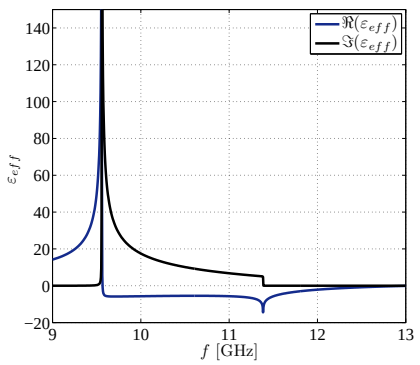

(a) ε_z, ELC

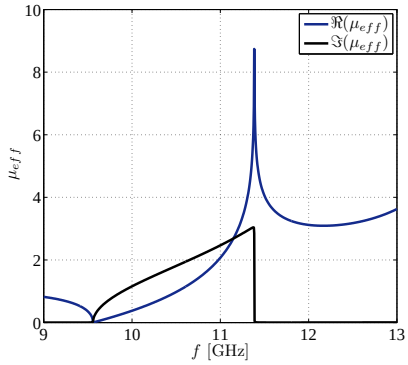

(b) μ_y, ELC

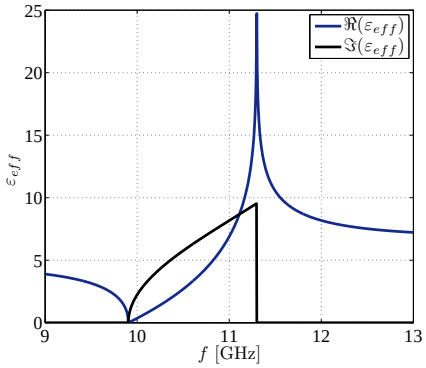

(c) ε_z, SRR

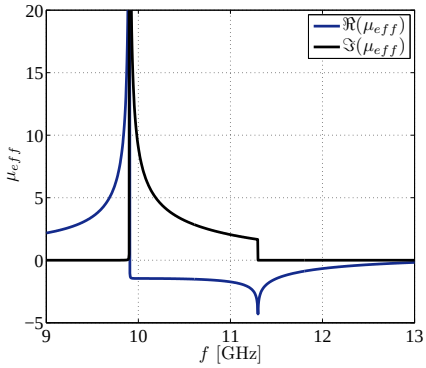

(d) μ_y, SRR

Figure 3.6.: Material parameters of ELC and SRR shown in Fig. 3.4.

4. Closed waveguide structures analysis

Cylindrical waveguides are the basic guiding media in electromagnetics where the cross section of the guiding medium is uniform along the cylinder. To compute the field distribution inside the guided structure, usually modal decomposition of the field is accomplished at a cross section of the waveguide. For homogeneously filled waveguides the field preserves its distribution and only a linear phase shift can represent the traveling behavior of the guided wave. In this case, it is enough to solve the Maxwell's equations only on a reference transversal cross section with closed boundary conditions for transverse geometrical variables, let's say ρ and φ in cylindrical coordinates. The functionality of longitudinal, z, variable is imposed by inspecting the wave propagation as $\mathrm{e}^{-\gamma z}$ from the reference plane with γ the complex wavenumber in the z direction.

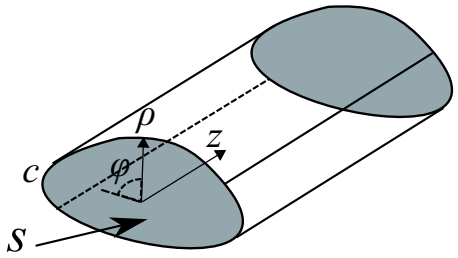

Figure 4.1.: The cylindrical homogeneous waveguide with arbitrary cross section.

Therefore the field is expressed as

$$\boldsymbol{E}(\boldsymbol{\rho}, \varphi, z) = \boldsymbol{E}(\boldsymbol{\rho}, \varphi)\mathrm{e}^{-\gamma z}, \tag{4.1}$$

$$\boldsymbol{H}(\boldsymbol{\rho}, \varphi, z) = \boldsymbol{H}(\boldsymbol{\rho}, \varphi)\mathrm{e}^{-\gamma z}. \tag{4.2}$$

In the absence of the excitation, the vector Helmholtz equation in three dimensions is then converting to a scalar two dimensional equation [Collin, 1991]

$$\nabla_t^2 \psi_h + k^2 \psi_h = 0 \tag{4.3}$$

where ∇_t^2 is the transverse part of ∇^2 and $k^2 = k_0^2 + \gamma^2$ with k_0 the free space wavenumber. The functions $\psi_h \mathrm{e}^{-\gamma z}$ are called modes of the cylindrical waveguide. The number of modes satisfying the homogeneous Helmholtz equation with closed boundary conditions are infinite but countable. Since these modes are countable, they are called discrete modes. These modes make a complete orthogonal set of entire domain basis functions for the transverse cross section with respect to the closed boundary condition. This property can be shown by multiplying (4.3) by a solution function like as ψ_j when the equation is satisfied by ψ_i and vice versa

$$\psi_j \nabla_t^2 \psi_i + (k_0^2 + \gamma_i)\psi_i \psi_j = 0, \tag{4.4}$$
$$\psi_i \nabla_t^2 \psi_j + (k_0^2 + \gamma_j)\psi_j \psi_i = 0. \tag{4.5}$$

Subtracting two equations yields

$$(\gamma_i^2 - \gamma_j^2) \iint\limits_s \psi_i \psi_j ds = \iint\limits_s (\psi_j \nabla_t^2 \psi_i - \psi_i \nabla_t^2 \psi_j) ds = \oint\limits_c \left(\psi_i \frac{\partial \psi_j}{\partial n} - \psi_j \frac{\partial \psi_i}{\partial n} \right) dl, \tag{4.6}$$

where s is the surface of transverse cross section and c is the peripheral of s. By inspecting the Dirichlet or Neumann boundary condition for the field function ψ, the integration over c vanishes. For two different mode functions ψ_i and ψ_j the corresponding wavenumbers γ_i and γ_j are different, consequently, one achieves the orthogonality of two mode functions as

$$\iint\limits_s \psi_i \psi_j ds = 0, \quad i \neq j. \tag{4.7}$$

For degenerate modes, $\gamma_i = \gamma_j$ this procedure needs to take a new subset of modes for ψ_i and ψ_j as $\psi_1' = \psi_i$ and $\psi_2' = \psi_j + \alpha \psi_i$ where α is such that $\iint\limits_s \psi_1' \psi_2' ds = 0$.

However, the above orthogonality property does not satisfy in waveguides with finite conducting walls. The presence of conductivity results in the cross coupling between modes which is considered as attenuation.

For a waveguide with perfectly conducting walls and homogeneously filled, the modes can be categorized into two groups as transverse electric, TE, and transverse magnetic, TM, modes. TE modes have no electric field component along the guiding axis while TM modes have no magnetic field component along the guiding axis. By adding inhomogeneity into the waveguide, the modes

can no longer be separated into TE and TM modes but a linear combination of them. Consequently, a general orthogonality relation must be considered to expand any arbitrary field distribution in a waveguide based on a series of normal modes. This general orthogonal relation follows as a result of the Lorentz reciprocity principle.

Let $\boldsymbol{E}_m$, $\boldsymbol{H}_m$ and $\boldsymbol{E}_n$, $\boldsymbol{H}_n$ be two linearly independent solutions of the Maxwell's equations. It is known that $\nabla \times \boldsymbol{E}_m = -\mathrm{j}\omega\mu\boldsymbol{H}_m$ and $\nabla \times \boldsymbol{E}_n = -\mathrm{j}\omega\mu\boldsymbol{H}_n$. Multiplying two curl equations by $\boldsymbol{H}_n$ and $\boldsymbol{H}_m$ respectively and subtracting them results in

$$\boldsymbol{H}_n \cdot \nabla \times \boldsymbol{E}_m - \boldsymbol{H}_m \cdot \nabla \times \boldsymbol{E}_n = 0. \tag{4.8}$$

Interchanging the electric and magnetic fields yields

$$\boldsymbol{E}_n \cdot \nabla \times \boldsymbol{H}_m - \boldsymbol{E}_m \cdot \nabla \times \boldsymbol{H}_n = 0. \tag{4.9}$$

Adding two equations (4.8) and (4.9) results in

$$\nabla \cdot (\boldsymbol{E}_n \times \boldsymbol{H}_m - \boldsymbol{E}_m \times \boldsymbol{H}_n) = 0. \tag{4.10}$$

Separating the z component of the divergence operator gives

$$\begin{aligned} \nabla \cdot (\boldsymbol{E}_n \times \boldsymbol{H}_m - \boldsymbol{E}_m \times \boldsymbol{H}_n) &= \nabla_t \cdot (\boldsymbol{E}_n \times \boldsymbol{H}_m - \boldsymbol{E}_m \times \boldsymbol{H}_n) \\ &\quad + \boldsymbol{z}\frac{\partial}{\partial z} \cdot (\boldsymbol{E}_n \times \boldsymbol{H}_m - \boldsymbol{E}_m \times \boldsymbol{H}_n) \\ &= \nabla_t \cdot (\boldsymbol{E}_n \times \boldsymbol{H}_m - \boldsymbol{E}_m \times \boldsymbol{H}_n) \\ &\quad - (\gamma_n + \gamma_m)\boldsymbol{z} \cdot (\boldsymbol{E}_n \times \boldsymbol{H}_m - \boldsymbol{E}_m \times \boldsymbol{H}_n). \end{aligned} \tag{4.11}$$

Using the divergence theorem

$$\begin{aligned} \iint_s \nabla_t \cdot (\boldsymbol{E}_n \times \boldsymbol{H}_m - \boldsymbol{E}_m \times \boldsymbol{H}_n) ds &= \oint_c \boldsymbol{n} \cdot (\boldsymbol{E}_n \times \boldsymbol{H}_m - \boldsymbol{E}_m \times \boldsymbol{H}_n) dl \\ &\quad - (\gamma_n + \gamma_m) \iint_s \boldsymbol{z} \cdot (\boldsymbol{E}_{tn} \times \boldsymbol{H}_{tm} - \boldsymbol{E}_{tm} \times \boldsymbol{H}_{tn}) ds. \end{aligned} \tag{4.12}$$

The integration over the contour c enclosing the surface s of the transverse cross section is vanishing due to the perfect conducting walls. Thus one obtains

$$(\gamma_n + \gamma_m) \iint_s \boldsymbol{z} \cdot (\boldsymbol{E}_{tn} \times \boldsymbol{H}_{tm} - \boldsymbol{E}_{tm} \times \boldsymbol{H}_{tn}) ds = 0. \tag{4.13}$$

This equation also holds for imperfect conducting walls by inspecting the impedance boundary condition as $\boldsymbol{E}_t = Z_m \boldsymbol{n} \times \boldsymbol{H}$ which makes the integration over the contour vanishing.

Using the variable separation for transverse components of the field in the form

$$\boldsymbol{H}_{tn} = \boldsymbol{h}_n(\rho,\varphi)\mathrm{e}^{-\gamma_n z}, \tag{4.14}$$
$$\boldsymbol{E}_{tn} = \boldsymbol{e}_n(\rho,\varphi)\mathrm{e}^{-\gamma_n z}, \tag{4.15}$$

where $\boldsymbol{h}_n(\rho,\varphi)$ and $\boldsymbol{e}_n(\rho,\varphi)$ are the transverse vector functions of the transverse field components. Substituting (4.15) and (4.14) into (4.13) results in

$$(\gamma_n+\gamma_m)\iint_s \boldsymbol{z}\cdot(\boldsymbol{e}_n\times\boldsymbol{h}_m-\boldsymbol{e}_m\times\boldsymbol{h}_n)ds=0. \tag{4.16}$$

Moreover, in (4.16), each term vanishes separately. Consider two sets of solutions $\boldsymbol{E}_n$, $\boldsymbol{H}_n$ and $\boldsymbol{E}'_m$, $\boldsymbol{H}'_m$ such that the second set is a back propagating mode with $\mathrm{e}^{\gamma z}$ functionality and $\boldsymbol{E}'_m = \boldsymbol{e}_m\mathrm{e}^{\gamma z}$, $\boldsymbol{H}'_m = -\boldsymbol{h}_m\mathrm{e}^{\gamma z}$. Thus the equation (4.16) for this set becomes

$$(\gamma_n-\gamma_m)\iint_s \boldsymbol{z}\cdot(-\boldsymbol{e}_n\times\boldsymbol{h}_m-\boldsymbol{e}_m\times\boldsymbol{h}_n)ds=0. \tag{4.17}$$

From (4.16) and (4.17) it is concluded that

$$\iint_s \boldsymbol{z}\cdot(\boldsymbol{e}_n\times\boldsymbol{h}_m)ds=0, \tag{4.18}$$

$$\iint_s \boldsymbol{z}\cdot(\boldsymbol{e}_m\times\boldsymbol{h}_n)ds=0, \tag{4.19}$$

which is the general form of the orthogonality. In case of loss free medium inside the waveguide, the orthogonality relation is expressed as

$$\iint_s \boldsymbol{z}\cdot(\boldsymbol{e}_n\times\boldsymbol{h}^*_m)ds=0. \tag{4.20}$$

Equation (4.20) indicates that the power transferred through the cross section of a waveguide is the sum of carried power by every individual mode.

4.1. Bloch theory in periodic waveguides

We further assume the waveguide has periodic inhomogeneity in the longitudinal direction. The periodic material satisfies $M(p+x) = M(x)$ where p is the length of a period. Therefore, any function $\psi(x)$ has a periodic behavior in the form of [Sjöberg et al., 2005]

$$\psi(x+p) = \psi(x)\mathrm{e}^{-\gamma p}. \tag{4.21}$$

where γ is the complex wavenumber of the guiding medium.

In a cylindrical waveguide loaded by periodic inhomogeneity, the electric and magnetic field components for a period are written as

$$\boldsymbol{E}(x,y,z_0+p) = \boldsymbol{E}(x,y,z_0)\mathrm{e}^{-\gamma p}, \tag{4.22}$$
$$\boldsymbol{H}(x,y,z_0+p) = \boldsymbol{H}(x,y,z_0)\mathrm{e}^{-\gamma p}. \tag{4.23}$$

To compute the field components at $z = z_0$ and $z = z_0 + p$ cross sections of the wavegudie, using commercial simulators like as CST MWS [CST, 2014], the 2D eigenproblem over the cross section is solved. This eigenproblem solution will compute a set of complete basis functions over the $z = z_0$ and $z = z_0 + p$ cross sections which are called port modes. Consequently, the field distribution over the ports of a two port waveguide can be written as a combination of port modes

$$\boldsymbol{E}_{p1}(x,y,z_0) = \sum_{n=1}^{M} a_n \boldsymbol{e}_{n,p1}(x,y,z_0) + b_n \boldsymbol{e}_{n,p1}(x,y,z_0), \tag{4.24}$$
$$\boldsymbol{H}_{p1}(x,y,z_0) = \sum_{n=1}^{M} a_n \boldsymbol{h}_{n,p1}(x,y,z_0) - b_n \boldsymbol{h}_{n,p1}(x,y,z_0), \tag{4.25}$$

where a_n and b_n are the inward and outward traveling modes coefficients. The modal decomposition for the second port by considering the Bloch theorem is

$$\boldsymbol{E}_{p2}(x,y,z_0+p) = \sum_{n=1}^{M} a_n \boldsymbol{e}_{n,p1}(x,y,z_0)\mathrm{e}^{-\gamma_n p} + b_n \boldsymbol{e}_{n,p1}(x,y,z_0)\mathrm{e}^{-\gamma_n p}, \tag{4.26}$$
$$\boldsymbol{H}_{p2}(x,y,z_0+p) = \sum_{n=1}^{M} a_n \boldsymbol{h}_{n,p1}(x,y,z_0)\mathrm{e}^{-\gamma_n p} - b_n \boldsymbol{h}_{n,p1}(x,y,z_0)\mathrm{e}^{-\gamma_n p}, \tag{4.27}$$

where $a_n e^{-\gamma_n p} = a'_n$ and $b_n e^{-\gamma_n p} = b'_n$ are the coefficients of the eigenfunctions at the second port. To compute the dispersion diagram of different modes one needs to calculate equation (4.26) and (4.27) for every frequency. The desired eigenvalues for every modes are γ_n.

4.2. Eigenvalue computation for closed waveguides

To obtain the eigenvalues γ_n corresponding to every eigenfunction another relation between the eigenfunction at two ports has to be considered. For a multimode guiding medium, the amplitude of modes of different ports can be related through the generalized scattering matrix as

$$\begin{bmatrix} b_1 \\ \vdots \\ b_N \\ b'_1 \\ \vdots \\ b'_N \end{bmatrix} = \begin{bmatrix} \begin{bmatrix} S_{11} \\ S_{21} \end{bmatrix} \begin{bmatrix} S_{12} \\ S_{22} \end{bmatrix} \end{bmatrix} \begin{bmatrix} a_1 \\ \vdots \\ a_N \\ a'_1 \\ \vdots \\ a'_N \end{bmatrix}, \tag{4.28}$$

where $[S_{ij}] = \left[S_{ij}^{mn}\right]$ is the ijth scattered parameter from mode n to mode m. The nontrivial solution to matrix equations $Ax = \lambda x$ is obtained from the eigenvector decomposition of matrix $A - \lambda I$. The procedure known as singular value decomposition (SVD), produces three different matrices as

$$A = U\Sigma V^T, \tag{4.29}$$

where the U and V are orthogonal and their rows are eigenvectors and Σ is a diagonal matrix where its elements are eigenvalues. To transform the generalized scattering matrix of a multimode waveguide into a form to compute the eigenvalues of the modes, the transfer matrix of the waveguide can be employed. The transfer matrix of a waveguide is written as

$$\begin{bmatrix} b_1 \\ \vdots \\ b_N \\ a_1 \\ \vdots \\ a_N \end{bmatrix} = \begin{bmatrix} \begin{bmatrix} T_{11} \\ T_{21} \end{bmatrix} \begin{bmatrix} T_{12} \\ T_{22} \end{bmatrix} \end{bmatrix} \begin{bmatrix} a'_1 \\ \vdots \\ a'_N \\ b'_1 \\ \vdots \\ b'_N \end{bmatrix}. \tag{4.30}$$

If the number of port modes at two ports are the same, the T matrix will be a square matrix. When the T matrix is non-singular, the matrix diagonalization will result in $T = VDV^T$ with

$$D = \begin{bmatrix} \mathrm{e}^{-\gamma_1 p} & \cdots & 0 & 0 & \cdots & 0 \\ \vdots & \ddots & \vdots & \vdots & \ddots & \vdots \\ 0 & \cdots & \mathrm{e}^{-\gamma_N p} & 0 & \cdots & 0 \\ 0 & \cdots & 0 & \mathrm{e}^{\gamma_1 p} & \cdots & 0 \\ \vdots & \ddots & \vdots & \vdots & \ddots & \vdots \\ 0 & \cdots & 0 & 0 & \cdots & \mathrm{e}^{\gamma_N p} \end{bmatrix}. \tag{4.31}$$

The terms $\mathrm{e}^{-\gamma_i p}$ correspond to forward waves while the terms $\mathrm{e}^{\gamma_i p}$ correspond to backward waves. In general, $\gamma = \alpha + j\beta$ is complex value where the real part α indicates the loss along the waveguide and β indicates the phase shift. In a closed loss less structure, when the modes are not coupled, $|\mathrm{e}^{-\gamma p}| = 1$ which is equivalent to $\alpha = 0$ in the pass bands.

4.3. Complex modes in closed waveguides

As it was mentioned in the previous section, the orthogonality of modes is applicable for real and complex wavenumbers. The presence of complex modes in closed waveguides is known for a long time in waveguides loaded by dielectrics [Clarricoats and Taylor, 1964]. Especially, these modes are the result of the coupling of two forward and backward waves in a dissipation less waveguide [Clarricoats and Slinn, 1965]. These complex modes are always in conjugate pair and therefore when a set of parameters $(\gamma_n, \boldsymbol{E}_t, E_z, \boldsymbol{H}_t, H_z)$ is satisfying the source free Maxwell's equations in a closed waveguide, then $(-\gamma_n, \boldsymbol{E}_t, -E_z, -\boldsymbol{H}_t, H_z)$ and $(\pm\gamma_n^*, \boldsymbol{E}_t^*, \pm E_z^*, \pm\boldsymbol{H}_t^*, \pm H_z^*)$ are also meeting this equation [Rozzi et al., 1998, Islam and Eleftheriades, 2010, Omar and Schonemann, 1986]. For the existence of the complex modes in closed waveguides some rules have be summarized in [Rozzi et al., 1998] using the Lorenz's reciprocity theorem. Considering the electric and magnetic field in the transverse cross section of a closed homogeneous wavegudie as

$$\boldsymbol{E}(x, y, z) = \boldsymbol{e}_1(x, y)\mathrm{e}^{-\gamma_1 z} + \boldsymbol{e}_2(x, y)\mathrm{e}^{-\gamma_2 z}, \tag{4.32}$$

$$\boldsymbol{H}(x, y, z) = \boldsymbol{h}_1(x, y)\mathrm{e}^{-\gamma_1 z} + \boldsymbol{h}_2(x, y)\mathrm{e}^{-\gamma_2 z}, \tag{4.33}$$

where $\gamma_1 = \gamma_2^* = \alpha + \mathrm{j}\beta$ and the pairs $(\boldsymbol{e_1}, \boldsymbol{h_1})$ and $(\boldsymbol{e_2}, \boldsymbol{h_2})$ are complex conjugate. Consider the Lorentz's theorem for a source free region over the

cross section of the waveguide

$$\begin{aligned}\frac{\partial}{\partial z}\iint_s (\boldsymbol{E}_t \times \boldsymbol{H}'_t - \boldsymbol{E}'_t \times \boldsymbol{H}_t)\cdot \boldsymbol{z} ds \\ = -j\omega \iint_s \left[(\varepsilon-\varepsilon')\boldsymbol{E}\cdot\boldsymbol{E}' - (\mu-\mu')\boldsymbol{H}\cdot\boldsymbol{H}'\right] ds.\end{aligned} \tag{4.34}$$

Substituting the three other possibilities for field and wavenumber in the conjugate pairs instead of $\boldsymbol{E}'$, $\boldsymbol{H}'$, ε' and μ', the orthogonality relations can be examined. By defining the power coupling between modes in two real and imaginary senses

$$P_{ij} = \iint_s (\boldsymbol{e}_{ti} \times \boldsymbol{h}^*_{tj})\cdot \boldsymbol{z} ds, \quad i,j = 1,2, \tag{4.35}$$

$$Q_{ij} = \iint_s (\boldsymbol{e}_{ti} \times \boldsymbol{h}_{tj})\cdot \boldsymbol{z} ds, \quad i,j = 1,2. \tag{4.36}$$

It can be shown for all choices, that $P_{ii} = 0$. This implies the Poynting vector integration over the cross section of the waveguide for every individual complex mode is vanishing, namely no net power is carried by every single mode of a complex pair. Therefore, these modes which always are present in a complex conjugate pair, cannot transfer any net real or complex power along the waveguide. Such modes behave in this aspect like modes at cutoff. Furthermore, the orthogonality relation (4.35) confirms that $P_{12} = -P^*_{21}$. This relation indicates the exchange power between 1 and 2 are complex conjugate and opposite of each other. Therefore, a pair of complex modes can only carry pure reactive power so that they behave as a whole evanescently.

In the past, it was believed that the complex pairs are excited together. However, recently there has been some investigations that show these modes can be excited completely independently [Islam and Eleftheriades, 2010].

In the following, the effect of considering higher order modes in evaluating the eigenvalues is investigated in a unit cell of left handed material. The left handed behavior is realized by the combination of an electric resonator (ELC) and a split ring resonator (SRR) as depicted in Fig. 4.2. The unit cell sizes are $p = h = 10/3$mm, $w = 2.775$mm. Substrate is Rogers RT5870 with ε_r=2.33 and thickness of 0.381 mm. The unit cell is periodic in three dimensions. To extract the material property, however, the wave propagation along y direction

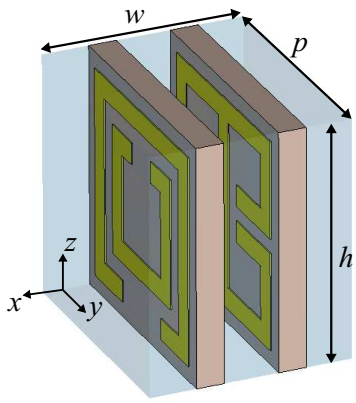

Figure 4.2.: Unit cell of a periodic structure made up of electric and magnetic resonators.

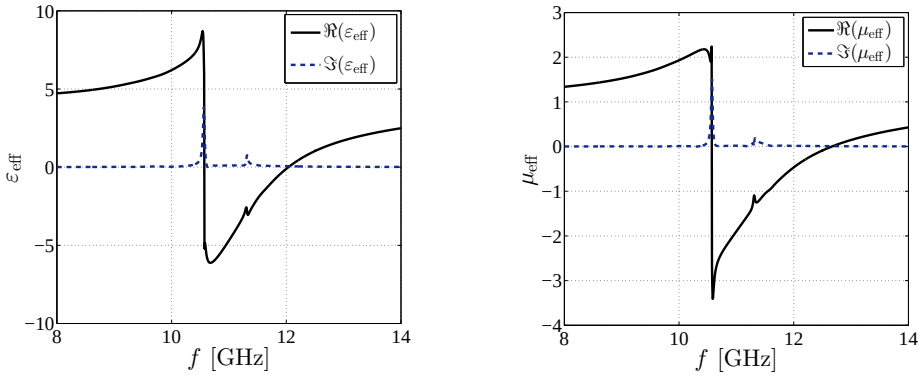

(a) Permittivity (b) Permeability

Figure 4.3.: Bulk material properties extracted for one unit cell of Fig. 4.2

is considered in the simulation. Therefore, the periodicity has been modeled by PEC/PMC boundary condition in z and x directions respectively. By this configuration, the ports are placed directly at two end faces of unit cell along y direction.

The material properties obtained using Kramers-Krönig relations explained in section 3.2, are depicted in Fig. 4.3. As it is seen, the permittivity and permeability have negative sign from 10.55 GHz to 12 GHz while from 12 to 12.7 GHz the unit cell is behaving as single negative material with negative

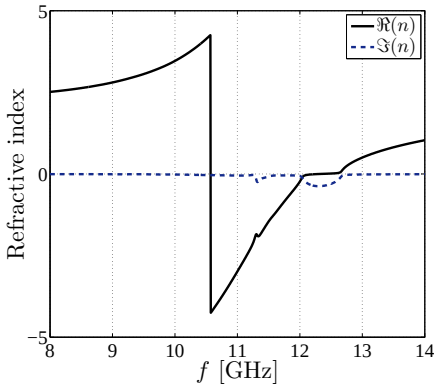

Figure 4.4.: Refractive index extracted for one unit cell of Fig. 4.2.

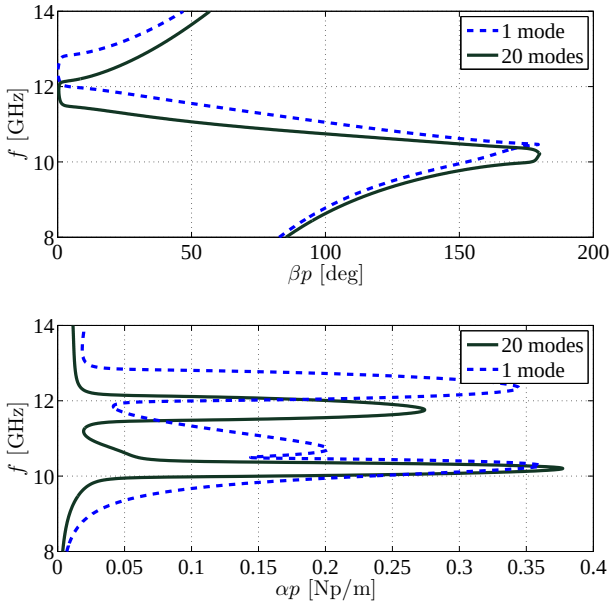

Figure 4.5.: Dispersion diagram of first Bloch mode of the unit cell Fig. 4.2 by considering 20 port modes and one port mode.

permeability. The refractive index computed from these material properties is shown in Fig. 4.4. The left handed region and the band gap behavior of the

unit cell is inferred from the refractive index.

To account for the higher order modes, twenty port modes in the excitation are considered. The computed scattering matrix is converted to transfer matrix. After that, the eigenvalues of the transfer matrix are computed with respect to the Bloch-Floquet theorem. This procedure has been repeated for one mode excitation. The dispersion diagram of the fundamental mode is compared for one mode excitation and twenty modes in excitation in Fig. 4.5. As it is depicted in the attenuation diagram of Fig. 4.5, the attenuation in the guided region is becoming lower by considering higher order modes. Since this structure has no right handed propagating mode at the same left handed band to be coupled to left handed mode and make a complex band region, it is expected that all the eigenvalues in this structure become real or imaginary. This is confirmed by increasing the number of excited modes, where, the attenuation constant is decreased in the guided wave region.

4.4. Scattering matrix approach for open waveguides

Open structures are waveguides with an unbounded boundary. Therefore, in the cross section of these wavegudies, the 2D Sturm Liouville equation of the third type (SLP3) should be solved [Dudley, 1994]. However, in most geometrical configurations it is not possible to compute the eigenmodes of the SLP3 problems. Consequently, the scattering matrix approach based on a complete basis mode decomposition is not applicable to all open waveguide structures. To extend the method of modal decomposition to open waveguides like microstrip structures and slotted waveguides, one method is to enclose the open boundary of the waveguide by PEC walls at a distant large enough to not disturb the guided modes inside the wavguide [Mittra et al., 1980, Solbach and Wolff, 1978]. However, this assumption only works for non-radiating structures. The difficulty of applying this method for radiating structures, is the reflection from PEC wall. To minimize the reflections from PEC walls, it is possible to enclose the wavegudie with an artificial absorbing boundary condition (ABC) [Derudder et al., 2001b]. For the mode matching technique the superior absorbing boundary condition is perfectly matched layer (PML). These PMLs are designed such that the enclosed waveguide can still behave like an open waveguide and the field distribution of the modes inside the wavegudie are not affected by PML layer.

The perfectly matched layers are uniaxial anisotropic material which are included in the field equations in the form of

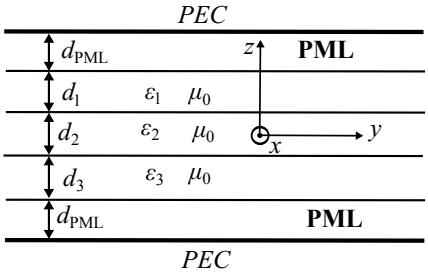

Figure 4.6.: Layered slab covered by a symmetric PML at top and bottom.

$$\boldsymbol{D} = \varepsilon\bar{\bar{\alpha}} \cdot \boldsymbol{E}, \tag{4.37}$$

$$\boldsymbol{B} = \mu\bar{\bar{\alpha}} \cdot \boldsymbol{H}, \tag{4.38}$$

such that in a stratified structure layered in the z direction it is written as

$$\bar{\bar{\alpha}} = \begin{bmatrix} \alpha(z) & 0 & 0 \\ 0 & \alpha(z) & 0 \\ 0 & 0 & \frac{1}{\alpha(z)} \end{bmatrix} \tag{4.39}$$

where $\alpha(z) = 1 + (\kappa_0 - 1)f(z) - j\frac{\sigma_0}{\omega\varepsilon_0}f(z)$. α, κ_0, σ_0 and f are the constructing parameters which indicate the type of PML.

Introducing this PML to Maxwell's equation results in two separate sets of TE and TM mode equations in the direction of wave propagation within the PMLs.

$$\frac{1}{\alpha}\frac{\partial}{\partial z}\left(\frac{1}{\alpha}\frac{\partial E_x}{\partial z}\right) + \gamma^2 E_x = 0, \tag{4.40}$$

$$\frac{1}{\alpha}\frac{\partial}{\partial z}\left(\frac{1}{\alpha}\frac{\partial H_x}{\partial z}\right) + \gamma^2 H_x = 0, \tag{4.41}$$

with $\gamma^2 = \omega^2\mu\varepsilon - k_y^2$. Due to symmetry, the equation for x components is also the same as that for y components.

By implementing the PML at the open boundary the Helmholtz equation is transformed into the complex coordinates such that the thickness of the PML layer can be considered as a complex value

$$\tilde{d}_{PML} = \int_0^{d_{PML}} \alpha z' dz'. \tag{4.42}$$

In case of an air slab terminated by PML layers at top and bottom, the dispersion equations results in discrete TE and TM modes with complex wavenumbers which are known as PML or Berenger modes. These modes have their highest field values inside the PML layer. When covering a slab of dielectric material with PMLs, two other groups of modes rather than Berenger modes are achieved. A group with real eigenvalues, which are discrete surface modes confined within the dielectric known as propagating modes and a group of complex modes with their fields more concentrated inside the dielectric layer. These modes are called leaky modes.

By this method, the complete basis for describing the field at the cross section of a waveguide with open boundary can be determined. In [Olyslager, 2004], it has been mathematically shown that the Green's function of slab waveguide terminated by PML layers can be discretized into a series of discrete modes. Assume the Green's function equation for free space as

$$\nabla_{xy}^2 g(x,y) + g(x,y) = \delta(x)\delta(y). \tag{4.43}$$

Subjected to the radiation boundary condition

$$\lim_{\rho\to+\infty}\left[\frac{\partial}{\partial\rho}g(x,y) + jg(x,y)\right] = 0, \tag{4.44}$$

with $\rho = \sqrt{x^2+y^2}$. The radiation condition which is known also as the Sommerfeld radiation condition considers the time harmonic behavior of the function as $\mathrm{e}^{\mathrm{j}\omega t}$. Using the Fourier transform for x variable

$$G(\lambda,y) = \int_{-\infty}^{+\infty} g(x,y)\mathrm{e}^{\mathrm{j}\lambda x}dx, \tag{4.45}$$

the Green's function equation becomes

$$\frac{d^2}{dy^2}G(\lambda,y) + (1-\lambda^2)G(\lambda,y) = \delta(y). \tag{4.46}$$

This one dimensional Green's function can be easily solved to

$$G(\lambda,y) = \frac{\mathrm{j}\mathrm{e}^{-\mathrm{j}\sqrt{1-\lambda^2}|y|}}{2\sqrt{1-\lambda^2}}. \tag{4.47}$$

From (4.47), it is seen that over the λ complex plane the Green's function has two branch cuts originating from $\lambda = \pm 1$. Transformation of the Green's function from spectral to spatial domain is performed by inverse Fourier transform

as

$$\int_{-\infty}^{+\infty} \frac{\mathrm{j}\mathrm{e}^{-\mathrm{j}\sqrt{1-\lambda^2}|y|}}{2\sqrt{1-\lambda^2}} \mathrm{e}^{-\mathrm{j}\lambda x} d\lambda = \frac{\mathrm{j}}{4} H_0^2(\rho). \tag{4.48}$$

The integration path over the real λ axis and the branch cunts of (4.48) are depicted in Fig. 4.7. From the Cauchy theorem, the integration over the real λ axis can be replaced by the integration around the branch cut, since the integration over the semi circle at infinity does not contribute to the final response.

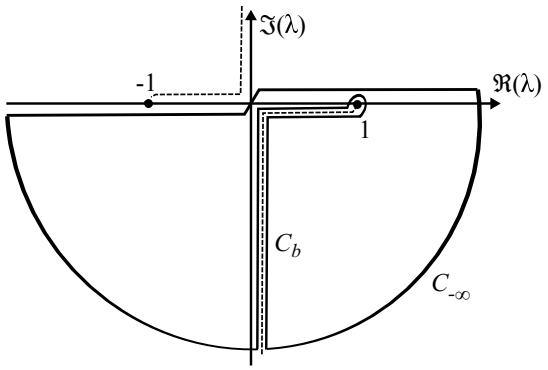

Figure 4.7.: Complex λ plane for the spectral Green's function (4.47).

To extend the closed form Green's function (4.47) to an air region terminated at the distance $\pm d$, the boundary condition for the tangential field at the termination is considered to be vanishing

$$\tilde{g}(x, y = \pm d) = 0, \tag{4.49}$$

where $d \in \mathbb{R}$. Transforming the Green's function into the spectral domain and computing the closed from Green's function results in

$$\tilde{G}(\lambda, y) = \frac{\sin\left[\sqrt{1-\lambda^2}(|y| - d)\right]}{2\sqrt{1-\lambda^2}\cos\left[\sqrt{1-\lambda^2}d\right]}. \tag{4.50}$$

Inverse Fourier transform of (4.50) gives the Green's function as

$$\tilde{g}(x,y) = \int_{-\infty}^{+\infty} \frac{\sin\left[\sqrt{1-\lambda^2}(|y|-d)\right]}{2\sqrt{1-\lambda^2}\cos\left[\sqrt{1-\lambda^2}d\right]} \mathrm{e}^{-\mathrm{j}\lambda x} d\lambda. \tag{4.51}$$

As it is seen from (4.50), the Green's function has no branch cut and has simple poles at

$$\lambda_n^{\pm} = \pm\sqrt{1-\frac{(2n+1)^2\pi^2}{4d^2}}, \quad n = 0,1,2,..., \tag{4.52}$$

which are shown on the complex λ plane in Fig. 4.8

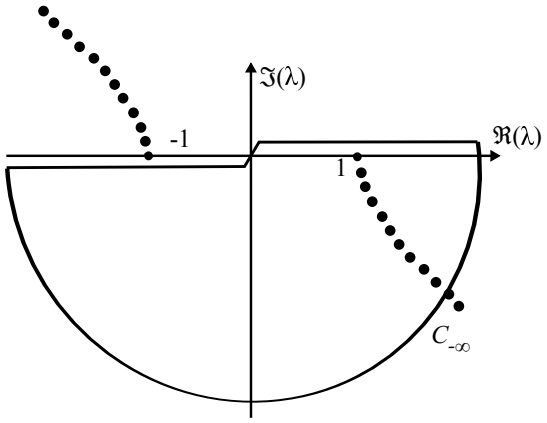

Figure 4.8.: Discrete poles of the approximated Green's function (4.50).

Using the Cauchy theorem, the Green's function (4.51) can be written as the summation of eigenmodes

$$\tilde{g}(x,y) = -\frac{j}{2d}\sum_{n=0}^{+\infty} \cos\frac{(2n+1)\pi y}{2d} \frac{\mathrm{e}^{-j\sqrt{1-\frac{(2n+1)^2\pi^2}{4d^2}}x}}{\sqrt{1-\frac{(2n+1)^2\pi^2}{4d^2}}}. \tag{4.53}$$

In this method, the branch cut which is indicating the continuum part of the spectral Green's function, has been replaced by a discrete set of poles over the complex λ plane. The poles of the Green's function which are dependent on d are PML modes.

Another general structure which can include leaky modes can be represented by replacing the free space with an interface of two semi infinite medium truncated by PMLs at top and bottom. One medium is free space, $y > y'$, with $k = 1$ and the other medium, $y < y'$, with $k = k_y$, Fig. 4.9.

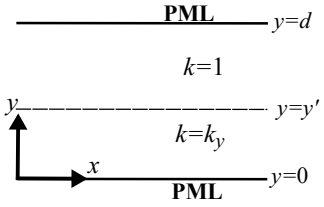

Figure 4.9.: Discrete poles of the approximated Green's function (4.50).

The Green's function equation is in the form of

$$\nabla_{xy}^2 g(x,y) + k^2(y) g(x,y) = \delta(x)\delta(y-y'), \quad y' > 0. \tag{4.54}$$

Then, the spectral domain Green's function is achieved as

$$\frac{d^2}{dy^2} G(\lambda, y) + (k^2(y) - \lambda^2) G(\lambda, y) = \delta(y - y'). \tag{4.55}$$

The Green's function can be written as

$$\tilde{G}(\lambda, y) = -\frac{\sin[\kappa_2(\lambda)(d-y')]\sin[\kappa_1(\lambda)y]}{N(\lambda)}, \quad 0 < y < y', \tag{4.56}$$

$$\tilde{G}(\lambda, y) = -\frac{\sin[\kappa_1(\lambda)y']\sin[\kappa_1(\lambda)(d-y)]}{N(\lambda)}, \quad y' < y, \tag{4.57}$$

where $\kappa_1(\lambda) = \sqrt{k_y^2 - \lambda^2}$ and $\kappa_2(\lambda) = \sqrt{1 - \lambda^2}$.

The denominator of the Green's function is

$$N(\lambda) = \kappa_2(\lambda)\sin[\kappa_1(\lambda)y']\cos[\kappa_2(\lambda)d] + \kappa_1(\lambda)\cos[\kappa_1(\lambda)y']\sin[\kappa_2(\lambda)d] \tag{4.58}$$

The Green's function in this case will have four branch cuts emanating from ± 1 and $\pm k_y$. The branch cuts at ± 1 will again result in the same PML modes which are dependent on d while the branch cuts at $\pm k_y$ when discretized, result in modes depending on y' and are called quasi leaky modes [Rogier and De Zutter, 2001].

PML layers are generally anisotropic which makes it difficult to handle the numerical modeling of these artificial boundary conditions. Therefore, realizing

the absorbing boundary conditions by isotropic material will be an advantageous. In this regard, lossy materials can be implemented to minimize the reflection of an incident wave at all frequencies and all incident angles [Weitsch and Eibert, 2011]. These PML layers are designed by adding a gradually increasing loss to higher layers, Fig. 4.10.

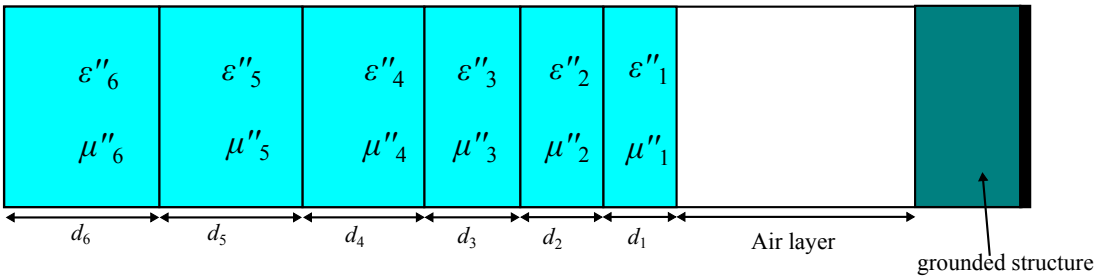

Figure 4.10.: Layered PML with increasing loss by going away from the structure.

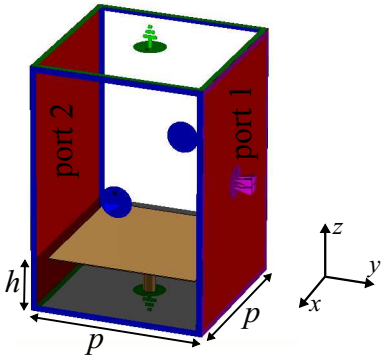

Figure 4.11.: A unit cell of the Sievenpiper mushroom with corresponding boundary condition, blue: PMC, green: PEC, open boundary at ports. Unit cell size: $p = 3.5$ mm, $h_{sub} = 1.75$ mm, patch size = 3 mm, $r_{via} = 0.125$ mm, $\varepsilon_r = 2.2$.

The unit cell of a mushroom structure introduced by Sievenpiper [Sievenpiper et al., 1999] is analyzed using SMA approach. To enclose the unit cell, the top face of the unit cell is covered by PEC boundary condition. The unit cell has been excited using waveports with two fundamental modes. The dispersion diagram computed using Bloch-Floquet theorem is depicted in Fig. 4.12. As it is observed, the first mode, on the left, shows a complex band from 12

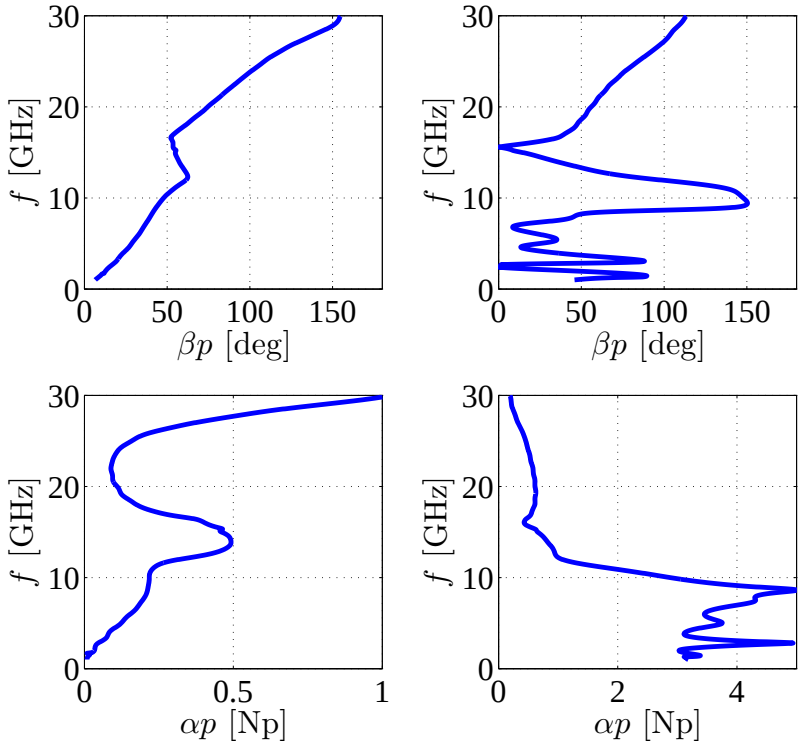

Figure 4.12.: Dispersion diagram for two fundamental modes of the SMA approach for unit cell of Fig. 4.11, left: first mode, right: second mode

GHz to 16 GHz. As it was mentioned in section 4.3, the complex modes in closed structures are due to the coupling between a right handed mode of the background waveguide and the left handed mode of the structure. The left handed mode of the structure can be observed in the dispersion diagram of the second mode, on the right, from 12 to 16 GHz.

To compensate the effect of the right handed mode of the background waveguide which is coupled to the left handed mode, the structure is covered by a multilayer homogeneous lossy absorber like as Fig. 4.10 with $d_1 = 2$ mm, $d_2 = 2$ mm, $d_3 = 2.5$ mm, $d_4 = 2.5$ mm, $d_1 = 3$ mm, $d_1 = 5$ mm. The electric and magnetic losses for every layer are equal and are indicated as $\tan\delta_1 = 0.02$, $\tan\delta_2 = 0.08$, $\tan\delta_3 = 0.2$, $\tan\delta_4 = 0.4$, $\tan\delta_5 = 0.65$, $\tan\delta_6 = 0.8$. The dispersion diagram of the fundamental mode confirms the compensation of the

coupling between the right handed and left handed modes using PML layers, Fig. 4.13.

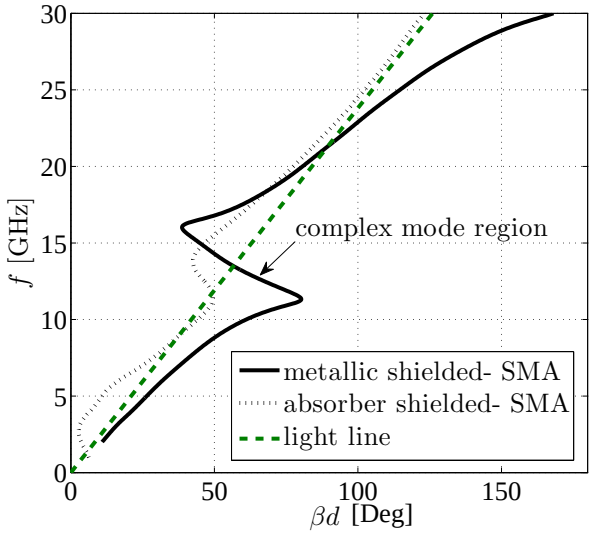

Figure 4.13.: Dispersion diagram for the fundamental mode of the SMA approach for unit cell of Fig. 4.11 with and without absorber shields.

Consideration of PML layers to account for the guided radiating modes in open structures is only useful for the guided wave applications. However, by increasing the technology very rapidly, there is an increasing demand to develop quick and accurate methods to describe the wave propagation in new media. In this purpose, in the next chapters, the computation of eigenmodes by excitation is introduced.

5. Finite element boundary integral method

Metamaterial structures analyzed in this thesis are periodic arrangement of subwavelength unit cells with possibly open boundaries at top or bottom of the unit cell. The external excitation in this work is plane wave excitation and the eigenvalues are sought in the scattered field from the unit cell. To take the advantage of finite element method for modeling arbitrary unit cell configurations together with boundary integral method for modeling global open boundaries, the hybrid finite element boundary integral method is one of the most widely used methods. This method, therefore, is used to efficiently solve the Maxwell's equations together with corresponding open boundary conditions. In this chapter, the finite element boundary integral for periodic structures is reviewed.

5.1. Maxwell's equations

For a medium of linear, inhomogeneous and anisotropic material, a system of four coupled equations can describe the behavior of a time harmonic electromagnetic field with the time dependency of the form $e^{j\omega t}$. These four equations make a set of equations known as Maxwell's equations

$$\nabla \times \boldsymbol{E}(\boldsymbol{r}) = -j\omega \boldsymbol{B}(\boldsymbol{r}) - \boldsymbol{M}(\boldsymbol{r}), \tag{5.1}$$

$$\nabla \times \boldsymbol{H}(\boldsymbol{r}) = j\omega \boldsymbol{D}(\boldsymbol{r}) + \boldsymbol{J}(\boldsymbol{r}), \tag{5.2}$$

$$\nabla \cdot \boldsymbol{D}(\boldsymbol{r}) = -\rho_e(\boldsymbol{r}), \tag{5.3}$$

$$\nabla \cdot \boldsymbol{B}(\boldsymbol{r}) = \rho_m(\boldsymbol{r}), \tag{5.4}$$

where $\boldsymbol{E}$, $\boldsymbol{H}$ are electric and magnetic field intensity, $\boldsymbol{B}$, $\boldsymbol{D}$ are the electric and magnetic flux density, $\boldsymbol{J}$, $\boldsymbol{M}$ are the electric and magnetic currents density and ρ_e , ρ_m are the electric and magnetic charge density, respectively. Equations (5.1)-(5.2) are the differential form of Faraday's and Ampere's law, equation (5.3) is the Gauss's law for electric charge while (5.4) is the Gauss's

law for magnetic field. By taking the divergence of Faraday's and Ampere's laws and using the Gauss's laws, another set of equations are achieved which indicate the conservation of the charge

$$\nabla \cdot \boldsymbol{J}(\boldsymbol{r}) = -\mathrm{j}\omega\rho_e(\boldsymbol{r}), \tag{5.5}$$
$$\nabla \cdot \boldsymbol{M}(\boldsymbol{r}) = -\mathrm{j}\omega\rho_m(\boldsymbol{r}). \tag{5.6}$$

These equations are known as continuity equations for electric and magnetic charges respectively.

The effect of constitutive medium in the general anisotropic form is considered as

$$\boldsymbol{B}(\boldsymbol{r}) = \mu_0\overline{\overline{\boldsymbol{\mu}}}_r(\boldsymbol{r}) \cdot \boldsymbol{H}(\boldsymbol{r}), \tag{5.7}$$
$$\boldsymbol{D}(\boldsymbol{r}) = \varepsilon_0\overline{\overline{\boldsymbol{\varepsilon}}}_r(\boldsymbol{r}) \cdot \boldsymbol{E}(\boldsymbol{r}). \tag{5.8}$$

Substituting (5.7) and (5.8) into the (5.2)-(5.4), the Maxwell's equations are reduced to

$$\nabla \times \boldsymbol{E}(\boldsymbol{r}) = -\mathrm{j}\omega\mu_0\overline{\overline{\boldsymbol{\mu}}}_r \cdot \boldsymbol{H}(\boldsymbol{r}) - \boldsymbol{M}(\boldsymbol{r}), \tag{5.9}$$
$$\nabla \times \boldsymbol{H}(\boldsymbol{r}) = \mathrm{j}\omega\varepsilon_0\overline{\overline{\boldsymbol{\varepsilon}}}_r \cdot \boldsymbol{E}(\boldsymbol{r}) + \boldsymbol{J}(\boldsymbol{r}), \tag{5.10}$$
$$\nabla \cdot \overline{\overline{\boldsymbol{\varepsilon}}}_r \cdot \boldsymbol{E}(\boldsymbol{r}) = -\rho_e(\boldsymbol{r}), \tag{5.11}$$
$$\nabla \cdot \overline{\overline{\boldsymbol{\mu}}}_r \cdot \boldsymbol{H}(\boldsymbol{r}) = \rho_m(\boldsymbol{r}). \tag{5.12}$$

Equations (5.9) , (5.10) are the rotation of electric and magnetic fields which also show the coupling of these two field intensities. By eliminating $\boldsymbol{E}$ or $\boldsymbol{H}$ from these equations, a second order differential equation is obtained which is known as ***vector wave equation*** either based on electric or magnetic field intensity

$$\nabla \times \overline{\overline{\boldsymbol{\mu}}}_r^{-1} \cdot \nabla \times \boldsymbol{E}(\boldsymbol{r}) - k_0^2\overline{\overline{\boldsymbol{\varepsilon}}}_r \times \boldsymbol{E}(\boldsymbol{r}) = -\mathrm{j}k_0 Z_0 \boldsymbol{J}(\boldsymbol{r}) - \nabla \times \overline{\overline{\boldsymbol{\mu}}}_r^{-1} \cdot \boldsymbol{M}(\boldsymbol{r}), \tag{5.13}$$
$$\nabla \times \overline{\overline{\boldsymbol{\varepsilon}}}_r^{-1} \cdot \nabla \times \boldsymbol{H}(\boldsymbol{r}) - k_0^2\overline{\overline{\boldsymbol{\mu}}}_r \times \boldsymbol{H}(\boldsymbol{r}) = -\mathrm{j}k_0 Y_0 \boldsymbol{M}(\boldsymbol{r}) - \nabla \times \overline{\overline{\boldsymbol{\varepsilon}}}_r^{-1} \cdot \boldsymbol{J}(\boldsymbol{r}). \tag{5.14}$$

where $Y_0 = 1/Z_0 = \sqrt{\varepsilon_0/\mu_0}$ is the wave admittance of free space and $k_0 = \omega\sqrt{\mu_0\varepsilon_0}$ is the free space wavenumber.

The wave equation is a partial differential equation which can be satisfied by an infinite number of solutions. To obtain a unique solution, appropriate

boundary conditions should be enforced. The radiation condition which guarantees the physical behavior of the field at infinity, is Sommerfeld condition [Sommerfeld, 1949]

$$\lim_{r\to\infty} r\left[\nabla\times\begin{pmatrix}\boldsymbol{E}\\ \boldsymbol{H}\end{pmatrix}+jk_0\hat{r}\times\begin{pmatrix}\boldsymbol{E}\\ \boldsymbol{H}\end{pmatrix}\right]=0, \tag{5.15}$$

with $r=|\boldsymbol{r}|$ the magnitude of position vector $\boldsymbol{r}$ and its unit direction of $\hat{r}=\frac{\boldsymbol{r}}{r}$. The wave equation subjected to the boundary conditions is only possible to be solved analytically in very specific geometries of the scatterers and radiating structures. Accurate and complete solution of wave equation in complex media needs to employ numerical computations. Because of this, a variety of numerical techniques both in time domain and frequency domain have been developed to solve for the transient and steady state response of wave equation.

Most numerical methods discretize the unknown quantity in the spatial or temporal domain. The accuracy of the solution mostly depends on the discretization. However, too much refinement of the discretizations increases the solution time and sometimes the condition number of the system matrix is increased badly for discretizations finer than $\lambda/10$. Therefore, a trade-off between the number of unknowns and the condition number of the system matrix is always a limit for the quality of discretizations.

There are a variety of numerical techniques to solve the Maxwell's equations [Taflove and Hagness, 2005] ,[Peterson et al., 1998] , [Harrington and Harrington, 1996, Jin, 2014]. In electromagnetics, the Finite element method is a general purpose technique that solves for volumetric electromagnetic fields and can be used to accurately characterize microwave components and antennas in diverse configurations. For antenna or scattering problems, the air region surrounding the model must be included and terminated with an absorbing boundary condition (ABC). The integral equation (IE) approach, which solves directly for currents on object surfaces is not as general as the FEM, but is often more efficient for large open problems since it does not require the surrounding air volume. Combining these two techniques in hybrid finite element boundary integral (FEBI) method gives this opportunity to reduce the size of the FEM domain of a given open boundary problem. In the following, the finite element and boundary integral methods and their combinations are reviewed.

5.2. Integral equations and solution methods

The major disadvantage of partial differential equations is the need of extending the discretization to the far field region to enforce the radiation condition. In

contrast to FEM, the integral equation (IE) procedure, computes the equivalent currents that are induced on the surface of objects in the model. For conducting objects the electric currents are computed and for finite dielectric objects the equivalent electric and magnetic currents are computed. The solution method is often referred to as the Method of Moments (MoM). These equivalent currents are computed through the Huygens's principle over a surface enclosing the scatterer or radiator [Harrington and Harrington, 1996]. The more general form of the Huygens's principle can be cast as the equivalence theorem [Chen, 1989].

5.2.1. Huygens's principle

Using the Green's theorem, the Huygens's principle can be derived [Harrington, 1961]. Consider a closed surface S surrounding the source of radiation and any other objects such that the infinite space exterior to the closed surface is homogeneous (Fig. 5.1).

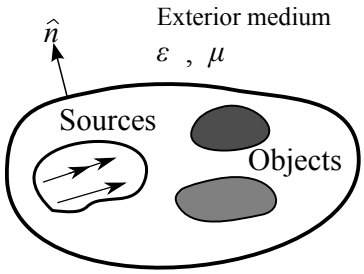

Figure 5.1.: Huygens's principle.

The total electromagnetic field at the observation point r can be obtained as

$$\boldsymbol{E}(\boldsymbol{r}) = \iint_S \big[-j\omega\mu[\hat{n}' \times \boldsymbol{H}]G_0(\boldsymbol{r},\boldsymbol{r'}) + [\hat{n}' \cdot \boldsymbol{E}]\nabla G_0(\boldsymbol{r},\boldsymbol{r'}) + [\hat{n'} \times \boldsymbol{E}(\boldsymbol{r'})] \times \nabla G_0(\boldsymbol{r},\boldsymbol{r'})\Big]\, ds', \tag{5.16}$$

$$\boldsymbol{H}(\boldsymbol{r}) = \iint_S \big[j\omega\varepsilon[\hat{n}' \times \boldsymbol{E}]G_0(\boldsymbol{r},\boldsymbol{r'}) + [\hat{n}' \cdot \boldsymbol{H}]\nabla G_0(\boldsymbol{r},\boldsymbol{r'}) + [\hat{n'} \times \boldsymbol{H}(\boldsymbol{r'})] \times \nabla G_0(\boldsymbol{r},\boldsymbol{r'})\Big]\, ds', \tag{5.17}$$

where $\hat{n}'$ indicates the unit vector normal to the S at $\boldsymbol{r}'$ and pointing outward the closed surface. By inspecting the relation between the surface currents and the tangential fields as

$$\hat{n}' \times \boldsymbol{H}(\boldsymbol{r}') = \boldsymbol{J}_s(\boldsymbol{r}'), \tag{5.18}$$
$$\boldsymbol{E}(\boldsymbol{r}') \times \hat{n}' = \boldsymbol{M}_s(\boldsymbol{r}'), \tag{5.19}$$
$$\hat{n}' \cdot \varepsilon \boldsymbol{E}(\boldsymbol{r}') = \rho_e(\boldsymbol{r}'), \tag{5.20}$$
$$\hat{n}' \cdot \mu \boldsymbol{H}(\boldsymbol{r}') = \rho_m(\boldsymbol{r}') \tag{5.21}$$

equations (5.16) and (5.17) are expressed in terms of the equivalent currents and charges as

$$\boldsymbol{E}(\boldsymbol{r}) = \iint_S \Big[- j\omega\mu \boldsymbol{J}_s(\boldsymbol{r}') G_0(\boldsymbol{r}, \boldsymbol{r}') + \frac{1}{\varepsilon} \rho_e(\boldsymbol{r}') \nabla G_0(\boldsymbol{r}, \boldsymbol{r}') + \boldsymbol{M}_s(\boldsymbol{r}') \times \nabla G_0(\boldsymbol{r}, \boldsymbol{r}') \Big] ds', \tag{5.22}$$

$$\boldsymbol{H}(\boldsymbol{r}) = \iint_S \Big[- \mathrm{j}\omega\varepsilon \boldsymbol{M}_s(\boldsymbol{r}') G_0(\boldsymbol{r}, \boldsymbol{r}') + \frac{1}{\mu} \rho_m(\boldsymbol{r}') \nabla G_0(\boldsymbol{r}, \boldsymbol{r}') + \boldsymbol{J}_s(\boldsymbol{r}') \times \nabla G_0(\boldsymbol{r}, \boldsymbol{r}') \Big] ds'. \tag{5.23}$$

$\boldsymbol{E}$ and $\boldsymbol{H}$ are the total electric and magnetic fields in the free space and $G_0 = \frac{1}{4\pi} \frac{\mathrm{e}^{-\mathrm{j}k|\boldsymbol{r}-\boldsymbol{r}'|}}{|\boldsymbol{r}-\boldsymbol{r}'|}$ is the scalar Green's function of the free space.

When there is an incident field in the free space region, a term including the incident field has to be added to the right hand side of the equations (5.16) and (5.17).

The surface integral expressions (5.22) and (5.23) are describing the exact field values in terms of surface currents and charges. However, using the continuity equations, the charges can be replaced by the corresponding current densities and the equation can be written only based on the currents. In order to obtain the equivalent currents, the observation point has to be located at the boundary surface of S. To guarantee that the IE is valid for all the points over the boundary surface, the singular points on the boundary, where the observation point is very close to the source point and the Green's function becomes infinite, are needed to be excluded from the equation. For this purpose, the

boundary surface is deformed such that the singularity point is excluded by a hemisphere [Eibert, 1997].

In computation of the total electric field inside the exterior region of the closed surface S, it is noted that the following integration is performed over the hemisphere

$$\iiint\limits_{V_b} \boldsymbol{E}(\boldsymbol{r}')\delta(\boldsymbol{r}-\boldsymbol{r}')dv' = \frac{1}{2}\boldsymbol{E}(\boldsymbol{r}). \tag{5.24}$$

By the assumption of (5.24) and considering the incident field in the problem, the surface integral field equations become

$$\begin{aligned}\frac{1}{2}\boldsymbol{E}(\boldsymbol{r}) = &\iint\limits_S -\mathrm{j}\omega\mu\boldsymbol{J}_s(\boldsymbol{r}')G_0(\boldsymbol{r},\boldsymbol{r}')ds' + \nabla\iint\limits_S \frac{1}{\mathrm{j}\omega\varepsilon}\nabla\cdot\boldsymbol{J}_s(\boldsymbol{r}')G_0(\boldsymbol{r},\boldsymbol{r}')ds' \\ &+ \iint\limits_S \boldsymbol{M}_s(\boldsymbol{r}')\times\nabla G_0(\boldsymbol{r},\boldsymbol{r}')ds' + \boldsymbol{E}^{inc}(\boldsymbol{r}),\end{aligned} \tag{5.25}$$

$$\begin{aligned}\frac{1}{2}\boldsymbol{H}(\boldsymbol{r}) = &\iint\limits_S -\mathrm{j}\omega\varepsilon\boldsymbol{M}_s(\boldsymbol{r}')G_0(\boldsymbol{r},\boldsymbol{r}')ds' + \nabla\iint\limits_S \frac{1}{\mathrm{j}\omega\varepsilon}\nabla\cdot\boldsymbol{M}_s(\boldsymbol{r}')G_0(\boldsymbol{r},\boldsymbol{r}')ds' \\ &- \iint\limits_S \boldsymbol{J}_s(\boldsymbol{r}')\times\nabla G_0(\boldsymbol{r},\boldsymbol{r}')ds' + \boldsymbol{H}^{inc}(\boldsymbol{r}),\end{aligned} \tag{5.26}$$

By multiplying the $\boldsymbol{n}\times\boldsymbol{n}\times$ by (5.25) and the $\boldsymbol{n}\times$ by (5.26)and replacing the tangential field by the tangential currents two integral equations are obtained. The resulting equations are called electric field integral equation (EFIE) and Magnetic Field Integral Equation (MFIE)respectively. In both EFIE and MFIE, the surface currents are unknown and generally numerical methods are taken to solve these equations.

$$\begin{aligned}\frac{1}{2}\boldsymbol{n}\times\boldsymbol{M}(\boldsymbol{r}) = \boldsymbol{n}\times\boldsymbol{n}\times\Bigg[&\iint\limits_S -\mathrm{j}\omega\mu\boldsymbol{J}_s(\boldsymbol{r}')G_0(\boldsymbol{r},\boldsymbol{r}')ds' + \\ &\nabla\iint\limits_S \frac{1}{j\omega\varepsilon}\nabla\cdot\boldsymbol{J}(\boldsymbol{r}')G_0(\boldsymbol{r},\boldsymbol{r}')ds' + \iint\limits_S \boldsymbol{M}_s(\boldsymbol{r}')\times\nabla G_0(\boldsymbol{r},\boldsymbol{r}')ds' + \boldsymbol{E}^{inc}(\boldsymbol{r})\Bigg],\end{aligned}$$

(5.27)

$$\frac{1}{2}\boldsymbol{J}(\boldsymbol{r}) = \boldsymbol{n} \times \Bigg[\iint\limits_{S} -\mathrm{j}\omega\varepsilon \boldsymbol{M}_s(\boldsymbol{r}')G_0(\boldsymbol{r},\boldsymbol{r}')ds' + \nabla \iint\limits_{S} \frac{1}{j\omega\mu}\nabla\cdot\boldsymbol{M}(\boldsymbol{r}')G_0(\boldsymbol{r},\boldsymbol{r}')ds' - \iint\limits_{S} \boldsymbol{J}_s(\boldsymbol{r}')\times\nabla G_0(\boldsymbol{r},\boldsymbol{r}')ds' + \boldsymbol{H}^{inc}(\boldsymbol{r}) \Bigg]. \tag{5.28}$$

The disadvantage of these integral equations is the problem of *interior resonance* such that the IEs result in nonunique or unstable responses at the vicinity of resonant frequencies of the cavity formed by the surface S covered by a PEC and filled with the homogeneous material of the exterior region. To overcome this problem, the linear combination of both EFIE and MFEI is regarded as the desired IE which is known as combined field integral equation (CFIE)

$$\alpha\mathrm{EFIE} + (1-\alpha)Z_0\boldsymbol{n}\times\mathrm{MFIE}, \tag{5.29}$$

where $\alpha \in [0,1]$ and $Z_0 = \sqrt{\frac{\mu}{\varepsilon}}$. By this formulation, the cavity resulting from EFIE and MFIE is modelled as a cavity with impedance boundary condition and therefore the interior resonant frequencies become complex subsequently a unique and stable solution will be obtained [Mautz and Harrington, 1977].

5.2.2. Solution of the integral equations by moment method

In order to solve the integral equation, especially in complex geometries, the numerical discretizations are employed to replace the integral with a summation. In these methods, the idea is to reduce the functional equation to the matrix equation and then solve it by known techniques [Harrington and Harrington, 1996]. In boundary integral formulation of the problems, the boundary surface S is discretized by two dimensional triangular meshes. The next step is to approximate field over these triangles by some basis functions. Until now, the most complete basis functions which satisfy the continuity of the currents on triangular common edges are Rao Wilton Glisson (RWG) basis functions shown in Fig. 5.2. Therefore, the currents over the BI are approximated as

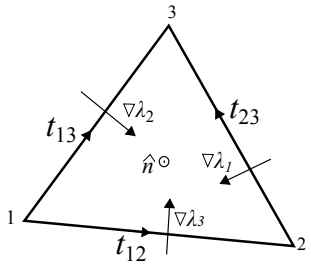

(a) The triangular element with local coordinate numbers

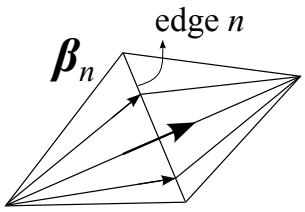

(b) The RWG vector basis function

Figure 5.2.: Vector basis function for BI discretization

$$\boldsymbol{J}_s(\boldsymbol{r}) = \sum_{n=1}^{N} U_n \boldsymbol{\beta}_n(\boldsymbol{r}), \tag{5.30}$$

$$\boldsymbol{M}_s(\boldsymbol{r}) = \sum_{n=1}^{M} V_n \boldsymbol{\beta}_n(\boldsymbol{r}). \tag{5.31}$$

The coefficients U_n and V_n are unknown and are to be computed via the solution of integral equation and vectors $\boldsymbol{\beta}_n$ are RWG basis functions. These subdomain functions were first introduced in [Rao et al., 1982] and are defined as

$$\boldsymbol{\beta}_j(\boldsymbol{r}) = \mp \frac{\boldsymbol{r} - \boldsymbol{r}_{4-j}}{2A_T} (\hat{n}_A \cdot \hat{n}(\boldsymbol{r})) \begin{cases} -, j = 1, 3 \\ +, j = 2 \end{cases} \tag{5.32}$$

where $\boldsymbol{r}_{4-j}$ is the position vector of the $(4-j)$th vertex and A_T is the surface of the triangle mesh element and $\hat{n}_A$ is the normal unit vector on the particular triangle.

The main property of these vector functions is that the continuity of the surface magnetic and electric currents over Huygens surface can be realized by them. Therefore, the electric and magnetic field intensity can be approximated as

$$\boldsymbol{E}_s(\boldsymbol{r}) = -\sum_{n=1}^{N} U_n \boldsymbol{\alpha}_n(\boldsymbol{r}), \tag{5.33}$$

$$\boldsymbol{H}_s(\boldsymbol{r}) = \sum_{n=1}^{M} V_n \boldsymbol{\alpha}_n(\boldsymbol{r}), \tag{5.34}$$

with

$$\boldsymbol{\beta}_n(\boldsymbol{r}) = \hat{n}(\boldsymbol{r}) \times \boldsymbol{\alpha}_n(\boldsymbol{r}). \tag{5.35}$$

Vector functions $\boldsymbol{\alpha}$ are called Whitney edge elements [Jin, 2014].

By using RWG basis functions as the test function in the method of moment formulation, the resulting is called Galerkin's method. Applying the Galerkin's method to IEs for every test function a system of linear equations is obtained. For test function $\boldsymbol{\beta}_m(\boldsymbol{r}_m)$ and source point at $\boldsymbol{r}_m$ the EFIE is written as

$$\begin{aligned}
&\frac{1}{2}\sum_{n=1}^{N} U_n \iint\limits_S \boldsymbol{\beta}_m(\boldsymbol{r}_m)\cdot[\boldsymbol{\beta}_n(\boldsymbol{r}_n)\times\hat{n}(\boldsymbol{r}_n)] \\
&+ j\omega\mu\sum_{n=1}^{N} V_n \left\{ \iint\limits_S \boldsymbol{\beta}_m(\boldsymbol{r}_m)\cdot\left[\iint\limits_S G_0(\boldsymbol{r}_m,\boldsymbol{r}_n)\boldsymbol{\beta}_n(\boldsymbol{r}_n)ds'\right]ds\right\} \\
&+ \frac{1}{j\omega\varepsilon}\sum_{n=1}^{N} V_n \left\{ \iint\limits_S \nabla_s\cdot\boldsymbol{\beta}_m(\boldsymbol{r}_m)\left[\iint\limits_S G_0(\boldsymbol{r}_m,\boldsymbol{r}_n)\nabla'_s\cdot\boldsymbol{\beta}_n(\boldsymbol{r}_n)ds'\right]ds\right\} \\
&+ \sum_{n=1}^{N} U_n \left\{ \iint\limits_S \boldsymbol{\beta}_m(\boldsymbol{r}_m)\cdot\left[\iint\limits_S \nabla G_0(\boldsymbol{r}_m,\boldsymbol{r}_n)\times\boldsymbol{\beta}_n(\boldsymbol{r}_n)ds'\right]ds\right\} \\
&= \iint\limits_S \boldsymbol{\beta}_m(\boldsymbol{r}_m)\cdot\boldsymbol{E}^{inc}(\boldsymbol{r}_m)ds.
\end{aligned} \tag{5.36}$$

The MFIE and CFIE also can be written in the form of matrices by Galerkin's method [Eibert, 1997]. However, choosing the test function for CFIE is not very obvious. The CFIE with RWG as the basis and testing functions leads to a very unstable solution [Sheng et al., 1998] therefore, the implementation of $RWG + \boldsymbol{n}\times RWG$ as test functions is suggested [Yla-Oijala and Taskinen, 2003]. Due to the $\frac{1}{R}$ dependence of Green's function to the distance between the source and observation point, the Green's function and therefore, the integral shows some singularities which are overcome by singularity extraction methods [Wilton et al., 1984, Graglia, 1993] or with some analytic methods [Eibert and Hansen, 1995].

5.3. Finite element method

The partial differential equation methods have the advantage of simple formulation even in the case of complex media and result in the simple numeri-

cal implementations. In addition, they produce highly sparse matrices which can be efficiently solved by special algorithms [Jin, 2014]. The finite element method, which is a partial differential equation method, is a technique for obtaining approximate solution to boundary value problems. The principle of the method is to replace a continuous domain by a number of subdomains which are usually referred to as elements. The behavior of the solution inside the element domains is modeled by interpolation functions containing the few unknown values of the elements nodes. Thus, the behavior of the whole system is approximately represented by a finite number of nodal values. Then a system of algebraic equations is obtained and the solution of the boundary value problem is achieved by solving the system of equations.

After the discretization of the solution domain and choosing the interpolation function, the element equation inside every element has to be derived which is usually performed by using variational techniques [Jin, 2014]. The resultant is a functional which is to be minimized by finding the stationary points of it. This stationary point corresponds to the solution of the aforementioned boundary value problem.

The appropriate functional corresponding to the wave equation can be obtained from the equation (5.13) as

$$F_v(\boldsymbol{E}) = \frac{1}{2}\iiint\limits_V \left[\frac{1}{\mu_r}(\nabla \times \boldsymbol{E}_{ad}) \cdot (\nabla \times \boldsymbol{E}) - k_0^2 \varepsilon_r \boldsymbol{E}_{ad} \cdot \boldsymbol{E}\right] dv + \frac{1}{2}\iint\limits_S [\boldsymbol{E}_{ad} \cdot (\hat{n} \times \nabla \times \boldsymbol{E})] da + \iiint\limits_V \boldsymbol{E}_{ad} \cdot \left[jk_0 Z_0 \boldsymbol{J}_s + \nabla \times \frac{\boldsymbol{M}_s}{\mu_r}\right] dv. \tag{5.37}$$

The partial differential equation based numerical techniques do not include any Green's function. This makes these methods inefficient especially for modeling the open boundaries. On the other hand, the integral equation methods have the advantage of simple numerical implementation with a minimum discretization region. This advantage is because of the modeling of the open boundaries by Green's function. However, they have a drawback when modeling of the complex media.

5.3.1. Solution of finite element

To solve the finite element functional (5.37), the volume of the object V has to be discretized using subdomains known as elements. The 3D elements are in the form of tetrahedra, triangular prisms or rectangular bricks. Among them,

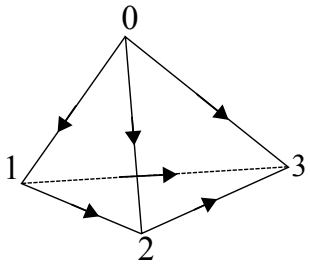

(a) The tetrahedron element with local coordinate numbers

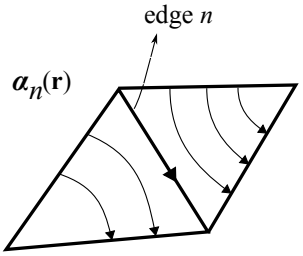

(b) Edge element basis function

Figure 5.3.: Vector basis function for FE discretization

tetrahedrons are the simplest and best suited for arbitrary volume domain [Jin, 2014]. After numbering of elements the next step is defining an interpolation function to approximate the unknown solution within an element. In general there are two strategies to select the interpolation function depending on the degrees of freedom in the element. The first developed interpolation functions are node functions where they approximate the field value linearly over the nodes of tetrahedrons. The drawbacks of these linear tetrahedrons are arising spurious modes because of the lack of enforcement of the divergence condition to the field, the difficulty of imposing the boundary conditions at material interface as well as at conducting surfaces. The suggested approach to overcome these difficulties is vector basis that assign degrees of freedom to the edges of the tetrahedron.

The desired edge elements are zeroth order edge elements $\boldsymbol{\alpha}_n(\boldsymbol{r})$ depicted in Fig. 5.3.

As it was shown in (5.35), these edge element functions are normal to the RWG basis functions where the triangles meet the BI surface. The electric and magnetic fields are expanded based on this basis inside the FE volume for element e as

$$\boldsymbol{E}^e(\boldsymbol{r}) = \sum_{i=1}^{6} E_i \boldsymbol{\alpha}_i^e(\boldsymbol{r}), \tag{5.38}$$

$$\boldsymbol{E}_{adj}^e(\boldsymbol{r}) = \sum_{i=1}^{6} E_{i,ad} \boldsymbol{\alpha}_i^e(\boldsymbol{r}), \tag{5.39}$$

$$\boldsymbol{H}_s(\boldsymbol{r}) = \sum_{i=1}^{6} H_i \boldsymbol{\alpha}_i^e(\boldsymbol{r}), \tag{5.40}$$

where, the maximum number 6 in summations indicates the tetrahedrons with 6 edges.

Substituting (5.39)-(5.40) into (5.37) and considering $\boldsymbol{M}_s = 0$, a system of matrix for element e is obtained as

$$0 = \frac{1}{2}\sum_{e=1}^{M}\{E^e\}^T[K^e]\{E^e\} + \frac{1}{2}\sum_{e=1}^{M_s}\{E^s\}^T[B^s]\{E^s\} - \sum_{e=1}^{M_{v1}}\{b^s\}, \tag{5.41}$$

where

$$[E^e] = \iiint\limits_{V^e}\left[\frac{1}{\mu_r}\{\nabla\times\boldsymbol{\alpha}^e\}\cdot\{\nabla\times\boldsymbol{\alpha}^e\} - k_0^2\varepsilon_r^e\{\boldsymbol{\alpha}^e\}\cdot\{\boldsymbol{\alpha}^e\}\right]dV, \tag{5.42}$$

$$[B^s] = \iint\limits_{S^s} jk_0Z_0\{\boldsymbol{n}\times\boldsymbol{\alpha}^e\}\cdot\{\boldsymbol{n}\times\boldsymbol{\alpha}^e\}dS, \tag{5.43}$$

$$[b^s] = \iiint\limits_{V^s} jk_0Z_0\boldsymbol{\alpha}^e\cdot\boldsymbol{J}_i dV, \tag{5.44}$$

with M the total number of volume elements, M_s the number of surface elements on the dielectric part of open boundary and M_{v1} the number of volume elements containing the source. This system of equations can be written in the matrix form and to solve it, the solution domain needs to be terminated outside the open boundary. For closed structures, usually Neumann or Dirichlet boundary conditions or a combination of them is describing the field behavior at the surface enclosing the FE discretization. For open structure, to terminate the computational finite element domain, artificial boundary conditions are utilized. These boundary conditions can be of two major types, absorbing boundary condition (ABC) and perfectly matched layers (PML). The final resulting matrix equation from FE discretization can be solved by Galerkin or Ritz methods [Jin, 2014].

5.4. Hybrid finite element boundary integral / FEBI

The idea of combining differential equations based with integral equations based methods is coming from mechanical engineering with the method of finite element - boundary element [Jin, 2014]. By introducing an artificial boundary enclosing the scatterer, the field internal to the boundary is expressed by a variational equation while the field exterior to the boundary is expanded based on the eigenmodes of the scatterer by involving the Green's function of the

free space over the boundary. The field obtained from the boundary integral part is then imposed to the variational equation as a boundary condition over the aforementioned artificial boundary. The variational equation is then solved by using the finite element method. A configuration for the FEBI object in Fig. 5.4 indicates the closed surface surrounding the whole object which is a composition of dielectric and PEC parts. In the presence of incident fields, the BI formulation is applied to the open boundary which is composed of surfaces $A_1 + A_\infty$. A_∞ is the closed surface surrounding the volume V_1 at the infinity.

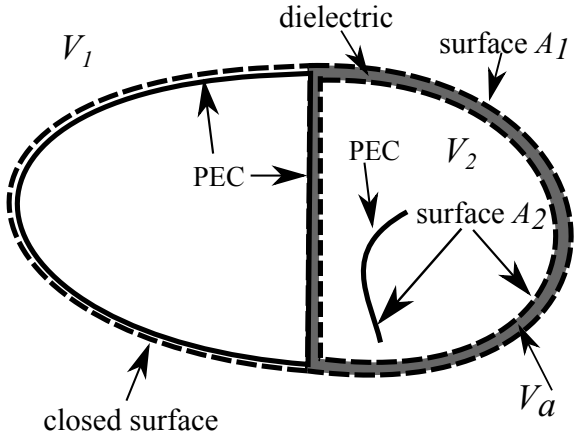

Figure 5.4.: The FEBI object.

In this configuration, the CFIE is written as

$$\frac{1}{2}\boldsymbol{n}\times\boldsymbol{M}_{A_1}(\boldsymbol{r}) = \boldsymbol{n}\times\boldsymbol{n}\times\left[\iint\limits_{A_1} -\mathrm{j}\omega\mu\boldsymbol{J}_{A_1}(\boldsymbol{r}')G(\boldsymbol{r},\boldsymbol{r}')da' + \right.$$

$$\left.\nabla\iint\limits_{A_1}\frac{1}{\mathrm{j}\omega\varepsilon}\nabla\cdot\boldsymbol{J}(\boldsymbol{r}')G(\boldsymbol{r},\boldsymbol{r}')da' + \iint\limits_{A_1}\boldsymbol{M}_{A_1}(\boldsymbol{r}')\times\nabla G(\boldsymbol{r},\boldsymbol{r}')da' + \boldsymbol{E}^{inc}(\boldsymbol{r})\right]$$

$$, \qquad \boldsymbol{r}\in A_1 \tag{5.45}$$

and

$$\frac{1}{2}\boldsymbol{J}_{A_1}(\boldsymbol{r}) = \boldsymbol{n} \times \Bigg[\iint\limits_{A_1} -\mathrm{j}\omega\varepsilon \boldsymbol{M}_{A_1}(\boldsymbol{r}')G(\boldsymbol{r},\boldsymbol{r}')da' + \nabla \iint\limits_{A_1} \frac{1}{\mathrm{j}\omega\mu}\nabla\cdot\boldsymbol{M}(\boldsymbol{r}')G(\boldsymbol{r},\boldsymbol{r}')da' - \iint\limits_{A_1} \boldsymbol{J}_{A_1}(\boldsymbol{r}')\times\nabla G(\boldsymbol{r},\boldsymbol{r}')da' + \boldsymbol{H}^{inc}(\boldsymbol{r}) \Bigg] \quad , \quad \boldsymbol{r}\in A_1. \tag{5.46}$$

Also, the homogeneous region A_2 interior to volume V_2 can be the solution domain of the BIM where there is no incident field

$$\frac{1}{2}\boldsymbol{n}\times\boldsymbol{M}_{A_2}(\boldsymbol{r}) = \boldsymbol{n}\times\boldsymbol{n}\times \Bigg[\iint\limits_{A_2} -\mathrm{j}\omega\mu \boldsymbol{J}_{A_2}(\boldsymbol{r}')G(\boldsymbol{r},\boldsymbol{r}')da' + \nabla \iint\limits_{A_2} \frac{1}{\mathrm{j}\omega\varepsilon}\nabla\cdot\boldsymbol{J}(\boldsymbol{r}')G(\boldsymbol{r},\boldsymbol{r}')da' + \iint\limits_{A_2} \boldsymbol{M}_{A_2}(\boldsymbol{r}')\times\nabla G(\boldsymbol{r},\boldsymbol{r}')da' \Bigg] \quad , \quad \boldsymbol{r}\in A_2 \tag{5.47}$$

and

$$\frac{1}{2}\boldsymbol{J}_{A_2}(\boldsymbol{r}) = \boldsymbol{n}\times \Bigg[\iint\limits_{A_2} -\mathrm{j}\omega\varepsilon \boldsymbol{M}_{A_2}(\boldsymbol{r}')G(\boldsymbol{r},\boldsymbol{r}')da' + \nabla \iint\limits_{A_2} \frac{1}{\mathrm{j}\omega\mu}\nabla\cdot\boldsymbol{M}(\boldsymbol{r}')G(\boldsymbol{r},\boldsymbol{r}')da' - \iint\limits_{A_2} \boldsymbol{J}_{A_2}(\boldsymbol{r}')\times\nabla G(\boldsymbol{r},\boldsymbol{r}')da' \Bigg] \quad , \quad \boldsymbol{r}\in A_2. \tag{5.48}$$

Therefore, the CFIE is written for all open boundaries except for the part of A_2 located in the internal PEC thin layer [Tzoulis, 2009].

The field inside the dielectric region is modeled by finite element where inhomogeneous and anisotropic materials can be supported too. In this purpose, the functional 5.37 is fomulated over the finite element region V_a surrounded

by surfaces A_1 and A_2

$$0 = \iiint_{V_a} \left[(\nabla \times \boldsymbol{E}_{ad}^{int}(\boldsymbol{r})) \cdot \overline{\overline{\boldsymbol{\mu}}}_r^{-1}(\boldsymbol{r}) \cdot (\nabla \times \boldsymbol{E}^{int}(\boldsymbol{r})) - k_0^2 \boldsymbol{E}_{ad}(\boldsymbol{r}) \cdot \overline{\overline{\boldsymbol{\varepsilon}}}_r(\boldsymbol{r}) \cdot \boldsymbol{E}^{int}(\boldsymbol{r}) \right] dv$$
$$+ jk_0 Z_0 \oiint_{A_1+A_2} \left[\boldsymbol{E}_{ad}^{int}(\boldsymbol{r}) \cdot \left[\boldsymbol{H}^{int}(\boldsymbol{r}) \times \boldsymbol{n} \right] \right] da - jk_0 Z_0 \iiint_{V_a} \boldsymbol{E}_{ad}^{int}(\boldsymbol{r}) \cdot \boldsymbol{J}(\boldsymbol{r}) dv. \tag{5.49}$$

As mentioned, the system of coupled equations resulted from hybrid finite element boundary integral is solved by the variational method in the FE part and moment method in the BI part. The coupling is performed at the dielectric boundary $A_1 + A_2$. This implies the continuity of tangential fields over the surfaces A_1 and A_2

$$\boldsymbol{n} \times \boldsymbol{E}^{int}(\boldsymbol{r}) = \boldsymbol{n} \times \boldsymbol{E}^{ext}(\boldsymbol{r}), \tag{5.50}$$
$$\boldsymbol{n} \times \boldsymbol{H}^{int}(\boldsymbol{r}) = \boldsymbol{n} \times \boldsymbol{H}^{ext}(\boldsymbol{r}). \tag{5.51}$$

5.5. Periodic boundary condition in FEBI

The metamaterial structures investigated in this thesis are doubly periodic stratified media. The constructing unit cell has a regularly shaped boundary at the side walls, see Fig. 5.5. This array is assumed to be periodic in the $xy-$plane and (m, n)th cell of the array is obtained by shifting the $(0, 0)$th cell in the direction of $\boldsymbol{\rho}_{mn} = m\boldsymbol{\rho}_a + n\boldsymbol{\rho}_b$. $\boldsymbol{\rho}_a$ and $\boldsymbol{\rho}_b$ are the lattice vectors parallel to x and y directions.

To analyze the periodic structure, the advantage of periodicity is taken where one unit cell is modeled by the numerical modeling and the field intensity is forced to satisfy the periodic boundary conditions [Eibert et al., 1999]

$$\boldsymbol{E}(\boldsymbol{r} + m\boldsymbol{\rho}_a + n\boldsymbol{\rho}_b) = \boldsymbol{E}(\boldsymbol{r}) \mathrm{e}^{-j\boldsymbol{k}_{t00} \cdot \boldsymbol{\rho}_a + n\boldsymbol{\rho}_b}, \tag{5.52}$$
$$\boldsymbol{H}(\boldsymbol{r} + m\boldsymbol{\rho}_a + n\boldsymbol{\rho}_b) = \boldsymbol{H}(\boldsymbol{r}) \mathrm{e}^{-j\boldsymbol{k}_{t00} \cdot \boldsymbol{\rho}_a + n\boldsymbol{\rho}_b}, \tag{5.53}$$

where $\boldsymbol{k}_{t00} = k_{x00}\hat{x} + k_{y00}\hat{y}$ is the incident plane wave corresponding to the incident angle of θ_0 and ϕ_0 in the spherical coordinate as

$$k_{x00} = k_0 \sin(\theta_0) \cos(\phi_0), \tag{5.54}$$
$$k_{y00} = k_0 \sin(\theta_0) \sin(\phi_0). \tag{5.55}$$

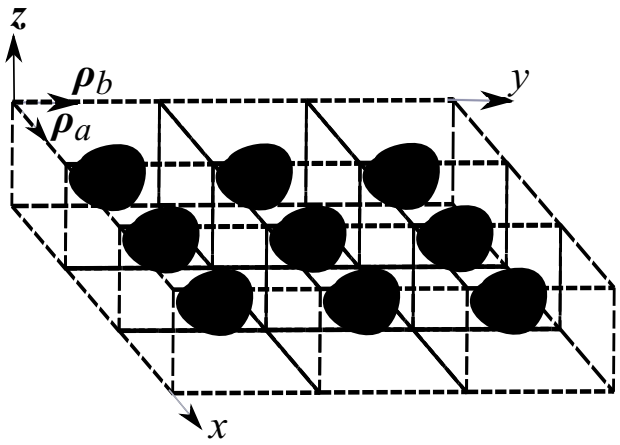

Figure 5.5.: The two dimensional configuration of periodic unit cells for FEBI modeling, O.B.C: open boundary condition, P.B.C: periodic boundary condition.

k_0 is the free space wavenumber at the operating frequency. The FE functional to describe the unit cell inhomogeneity can be obtained from the general form of FE functional (5.37). For a region free of magnetic source current the functional is written as

$$F(\boldsymbol{E}_{ad}, \boldsymbol{E}) = \iiint_V \left[\frac{1}{\mu_r}(\nabla \times \boldsymbol{E}_{ad}) \cdot (\nabla \times \boldsymbol{E}) - k_0^2 \varepsilon_r \boldsymbol{E}_{ad} \cdot \boldsymbol{E}\right] dv + jk_0 Z_0 \iint_S [\boldsymbol{E}_{ad} \cdot (\boldsymbol{H} \times \hat{n})] da + jk_0 Z_0 \iiint_V \boldsymbol{E}_{ad} \cdot \boldsymbol{J}^{int} dv. \tag{5.56}$$

where $\boldsymbol{J}^{int}$ indicates the volume excitation current interior to the FE domain and S is the surface surrounding the FE domain with $\hat{n}$ the unit vector normal to the surface of the FE directed to the outside of FE domain. To rearrange the functional in terms of only electric field intensity the integration of the magnetic tangential field over the BI should be replaced by the MFIE (5.26). By inspecting non PEC boundary and $\boldsymbol{E}(\boldsymbol{r'}) \times \hat{n} = \boldsymbol{M}_s(\boldsymbol{r'})$ the MFIE is

$$\boldsymbol{H}(\boldsymbol{r}) = \iint_S -2\mathrm{j}\omega\varepsilon(\boldsymbol{E}(\boldsymbol{r'}) \times \hat{n}) G_0(\boldsymbol{r}, \boldsymbol{r'}) ds' + \nabla \iint_S \frac{1}{\mathrm{j}\omega\varepsilon} \nabla \cdot (\boldsymbol{E}(\boldsymbol{r'}) \times \hat{n}) G_0(\boldsymbol{r}, \boldsymbol{r'}) ds' + \boldsymbol{H}^{inc}(\boldsymbol{r}), \tag{5.57}$$

substituting (5.57) into (5.58)and inspecting the divergence theorem one achieves

$$
\begin{aligned}
F(\boldsymbol{E}_{ad}, \boldsymbol{E}) = \iiint_V \Big[& \frac{1}{\mu_r}(\nabla \times \boldsymbol{E}_{ad}) \cdot (\nabla \times \boldsymbol{E}) - k_0^2 \varepsilon_r \boldsymbol{E}_{ad} \cdot \boldsymbol{E} dv \\
& + jk_0 Z_0 \boldsymbol{E}_{ad} \cdot \boldsymbol{J}^{int} \Big] dv - 2k_0^2 \iint_S \iint_S G(\boldsymbol{r}, \boldsymbol{r}_s) \Big[(\hat{n} \times \\
& \boldsymbol{E}_{ad}(\boldsymbol{r})) \cdot (\hat{n} \times \boldsymbol{E}(\boldsymbol{r}_s)) - \frac{1}{k_0^2} \nabla_s \cdot (\hat{n} \times \boldsymbol{E}_{ad}(\boldsymbol{r})) \nabla_s \cdot (\hat{n} \times \boldsymbol{E}(\boldsymbol{r}_s)) \Big] ds_s ds \\
& + jk_0 Z_0 \iint_S (\hat{n} \times \boldsymbol{E}_{ad}(\boldsymbol{r})) \cdot \boldsymbol{H}^{ext}(\boldsymbol{r}) ds.
\end{aligned}
\tag{5.58}
$$

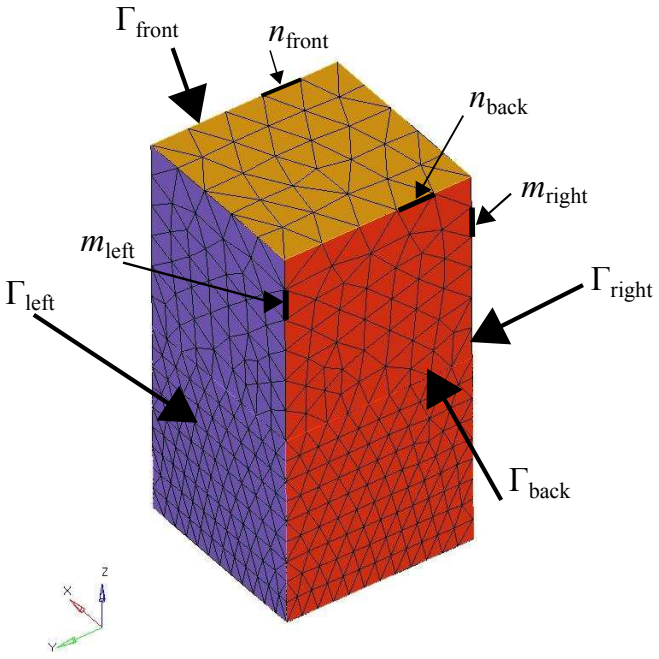

Figure 5.6.: FE mesh of 2D periodic structure.

The periodic boundary conditions at the vertical side walls in the FE domain are the phase boundary condition which yield a unique solution to the field problem. Moreover, to assure the periodicity of the field distribution in free

space, the free space Green's function must be replaced by the periodic Green's function.

The phase boundary condition to be employed in the FE domain is the same as the phase shift in the planar arrays [McGrath and Pyati, 1994]. For this the mesh configuration should be the same at opposite side walls, Fig. 5.6.

Using the edge element basis functions for FE discretization, then if e_m is the field at an edge of the vertical walls, the value e_n of the field at the corresponding edge on the opposite side wall is given as

$$e_n = e_m \mathrm{e}^{-j\boldsymbol{k}_{t00}\cdot\Delta\boldsymbol{r}} \tag{5.59}$$

with $\Delta\boldsymbol{r} = (\boldsymbol{\rho}_a \text{or} \boldsymbol{\rho}_b)$ is the vector connecting the two edges. Therefore, the unknown fields on the edges over Γ_{back} and Γ_{left} are eliminated by replacing the shifted field over edges on Γ_{front} and Γ_{right} respectively through relation (5.59).

The surface meshes of the FE part are compatible by the BI vector basis functions. Therefore the surface integrals in (5.58) are discretized over the BI using RWG basis functions. In order to implement the periodic boundary conditions for the field over the BI and surface currents on it, the Green's function in (5.58) also, must be periodic. The spectral domain Green's function for free space can be written as

$$G_P(\boldsymbol{r},\boldsymbol{r}') = \sum_{m=-\infty}^{+\infty}\sum_{n=-\infty}^{+\infty} \frac{\mathrm{e}^{-\mathrm{j}\boldsymbol{k}_{tmn}\cdot(\boldsymbol{\rho}-\boldsymbol{\rho}')}}{2\mathrm{j}Ak_{zmn}} \mathrm{e}^{-jk_{zmn}|z-z'|}. \tag{5.60}$$

with $A = |\boldsymbol{\rho}_a \times \boldsymbol{\rho}_b|$ is the cross section of the unit cell, $\boldsymbol{r} = \boldsymbol{\rho} + z\hat{z}$ and

$$\boldsymbol{k}_{tmn} = \boldsymbol{k}_{t00} + \frac{2\pi}{A}[m(\boldsymbol{\rho}_b \times \hat{z}) + n(\hat{z} \times \boldsymbol{\rho}_a)]. \tag{5.61}$$

At the end, the matrix form of the FEBI for periodic structure is

$$\begin{bmatrix} A^{int} & A^{cross}_{1,top} & A^{cross}_{1,bot} \\ A^{cross}_{2,top} & A^{bound}_{top} & 0 \\ A^{cross}_{2,bot} & 0 & A^{bound}_{bot} \end{bmatrix} \begin{Bmatrix} \mathrm{e}^{int} \\ \mathrm{e}^{bound}_{top} \\ \mathrm{e}^{bound}_{bot} \end{Bmatrix} + \begin{bmatrix} 0 & 0 & 0 \\ 0 & Z_{top} & 0 \\ 0 & 0 & Z_{bot} \end{bmatrix} \begin{Bmatrix} \mathrm{e}^{int} \\ \mathrm{e}^{bound}_{top} \\ \mathrm{e}^{bound}_{bot} \end{Bmatrix} = \begin{Bmatrix} f^{int} \\ f^{bound}_{top} \\ f^{bound}_{bot} \end{Bmatrix} \tag{5.62}$$

where A matrices are associated to FE portion and therefore, highly sparse matrices. Z matrices are the fully populated matrices resulted from moment method over the boundary integral on the top and bottom discretized periodic unit cell. f are the excitation field both in the FE and BI parts. Due to the periodic boundary condition and periodic Green's function, the matrices in (5.62) are non-symmetric and all the elements have to be computed separately which means the complexity of matrices in the BI portion are of the order of $\mathcal{O}(n_s^2)$ with n_s the number of edge elements over the BI and the complexity of the FE portion is of the order of $\mathcal{O}(n_v)$ with n_v the number of volume edges.

6. Sturm Liouville problems and eigenmode decomposition

In section 5, the application of BI equations over the open boundary was investigated to model the radiation condition effectively. For a known excitation, the computation of the scattered field needs to implement the impulse response of the scatterer to the spatial point dipole excitation. Afterwards, the scattered field to every arbitrary excitation can be computed through the integration over the source.

On the other hand, by modal analysis synthesized in chapter 4, electromagnetic fields in inhomogeneously filled waveguide were represented as superposition of eigenmodes. As it was shown, this method for solving eigenvalue problems leads to difficulties in open regions (one or both domain endpoints at infinity), since the mode spectra may then be continuous and the eigenfunction becomes improper. Furthermore, the suggested PML termination has approximations which need to consider the excluded improper modes like as Berenger modes.

A more powerful and direct technique is provided by the characteristic Green's function procedure based on the connection between source free resonant solutions (eigenfunction) and the traveling wave response to point source excitation. This connection is known as the Sturm-Liouville theorem for differential equations. The Sturm-Liouville differential equation is in the form of

$$[\frac{d}{dx}p(x)\frac{d}{dx} - q(x) + \lambda_m w(x)]f_m(x) = 0, \quad x_1 \leqslant x \leqslant x_2, \tag{6.1}$$

where f_m is the eigenfunction and λ_m is the corresponding eigenvalue. The equation is solved subjected to the homogeneous boundary condition at $x = x_{1,2}$ in the form of $p\frac{df_m}{dx} + \alpha_{1,2}f_m = 0$. p , q and the weight function w are assumed to be piecewise continuous functions of x in the solution domain. The orthogonality relation is derived in a method like as the 2D vector eigenfunctions in (4.16) where the integration is performed with respect to the weight factor

$$(\lambda_m - \lambda_n) \int_{x_1}^{x_2} w\ f_m\ f_n^*\ dx = 0 \quad m \neq n. \tag{6.2}$$

By this eigenmode computation, the completeness relation is read as

$$\frac{\delta(x - x')}{w(x')} = \sum_m f_m(x)\ f_m^*(x), \quad x_1 < \begin{matrix} x \\ x' \end{matrix} < x_2, \tag{6.3}$$

therefore, the Green's function of this equation can be decomposed based on the eigenfunctions with

$$g(x, x'; \lambda) = -\sum_m \frac{f_m(x)\ f_m^*(x')}{\lambda_m - \lambda}, \tag{6.4}$$

which is concluded from the Cauchy's theorem

$$\frac{\delta(x - x')}{w(x')} = -\frac{1}{2\pi \mathrm{j}} \oint_c g(x, x'; \lambda) d\lambda. \tag{6.5}$$

The assumptions above are that the eigenvalue spectrum is simple and discrete. As it is inferred from (6.4), the poles of the Green's function are the discrete eigenvalues of the Sturm-Liouville problem (6.1).

6.1. Semi-infinite solution domain

As the interval of (6.1) becomes semi-infinite or infinite, the eigenvalues of the Sturm-Liouville are no longer only discrete values. These Sturm-Liouville problems of type 3 [Dudley, 1994] are called open boundary problems. In this case the delta representation (6.3) is written based on the both discrete and continuous spectrum eigenfunctions as

$$\frac{\delta(x - x')}{w(x')} = \sum_m f_m(x)\ f_m^*(x') + \int_{-\infty}^{+\infty} f_\nu(x, \lambda_\nu) f_\nu^*(x', \lambda_\nu) d\nu. \tag{6.6}$$

To illustrate the application of this method, the simplest open boundary problem is a homogeneous dielectric slab waveguide, Fig. 6.1. To obtain the eigenmodes for reconstructing the Green's function in this structure, the best

choice for a complete basis is a set of modes transverse to z namely TE^z and TM^z modes. This presentation results in two alternatives for dyadic Green's function [Michalski and Zheng, 1990]. The goal in this thesis is not to formulate the Green's function nevertheless the knowledge of the singularities needs the derivation methods of Green's function. The most common form of the dyadic Green's function for the electric potential is

$$\overline{\overline{G}}(r,r') = \begin{bmatrix} G_{xx} & 0 & 0 \\ 0 & G_{yy} & 0 \\ G_{zx} & G_{zy} & G_{zz} \end{bmatrix} \tag{6.7}$$

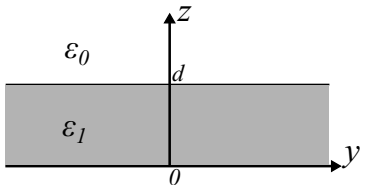

Figure 6.1.: A dielectric slab waveguide in an infinite background.

Every component of the dyadic Green's function (6.7) is obtained by the assumption of the free space delta representation based on the TE or TM scalar eigenfunctions [Felsen and Marcuvitz, 1994]

$$\begin{aligned} \mathbf{\Phi}_i(\boldsymbol{\rho}) &= \frac{1}{2\pi} \mathrm{e}^{-\mathrm{j}(k_x x + k_y y)}, \quad -\infty < k_x < \infty, \quad -\infty < k_y < \infty; \\ k_{ti}^2 &= k_x^2 + k_y^2. \end{aligned} \tag{6.8}$$

where k_{ti} is the transverse wavenumber. The delta representation in two dimensions is therefore as

$$\begin{aligned} \delta(\boldsymbol{\rho} - \boldsymbol{\rho}') = \sum_i \mathbf{\Phi}_i(\boldsymbol{\rho}) \mathbf{\Phi}_i^*(\boldsymbol{\rho}') = \frac{1}{4\pi^2} \int_{-\infty}^{+\infty} dk_x \int_{-\infty}^{+\infty} dk_y \mathrm{e}^{-\mathrm{j}(k_x x + k_y y)} \mathrm{e}^{+\mathrm{j}(k_x x' + k_y y')}, \\ -\infty < \begin{matrix} x \\ x' \end{matrix} < \infty, \quad -\infty < \begin{matrix} y \\ y' \end{matrix} < \infty. \end{aligned} \tag{6.9}$$

These scalar free space eigenfunction then are used in the multilayer structures to compute for the Green's function by applying appropriate boundary conditions.

6.2. Green's function of layered media

Consider a layered medium as Fig. 6.2 in which every layer is a homogeneous dielectric medium. The traveling waves (eigenfunctions) are considered as plane waves as it was explained in the previous section. By this assumption it is possible to utilize the transmission line model for every layer

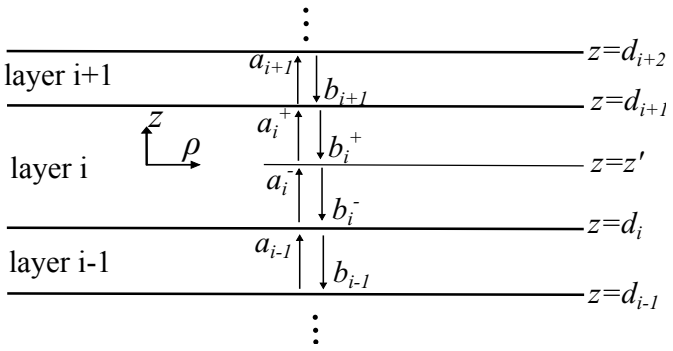

Figure 6.2.: A multilayer dielectric medium in an infinite background.

$$-\frac{d}{dz}U^i(z) = \mathrm{j}k_{zi}Z_iI^i(z), \tag{6.10}$$

$$-\frac{d}{dz}I^i(z) = \mathrm{j}k_{zi}Y_iU^i(z), \tag{6.11}$$

where $Z_i = 1/Y_i$ and k_{zi} are respectively the wave impedance and the wavenumber in layer i, U^i is equivalent to the electric field amplitude and I^i is equivalent to the magnetic field amplitude. By considering the electric or magnetic source at $z = z'$ the dyadic Green's function can be obtained. The waves in layered media are considered as plane waves. Therefore, the general response for the electric and magnetic fields can be obtained as the superposition of incoming and outgoing waves in every layer

$$U^i(z) = A_i\mathrm{e}^{-\mathrm{j}k_{zi}} - B_i\mathrm{e}^{+\mathrm{j}k_{zi}}, \tag{6.12}$$

$$I^i(z) = Y_iA_i\mathrm{e}^{-\mathrm{j}k_{zi}} + Y_iB_i\mathrm{e}^{+\mathrm{j}k_{zi}}. \tag{6.13}$$

Applying the continuity of the fields at the boundaries of the layers results in the Green's function for layered medium. However these Green's functions

depend on the orientation of the source. For vertical and horizontal electric and magnetic dipoles, the complete Green's functions can be found in [Dural and Aksun, 1995]. For example the vector electric potential of a horizontal electric dipole at the same layer of the source is in the form of

$$\hat{G}_{xx}^{A} = \frac{\mu_i}{2\mathrm{j}k_{zi}}[\mathrm{e}^{-\mathrm{j}k_{zi}|z|} + A_h^e \mathrm{e}^{\mathrm{j}k_{zi}z} + C_h^e \mathrm{e}^{-\mathrm{j}k_{zi}z}]. \tag{6.14}$$

A_h^e and C_h^e are combination of reflection and transmission coefficients from layers above and below the source layer. For the source and observation points in different layers, the relation between the field amplitudes in two adjacent layers is obtained as

$$a_j^- = a_{j+1}^- \frac{t_{j+1,j}\mathrm{e}^{-\mathrm{j}(k_{z_{j+1}} - k_{z_j})(h+z_{-m+1})}}{1 - r_{j,j+1}R_{j,j-1}\mathrm{e}^{-\mathrm{j}k_{zj}2d_j}}, \tag{6.15}$$

and

$$a_j^+ = a_{j-1}^+ \frac{t_{j-1,j}\mathrm{e}^{-\mathrm{j}(k_{z_{j-1}} - k_{z_j})(z_{m-1}+d_j-h)}}{1 - r_{j,j-1}R_{j,j+1}\mathrm{e}^{-\mathrm{j}k_{zj}2d_j}}, \tag{6.16}$$

where $t_{j+1,j}$ is the Fresnel's transmission coefficient of the plane wave passing from the layer $j+1$ to layer j and $r_{j,j+1}$ is the Fresnel's reflection coefficient of the plane wave from layer the $j+1$ to layer j and $R_{j,j+1}$ is the generalized reflection coefficient at the interface of the layers j and $j+1$. z_m is the distance between the source layer i and layer j with $m = i - j$. Therefore, starting from the source layer, the field expression for other layers can be found.

The reflection coefficient given in (6.15) and (6.16) and the Green's function (6.14) are all in the spectral domain. From (6.9), the procedure of converting the spectral domain to time domain needs the integration over real wavenumbers which is called Sommerfeld integration path. The important point in our application to compute the dispersion diagram, is computing for the singularities of the Green's function. From (6.14), it can be concluded, for a general stratified layered medium, generalized reflection and transmission coefficients have the same poles of the Green's function. On the other hand, from the Sturm-Liouville equations, they are the same as the desired eigenvalues. In the next section the reflection and transmission coefficients for a slab waveguide and corresponding eigenvalues are studied.

6.3. Homogeneous slab waveguide

The reflection and transmission coefficients from a slab waveguide, Fig. 6.1, can be written in the form of

$$R = \frac{r(1 - \mathrm{e}^{-2\mathrm{j}k_{z_1}d)}}{1 - r^2\mathrm{e}^{-2\mathrm{j}k_{z_1}d}}, \tag{6.17}$$

$$T = \frac{(1 - r^2)\mathrm{e}^{-2\mathrm{j}k_{z_1}d}}{1 - r^2\mathrm{e}^{-2\mathrm{j}k_{z_1}d}}, \tag{6.18}$$

where for TM modes $r = \frac{k_{z_1}/\varepsilon_r - k_{z_0}}{k_{z_1}/\varepsilon_r + k_{z_0}}$. k_{z_1} and k_{z_0} are the wavenumbers in the z direction inside the slab and in free space. For TE modes $r = \frac{k_{z_1}/\mu_r - k_{z_0}}{k_{z_1}/\mu_r + k_{z_0}}$. It can be seen that the denominators of the generalized reflection and transmission coefficients in a slab waveguide are the same. This denominator is known as the characteristic function of the slab. Therefore, the poles of the reflection coefficient can be computed as discrete values from the following equation for TM modes

$$k_{z_1}/\varepsilon_r \tan(k_{z_1}d/2) \;=\; k_{z_0}, \tag{6.19}$$

$$k_y^2 + k_{z_1}^2 \;=\; \omega^2\varepsilon_r\varepsilon_0\mu_0, \tag{6.20}$$

$$k_y^2 - k_{z_0}^2 \;=\; \omega^2\varepsilon_0\mu_0. \tag{6.21}$$

6.3.1. Surface waves in slab waveguide

Solving equations (6.19)-(6.21) for real wavenumbers will result in the tangential wavenumber k_y for every given frequency. To solve these coupled nonlinear equations, the Newton-Raphson method can be employed. The other schematic method is observing the intersection of (6.19) with a curve resulted from substituting (6.20) into (6.21) as shown in Fig. 6.3. The circles are foot prints of iso-frequency equations yielded by combining (6.20) and (6.21).

For every frequency, as is shown, there is at least one response for positive k_{z_0}. These discrete modes are called proper modes since the positive k_{z_0} is equivalent to the decaying wave in free space. The response for $k_{z_0} < 0$ is called improper where the resulting mode is growing in free space.

The dispersion curves for sweeping the frequency for TM and TE modes are depicted in Fig. 6.4. These discrete modes are called surface wave modes, since they are confined into the slab thickness. The tangential wavenumber k_y

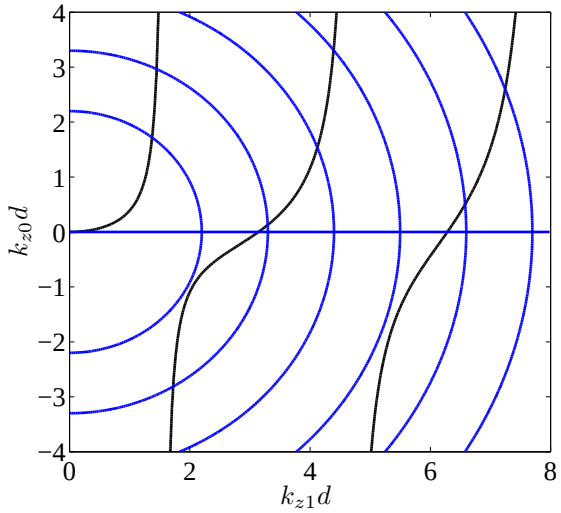

Figure 6.3.: Intersection of tangent and iso-frequency circles for a slab waveguide with d= 3.5 mm and ε_r=4.

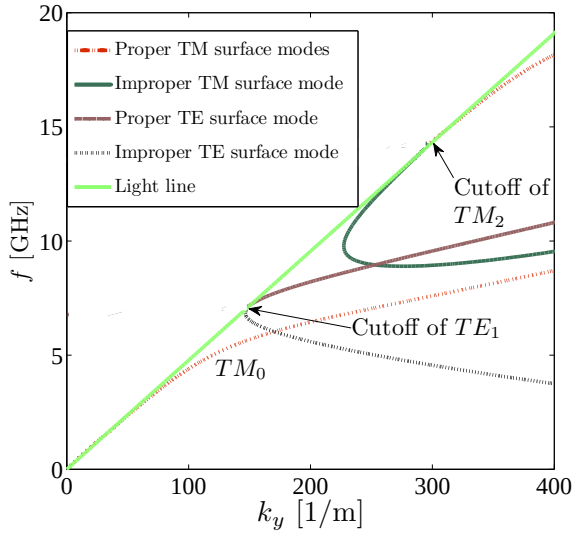

Figure 6.4.: Dispersion diagrams for a slab waveguide with d= 7 mm and ε_r=10.5.

for these modes is always greater than the free space wavenumber k_0 therefore, the dispersion curves only exist after the light line in the dispersion diagram.

6.3.2. Leaky waves in slab waveguide

Solving the coupled equations (6.19)-(6.21) for complex values of wavenumbers results into another interesting set of modes known as leaky modes. As can be observed from Fig. 6.3, there exist frequencies for modes higher than TM_0 where the circles are becoming tangential to the tangent curves. These frequencies however exist at the lower plane of k_{z0}. By reducing the frequency from this point, the complex wavenumbers are appeared in the solution of the coupled equation. Therefore, to solve the coupled characteristics equations by the Newton-Raphson method, the initial guess is the point where two curves are tangential. This point is equivalent to the minimum of the improper mode curve in the dispersion diagram, Fig. 6.4. It can be inferred from Fig. 6.4, TM_0 and TE_1 modes don't have any minimum, therefore they will not have any complex eigenvalue. In Fig. 6.5 the dispersion diagram of complex modes are computed for TM_2 mode.

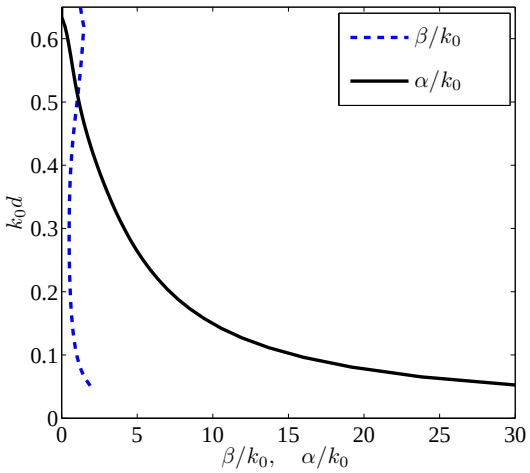

Figure 6.5.: Dispersion diagrams for complex TM_2 mode in a slab waveguide with d= 7 mm and ε_r=10.5.

The response is in the form of $k_y = \beta - \mathrm{j}\alpha$ where $\beta/k_0 = 1.4$ at 8.6 Ghz as the initial guess which corresponds to the minimum of the TM_2 dispersion curve.

7. Open structure analysis

7.1. Excitation of eigenmodes

The method of external excitation of eigenvalues has been proposed in [Reutskiy, 2010] and [Reutskiy, 2008]. This method solves the eigenporblem of a generalized Sturm-Liouville equation by applying an external excitation and maximizing the norm of the mean value of the response with respect to the eigenvalues. The particular property of these methods is that they do not need to solve the eigenproblem algebraically but seeking among the repeated solution of the excitation problem. In analogy with resonators, the method of internal excitation has been employed to look for eigenvalues of periodic unit cells in closed and open structures in [Eibert et al., 2012].

The internal excitation method has been extensively utilized in cavity resonators [Matthaei et al., 1963]. In these applications, to excite a distinct mode, depending on the field distribution of the desired mode, an appropriate probe is employed to couple the electromagnetic energy to the cavity. Normally two types of probes are utilized in microwave engineering applications known as electric probe and magnetic probe. The electric probe is positioned at the locations where the mode has electric field parallel to the probe. The magnetic probes, also known as loop currents , are positioned at the locations where the magnetic field of the desired mode is perpendicular to the surface of the loop. Aperture coupling is another type of excitation where from the equivalence theorem, the magnetic current over the open aperture is responsible for energy coupling between the two sides of the aperture. Normally, the coupling type is decided based on the strongest field component. Besides the internal excitation, external excitation is also performed based on the coupling of modes.

In this section the introduced method based on the scattering of electromagnetic waves is implemented in order to investigate the behavior of periodic metamaterials. This method is categorized as the method of external excitation. The goal is to compute the eigenvalues of the unit cell by excitation.

As it was shown in previous chapter, the eigenmodes of the layered media are in the form of plane waves. Moreover, metamaterial periodic stratified structures are to be investigated in this thesis. Approximation of these material by layered media allows us to consider the excitation of eigenmodes as plane

waves.

7.2. Plane wave excitation of layered media

As an external excitation for layered media, plane waves can be the best candidates. This enables the simpler wave decomposition in both free space and layered medium. Especially, considering the Berenger (PML) modes to account for the open boundary approximating the continuous spectrum is not needed anymore. As it was shown in section 6.3, modes in homogeneous layered media are real surface wave or complex leaky modes. The real surface wave modes are confined into the layers of the medium.

As it was shown in Fig. 6.4, surface wave modes have tangential wavenumbers as $k_t > k_0$. The corresponding plane waves to be coupled to these surface wave modes have the transverse wavenumbers as $k_z = \pm \mathrm{j}\sqrt{k_t^2 - k_0^2}$. The sign of imaginary wavenumber indicates an evanescent or growing plane wave which results in proper or improper surface wave mode. With respect to the time dependence of $\mathrm{e}^{\mathrm{j}\omega t}$ and spatial dependence of $\mathrm{e}^{-\mathrm{j}\boldsymbol{k}\cdot\boldsymbol{r}}$, the minus sign will indicate the proper modes and the plus sign will indicate the improper modes. Therefore, with these definitions, when $\Im(k_z) < 0$ the modes are proper and when $\Im(k_z) > 0$ modes are improper.

Consider the TM_0 mode in a slab waveguide with thickness 7 mm and $\varepsilon_r = 10$. The reflection and transmission coefficients of the TM_0 mode have been swept for evanescent waves at 7 GHz in Fig. 7.1. As it is observed, at $k_x/k_0 = 1.68$ there is a singularity in both reflection and transmission coefficients. This value is satisfying the dispersion characteristic of (6.19)-(6.21) which indicates the excitation of TM_0 surface wave mode. It should be noted that a slab waveguide is a symmetric structure in both x and y direction henceforth we have considered the $k_t = k_x$ and $k_y = 0$.

The field distribution inside and outside of the slab at 7 GHz and $k_x/k_0 = 1.68$ are shown in Fig. 7.2. The present field components, as it is seen, are E_z, E_x and H_y which confirm the excitation of TM_0 mode. From the distribution of H_y it is clear that the field has a maximum at the center of the slab.

The field components of the TM mode are related to each other through the following relations

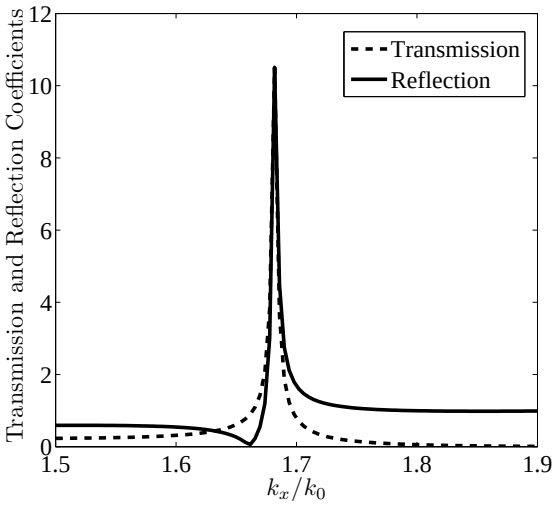

Figure 7.1.: The reflection and transmission coefficients of the evanescent plane wave incident onto a slab waveguide with d= 7 mm and ε_r=10.

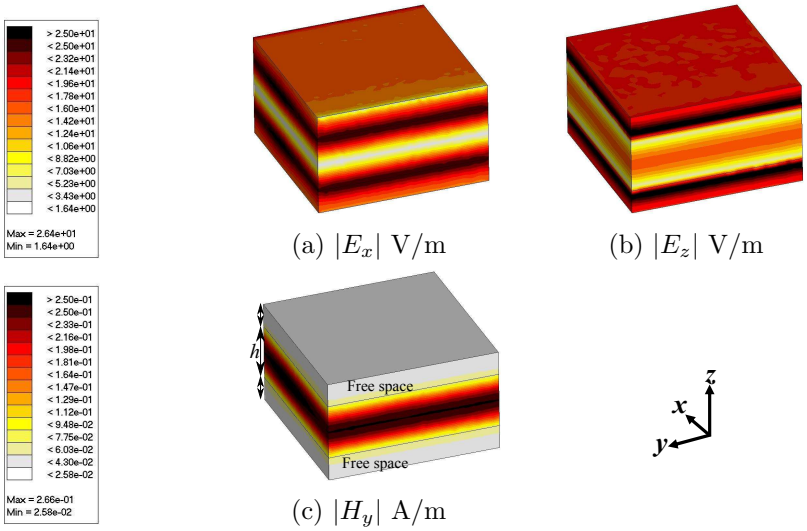

(a) $|E_x|$ V/m (b) $|E_z|$ V/m

(c) $|H_y|$ A/m

Figure 7.2.: Distribution of electric and magnetic fields of TM_0 mode inside and outside of the slab waveguide at 7 GHz and k_x/k_0=1.68, h = 7 mm, ε_r = 10.

$$E_z = \frac{-k_x}{\omega\varepsilon}\frac{\partial\psi}{\partial z} \tag{7.1}$$

$$E_x = \frac{1}{\mathrm{j}\omega\varepsilon}(k^2 - k_x^2)\psi \tag{7.2}$$

$$H_y = -\frac{\partial\psi}{\partial z} \tag{7.3}$$

where for TM_0 mode $\psi = A\cos(\sqrt{\omega^2\mu_0\varepsilon_0\varepsilon_r - k_x^2}z)\mathrm{e}^{-\mathrm{j}k_x x}$ inside the slab and $\psi = B\mathrm{e}^{-\sqrt{k_x^2-\omega^2\mu_0\varepsilon_0}|z|}\mathrm{e}^{-\mathrm{j}k_x x}$ outside the slab. The above equations also confirm the field distribution of Fig. 7.2. The interesting point in the field distribution of this surface wave mode is the electric field intensity has two maxima outside the slab and after these maxima the field is decaying very fast. In the next sections it is shown that this behavior is adequate for near field imaging.

7.2.1. Excitation of complex leaky modes in slab waveguide

To excite the leaky modes, the required wavenumbers are complex. In terms of plane waves, these waves are inhomogeneous plane waves which decay or grow while propagating. As it was mentioned in section 6.3, the dispersion diagram of the complex mode is starting from the minimum of the improper surface wave mode curve. Thus, the TM_0 mode has no complex part. Therefore the complex mode for TM_2 is computed.

For a slab of 7 mm thichness and $\varepsilon_r = 10$, the minimum of TM_2 dispersion curve is at 8.9 GHz and $\frac{k_x}{k_0} = 1.48$. Consequently, for a frequency less than 8.9 GHz the complex mode can be excited.

In the computation of the transmission and reflection coefficients by FEBI method, since the slab waveguide is a homogeneous structure, the scattered field from the unit cell only contains the fundamental Floquet mode and all higher order modes have the coefficient of zero. Henceforth, the scattered field in the upper side of the slab, where the incident field is illuminating the slab, will represent the reflection coefficient and at the bottom it is the same as transmission coefficient.

In Fig. 7.3, the transmission coefficient computed by FEBI method has been swept at 8.8 GHz for wavenumbers $\frac{k_{x_{real}}}{k_0} \in [1.44, 1.48]$ and $\frac{k_{x_{imag}}}{k_0} \in [-0.2, 0.2]$. As it is observed, there exist two singularities in the reflection coefficient. These two singular values are a complex conjugate pair. This behavior can be explained by complex function analysis. It should be noted that these singular values are observed in the reflection coefficient also.

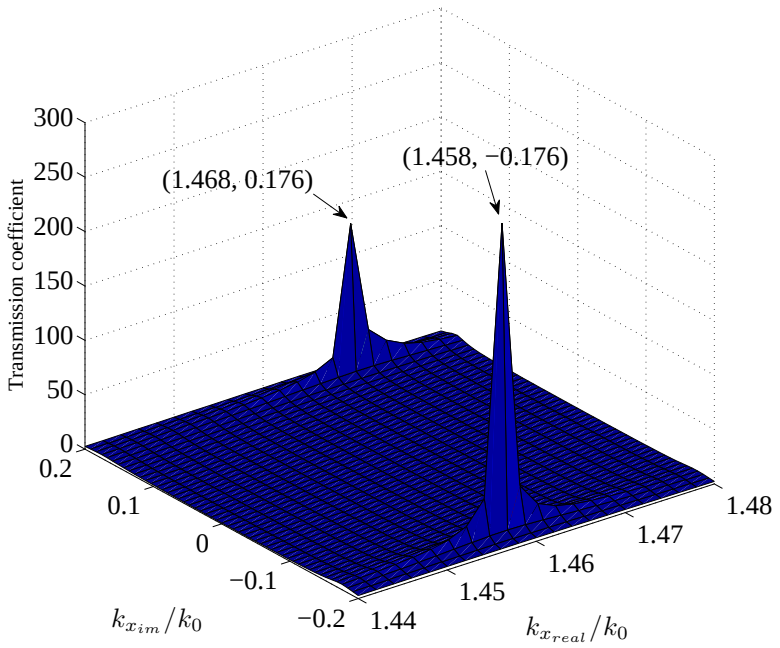

Figure 7.3.: Transmission coefficient of the inhomogeneous plane wave incident onto a slab waveguide with d= 7 mm and ε_r=10 at 8.8 GHz.

As it was discussed in section 4.3 for closed waveguides, in every eigenvalue equation in the form of $H(k_t, \omega) = 0$, the general response is in the form of complex pair of (k_t, ω) where each of variables can be complex [Hanson and Yakovlev, 1998]. In this thesis, the frequency is considered as real values but the wavenumber k_t is allowed to be complex. By this assumption, if k_t fulfills the dispersion equation, then $-k_t$, k_t^* and $-k_t^*$ also meet the same equation. The accuracy in the computation of the scattered field in FEBI method, strongly depend on the number of discretizations. The slight difference between the real part of the two conjugate pairs in Fig. 7.3 is due to this discretization.

By sweeping the frequency for proper and improper real modes as well as complex modes, the dispersion diagram of the TM_2 mode has been calculated as Fig. 7.4. The results from FEBI are compared with the results directly obtained from the solution of dispersion equations (6.19)-(6.21) by Newton-Raphson (NR) method. As it is observed, the theoretical solution of the dispersion

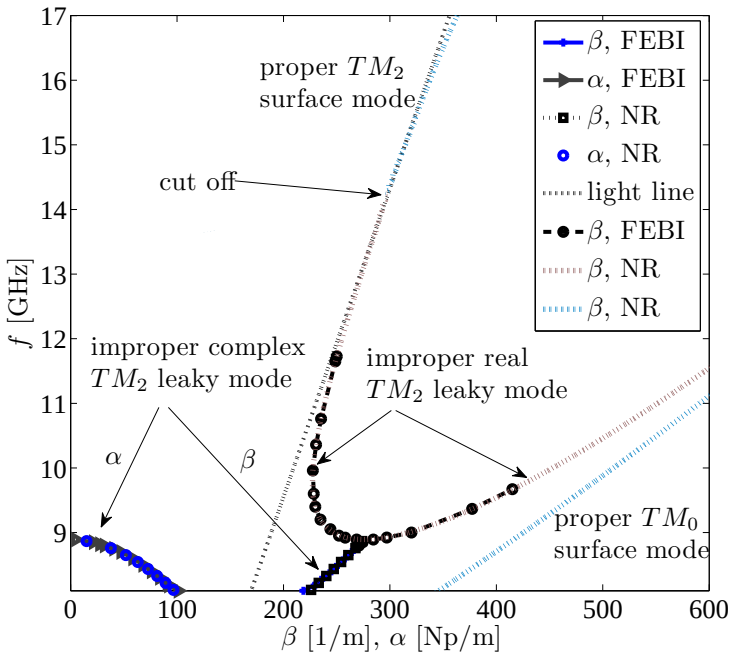

Figure 7.4.: Dispersion diagram of the improper leaky wave TM_2 and proper surface wave TM_0 and TM_2 modes for a slab waveguide with d= 7 mm and ε_r=10 computed by finite element boundary integral (FEBI) and Newton-Raphson (NR) methods.

equation is exactly the same as that one obtained by FEBI method.

7.3. Scattering from one sided open structures : absorption and minimum scattering, cloaking

Most of the guided wave open structures in microwave engineering are realized by microstrip technology which has the advantage of low weight and easy fabrication. The dielectric layer in these structures is terminated by a ground plane. Evaluating the Green's function in the spatial domain result in the Sommerfeld integrals which are time consuming. Therefore, several methods to approximate the Green's function have been introduced. Among them is the discrete complex image method [Fang et al., 1988, Ling and Jin, 2000] which uses the approximation of the kernel of the Sommerfeld type integrals by a

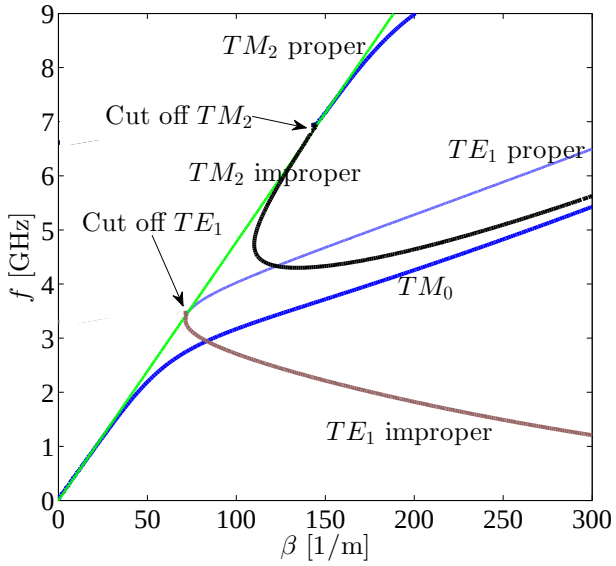

Figure 7.5.: Dispersion diagram of the surface wave modes for a grounded slab waveguide with $d = 7$ mm and $\varepsilon_r = 10.5$ computed by Newton-Raphson (NR) method.

series of exponential functions with different complex coefficients. Physically, each term of the series represents a discrete image with complex amplitude and location. The moment method for the analysis of the structures is utilizing then the approximated Green's function to accelerate the computations.

In this section, the scattering of inhomogeneous plane wave from grounded slab wavegudies is investigated. Consider a grounded slab waveguide with thickness $d = 7$ mm and $\varepsilon_r = 10.5$. The dispersion diagram of the proper and improper surface wave modes is computed by the Newton-Raphson solution of the dispersion equation for the grounded slab shown in Fig. 7.5.

Comparing the dispersion diagrams in Fig.s 6.3 and 7.5, the cutoff frequencies of the grounded slab are half of the slab waveguide's cutoffs which is due to the symmetric field distribution in the z direction. To excite the TM_0 mode like the procedure taken in previous section, the evanescent wave is employed. An evanescent TM plane wave has been swept over the real tangential wavenumbers as $k_t = k_y$ and $k_x = 0$ in Fig. 7.6. The singularity is observed at $\frac{k_y}{k_0} = 2.52$ and $f = 5$ GHz. The field distribution of the excited TM_0 mode is shown in Fig. 7.7.

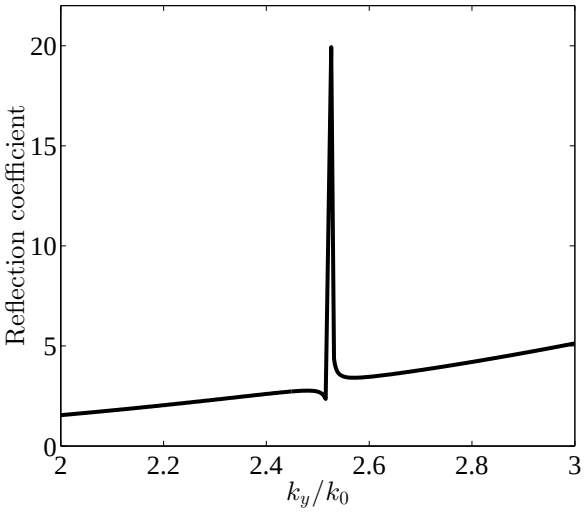

Figure 7.6.: Reflection coefficient of the incident evanescent plane wave from a grounded slab waveguide with $d = 7$ mm and $\varepsilon_r = 10.5$ computed by FEBI method.

As it was already explained, TM_0 mode has no improper part. Also, the dispersion curve of the improper TE_1 mode has no minimum. Therefore, the first mode which has the complex leaky part is TM_2 mode. The minimum of TM_2 mode in this slab is occurring at 4.27 GHz. To show the complex behavior of the leaky mode, the reflection coefficient of incident inhomogeneous plane wave is calculated by the FEBI method for the $\frac{k_{y_{real}}}{k_0} \in [-1.47, -1.45]$ and $\frac{k_{y_{imag}}}{k_0} \in [-0.2, 0.2]$ at 4.26 GHz. As it is observed in Fig. 7.8, the detected singular values are exactly complex conjugate of each other.

An interesting behavior of these grounded structures is the zeros observed in the reflection coefficient. The reflection coefficient of the plane wave from a grounded slab with thickness d and relative permittivity of ε_r is

$$R = \frac{1 + r\mathrm{e}^{2\mathrm{j}k_{z1}d}}{1 + r\mathrm{e}^{-2\mathrm{j}k_{z1}d}} \tag{7.4}$$

where for TM incident wave $r = \frac{k_{z1}/\varepsilon_r - k_{z0}}{k_{z1}/\varepsilon_r + k_{z0}}$ with k_{z1} the wavenumber inside the slab and k_{z0} the wavenumber in free space. Simplifying both the numerator and denominator of the reflection coefficient respectively result in

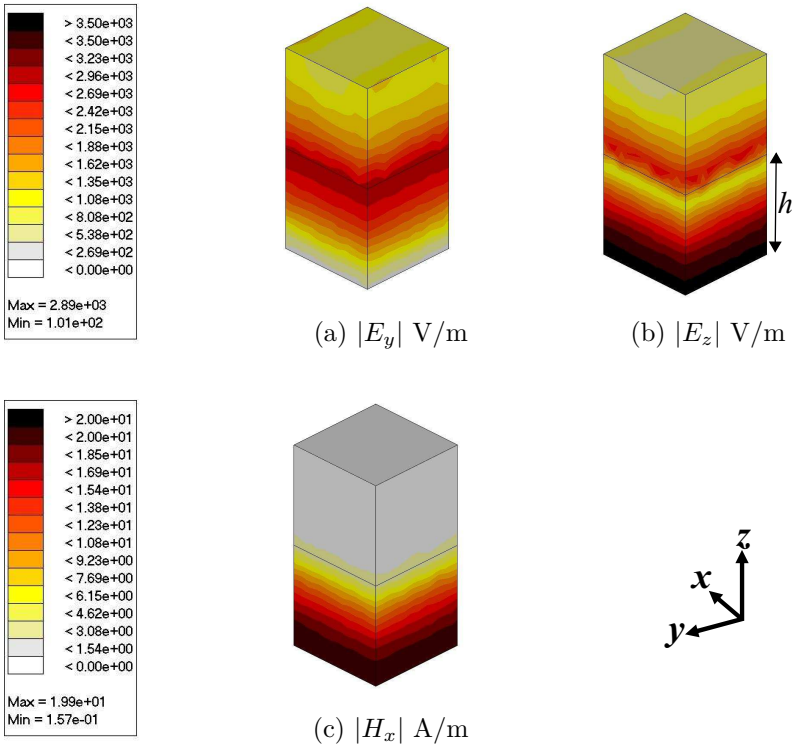

(a) $|E_y|$ V/m (b) $|E_z|$ V/m

(c) $|H_x|$ A/m

Figure 7.7.: Distribution of electric and magnetic fields of TM_0 mode inside and outside of the grounded slab waveguide at 5 GHz and k_y/k_0=2.52, h = 7 mm, ε_r = 10.5.

$$\frac{k_{z1}}{\varepsilon_r}\tan(k_{z1}d) - k_{z0}, \tag{7.5}$$

$$\frac{k_{z1}}{\varepsilon_r}\tan(k_{z1}d) + k_{z0}. \tag{7.6}$$

With a simple mathematical manipulation it can be perceived that the dispersion equation of numerator and denominator of the reflection coefficient have the same complex responses. However, since in the reflection coefficient the poles result in the infinity in the scattered field, zeros of the reflection are not observable. To make the zeros observable, a slight loss is added to the permittivity of the slab waveguide. The loss will degrade the location of the poles and zeros in different directions, since the equations for poles and zeros

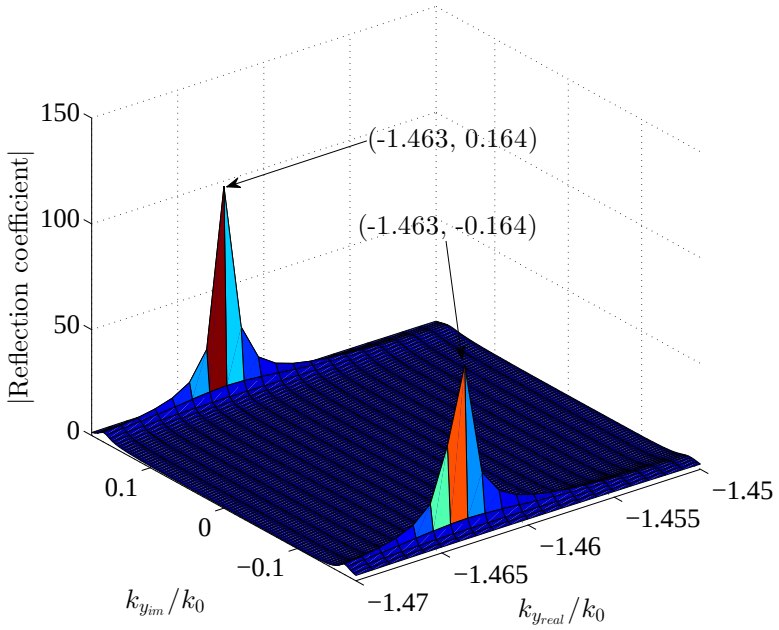

Figure 7.8.: Reflection coefficient of the incident inhomogeneous plane wave from a grounded slab waveguide with $d = 7$ mm and $\varepsilon_r = 10.5$ computed by FEBI method.

are not the same. The reflection coefficient of the inhomogeneous plane wave from a lossy grounded slab waveguide with $\varepsilon_r = 10.5 - \mathrm{j}0.03126$ at 3.85 GHz is depicted in Fig. 7.9. As it is shown, rather than the poles in Fig. 7.9a, there exist two zeros where for better appearance of zeros the inverse of the reflection coefficient is drawn in Fig. 7.9b.

The effect of the zeros in the fast wave region of the dispersion diagram is more interesting. Recently, scattering from random rough surfaces is becoming more popular. It is often assumed that the incident field is a homogeneous plane wave for the simplification of the analysis. Especially, for controlling the propagation and transmission of the wave in a spectrum and demonstrate the potential to make an object invisible by periodic coverings, the analysis of the scattering of plane waves from the periodic media is helpful. However, investigating the accurate behavior of the scatterers in the complete spectrum has not been performed until now. In the following we try to demonstrate the

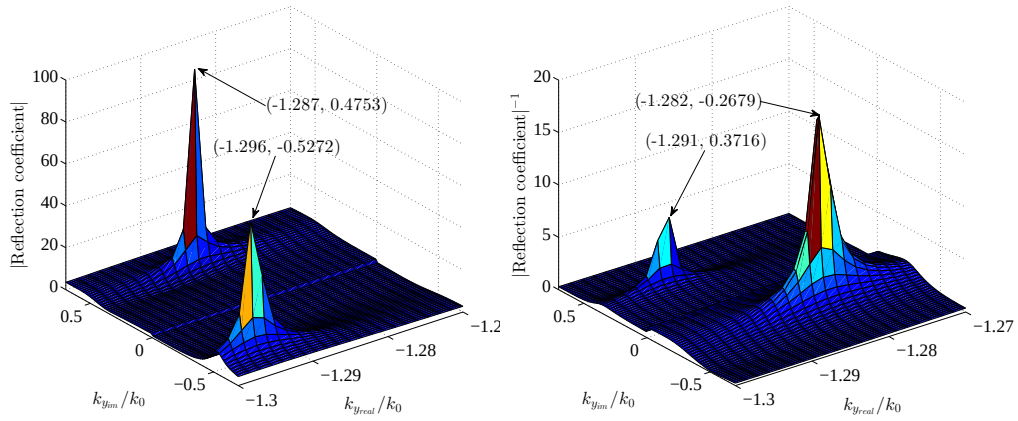

(a) Reflection coefficient.

(b) 1/|Reflection coefficient|.

Figure 7.9.: Poles and zeros of the reflection coefficient from a lossy grounded slab waveguide with $d = 7$ mm and $\varepsilon_r = 10.5 - \text{j}0.03126$ at 3.85 GHz computed by FEBI method

reason for complete absorption and cloaking by spatial modes decomposition of the scattered wave.

7.4. Riemann sheet for right handed and left handed modes

In the slow wave region, because the real part of the swept tangential wavenumber is greater than the free space wavenumber, the propagating wave is always confined to the dielectric slab. Therefore, there is no constraint on the scattered field. However, moving to the fast wave region, $\Re(k_t) < k_0$, the physical constraint on the scattered field is read as [Felsen and Marcuvitz, 1994]

$$\Im(k_z) < 0, \tag{7.7}$$

which is translated to the evanescent waves when $z \to +\infty$. These modes are called proper modes. The definition of the proper and improper modes for a stratified medium extended in $x - y$ plane only depends on the wavenumber in the z direction. The branch cuts on the Riemann sheet in a dielectric slab are

emanating from the branch points at $k_y = k_0$ by assuming that $k_t = k_y$ and $k_x = 0$.

For a complex wavenumber $k_y = \beta - \mathrm{j}\alpha$, on the top Riemann sheet where $\Im(k_z) < 0$, the right handed modes are defined as the spectrum where $\Re(k_y) > 0$ and the left handed modes are the ones with $\Re(k_y) < 0$. The relation $k_y^2 + k_z^2 = k_0^2$ between the tangential and normal complex wavenumbers outside the slab waveguide can be written as

$$k_0^2 - \beta^2 + \alpha^2 = k_{z0r}^2 - k_{z0i}^2, \tag{7.8}$$

$$\alpha\beta = k_{z0r} k_{z0i}, \tag{7.9}$$

where $k_{z0} = k_{z0r} + \mathrm{j}k_{z0i}$ is the wavenumber normal to the slab surface in the free space. By this assumption the definition of proper and improper modes on the right handed and left handed parts of the top Riemann sheet is depicted in Fig. 7.10

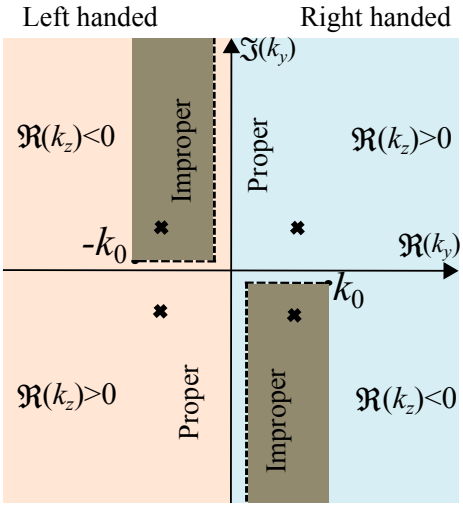

Figure 7.10.: The top Riemann sheet for complex wavenumbers.

With respect to the (7.9), the improper wavenumbers are in the fast wave region where the $\Im(k_{z0}) < 0$ and $\Re(k_{z0}) < 0$. As it is observed, this condition is met both for right handed and left handed wave propagation. In commercial softwares, the condition on tangential wavenumbers is considered as $\Im(k_y) < 0$ or equivalently $\alpha > 0$. This guarantees the evanescent waves propagating in the y direction along the waveguide while the right handed modes in the fast

wave region of this condition become improper and will be removed from the solution of a system equation.

By this explanation, from the reflection coefficient of the grounded slab waveguide, the dispersion diagram of complex leaky and surface wave modes of TM_2 mode as well as TM_0 mode are computed as shown in Fig. 7.11.

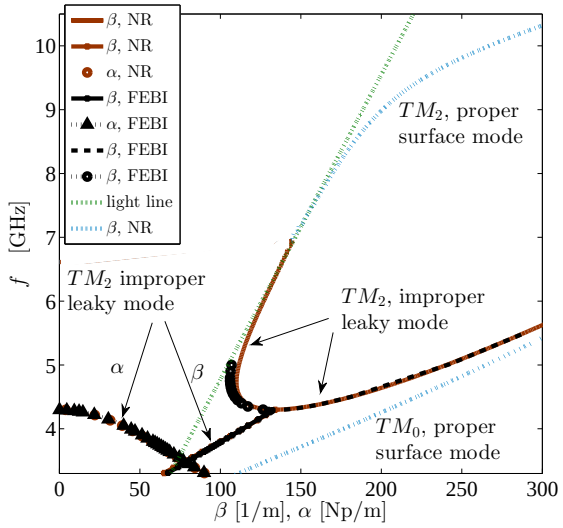

Figure 7.11.: Dispersion diagram of grounded slab with $\varepsilon_r = 10.5$ and $d = 7$ mm.

As it was explained for grounded slab waveguide in the slow wave region, in the fast wave region also there exist zeros at the same location of the poles. By removing the improper poles by applying the radiation condition on wavenumbers in fast wave region, in the location of the poles, zeros can be observable. These complex zeros, especially when there is only the fundamental Floquet mode existing in the field expansion, result in the zero scattered field from the stratified scatterer illuminated by the plane wave.

Reducing the scattered field from scatterers by covering them with artificial engineered materials is among the interests of the wave engineering. The procedure of concealing of scatterers from the external sources is known as cloaking. To our knowledge, until now all the attempts to explain this behavior have been on the experimental observation and some few researchers have explored it theoretically by introducing the concept of transmission eigenvalue that is not covered by the standard theory of eigenvalue problems for elliptic operators [Cakoni and Haddar, 2012].

7.5. Periodic open boundary structures

To realize the broadside radiation by wavegudies, the slotted wavegudies are introducing a new alternative to microstrip structures. Especially by introducing the slots to hollow wavegudies, a series capacitance is produced which together with the right handed circuit model of a hollow waveguide will result in a composite right/left hand, CRLH, behavior. The CRLH transmission lines enable the radiation from backfire to the endfire direction continuously.

7.5.1. Interdigital leaky wave antenna

A unit cell has been designed to provide the continuous beam steering for a leaky wave antenna in [Weitsch and Eibert, 2010]. This unit cell is balanced at 3.8 GHz and has a guided wave band from 3 to 6 GHz in the fast wave region. In [Weitsch and Eibert, 2010] the unit cell has been analyzed by scattering matrix approach (SMA) to compute for the eigenvalues. In this section the unit cell is investigated by scattering of plane waves by FEBI method.

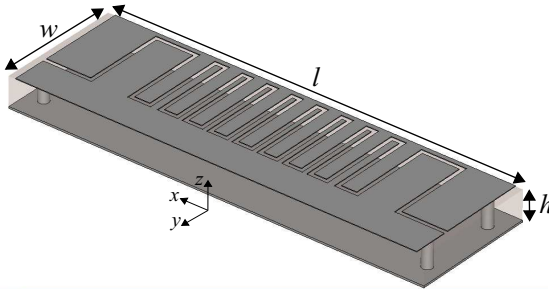

Figure 7.12.: Unit cell of an interdigital leaky wave antenna, h =1.524 mm, l = 20 mm, w = 5.9 mm, r_{via} = 0.25 mm, slot width = 0.2 mm and ε_r = 3.38. The unit cell is periodic in y direction and has open boundary in two other directions.

Since the left handed part of the dispersion diagram is starting at 3 GHz in the fast wave region, the frequencies below the 3 GHz are in the slow wave region. As it was explained is section 5.5, the periodicity is assigned by the phase shift on the periodic side walls. This condition in free space is employed by Floquet mode decomposition of the scattered field included in the periodic Green's function besides the periodic boundary condition in the finite element part. Since the incident plane wave is normalized and has the amplitude of unity, the fundamental scattered Floquet mode is representing the reflection

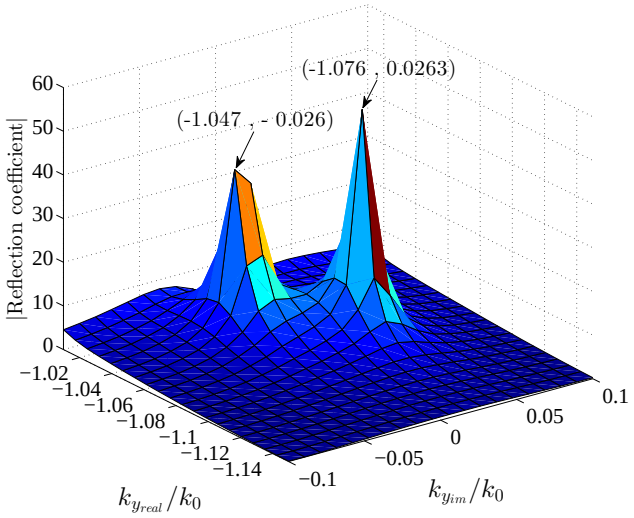

Figure 7.13.: Reflection coefficient of the fundamental Floquet mode from the leaky wave antenna unit cell at 2.96 GHz.

coefficient. By this assumptions, the reflection coefficient from the unit cell of the leaky wave antenna has been swept on complex wavenumbers in the slow wave region at 2.96 GHz, shown in Fig. 7.13. The periodicity of the unit cell is in the y direction and the excited plane wave is considered a TM wave with the field components of E_z, E_y and H_x. Therefore, the excited wavenumebr has k_y and k_z components such that $\boldsymbol{E} \cdot \boldsymbol{k} = 0$.

As it is observed from Fig. 7.13, the scattered field has two singularities which make a complex conjugate pair. Since the excited mode is in the slow wave region, both poles are observable.

To explore the singularities in the fast wave region, the swept reflection coefficient over complex wavenumbers at 3.4 GHz is shown in the Fig. 7.14. As it is depicted, only one singularity has been detected. At the location of the conjugate pair a zero is observed which is compatible to our prediction for grounded slab waveguides. As it was explained in section 7.4, for left handed modes, the proper wavenumbers are the one with $\Im(k_y) < 0$. Consequently, the improper singular value with $\Im(k_y) > 0$ is removed from the response and instead the corresponding zero is observed. This zero can be moved by adding the loss or chirality over the complex wavenumber plane. This make the zero to be observable on pure real wavenumber axis. For lossy structures it might result

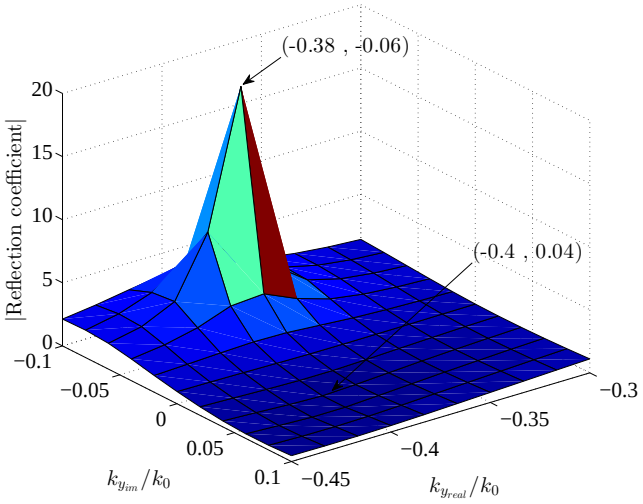

Figure 7.14.: Reflection coefficient of the fundamental Floquet mode from the leaky wave antenna unit cell at 3.4 GHz.

in the complete absorption though making the structure a chiral structure, the scattered field will have a different polarization than the incident field which does not mean the scattering reduction or complete absorption.

The dispersion diagram of the CRLH leaky wave antenna is computed for the fast wave region as shown in Fig. 7.15. The response from computation of singularities of reflection coefficient is referred to as the reflection pole method (RPM). As the reference for comparison, the results from scattering matrix approach are considered. The result of the scattering matrix approach in this figure is obtained from the computation of the eigenvalues of the fundamental mode by considering four higher order modes to compute the transmission matrix. The difficulty in the computation of the dispersion diagram by the SMA method is the reference for determining the transition frequency. In RPM method it is automatically determined by the incident wavenumber in the normal incidence.

The imaginary part of the dispersion diagram shown in Fig. 7.16 has been computed by the proposed reflection pole method compared by the matrix pencil method [Hua and Sarkar, 1989] and measurement results.

To compute the dispersion diagram faster, the search for the singularities is performed by a simplex optimization method known as Nelder-Mead which

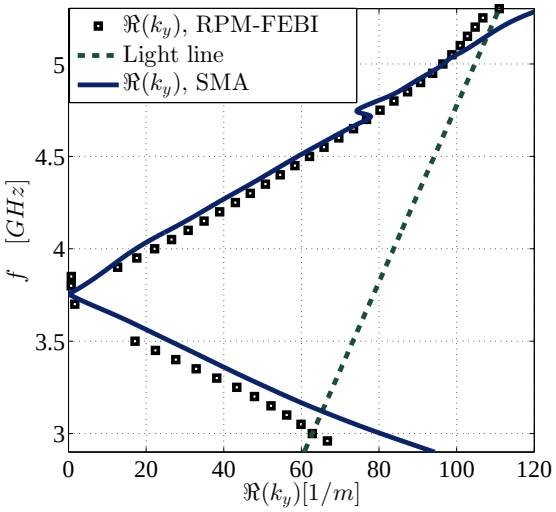

Figure 7.15.: Dispersion diagram of leaky wave antenna unit cell obtained by the FEBI analysis compared with the SMA method.

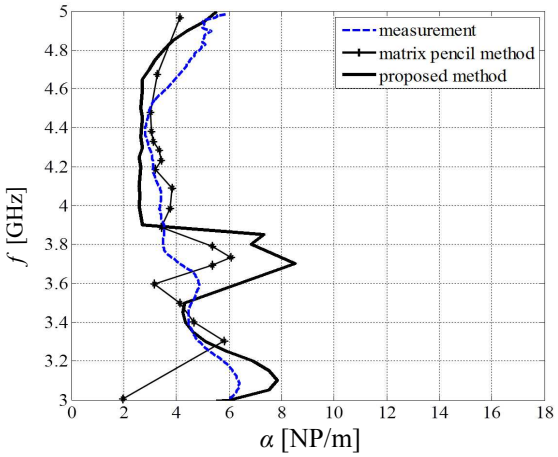

Figure 7.16.: Imaginary part of the dispersion diagram of leaky wave antenna unit cell obtained by the FEBI analysis compared with the measurement and matrix pencil approach.

searches for a local minimum of a function of several variables, see appendix A.1.

From the results of this section it can be concluded that the approximation of the periodic metamaterial stratified structures by homogeneous slab waveguide is possible for frequencies where only fundamental Floquet mode is propagating and higher order Floquet modes are evanescent. In the following some other properties of scattering from periodic structures is investigated.

7.6. Artificial ground planes

Electromagnetic band gap structures (EBG) are introducing stop bands to suppress the surface wave modes and enhance the performance of printed antennas and circuits. Among the EBG structures, artificial magnetic conductors (AMCs) are considered as the ground planes which reflect the incident field with zero reflection phase [Sievenpiper et al., 1999]. Due to the losses, it has been asserted that it is not possible to achieve the zero degree phase change, therefore, the frequency band in which the phase change is between -90° and $+90^\circ$ is considered as the band that AMC is realized [Maci et al., 2005]. In this section, the behavior of the phase and amplitude of the reflection coefficient are explored over the complex wavenumbers. Since AMC structures are among the grounded structures, only the reflection coefficient from these structures would suffice to be analyzed.

The mushroom structure Fig. 7.17, is the basic structure to realize the CRLH line. This structure is an abstraction of the corrugated surface, in which the corrugation is folded up and distributed in two dimensions. This surface impedance is modeled as parallel resonant circuit, as shown in Fig. 7.18. In the slow wave region of the open structures, they have very low leakage rate therefore, the eigenvalues of a one unit cell resonating at the wavenumbers greater than k_0 are nearly real and the singularities of the reflection coefficient can be detect by purely evanescent plane wave excitations.

The reflection coefficient of the 0th order Floquet mode from the AMC structure at 11.2 GHz is shown in the slow wave region for wavenumbers larger than k_0 in Fig. 7.19. Since the leakage is very low, two complex conjugate reflection peaks are very close to each other and the eigenvalue can be accurately detected by just sweeping the real wavenumber. As it is inferred from the reflection coefficient, the corresponding eigenvalue is around $k_y = 2.464k_0$. This AMC structure is symmetric in two dimensions and the excitation is a TM plane wave, then the periodic boundary condition is considered in y direction by sweeping k_y and the $k_x = 0$ is considered. The electric and magnetic field distributions of the excited mode, which is a left-handed TM_0 mode, are depicted in Fig. 7.20 in the yz-cut plane. As it is apparent from the field dis-

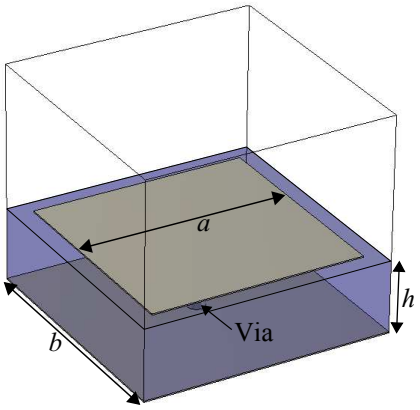

Figure 7.17.: The mushroom structure to realize an AMC ground plane, $a = 3$ mm, $b = 3.5$ mm, $h = 1$ mm, $r_{\text{via}} = 0.125$ mm and $\varepsilon_r = 2.2$.

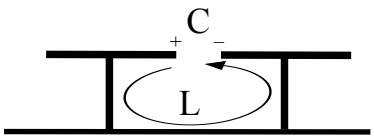

Figure 7.18.: The distributed circuit model for mushroom structure in 1D.

tribution, the circuit model introduced in Fig. 7.18 is only valid for the TM_0 mode.

Besides the surface waves in AMC structures which might affect the performance of the employing structure, the behavior of the AMC's has not been completely explored in the fast wave region until now. In [Sievenpiper et al., 1999], the fast wave region of the dispersion diagram is named as high impedance region where it is considered as band gap also. However, the reason for this behavior is not explained. In full wave simulators like as Ansoft HFSS [HFSS, 2014] and CST MWS [CST, 2014], it is possible to approximately compute the dispersion diagram in these regions by Eigenmode solution of the unit cell, yet the complete behavior of these structures has not been studied.

To explore the singularities in the fast wave region, first we find a surface wave mode higher than the TM_0 mode. The computation of the dispersion diagram is started from the slow wave region since only pure evanescent waves are required to compute for the singularities. By moving towards the fast wave region, due to leakage, the eigenvalues gradually become complex. By

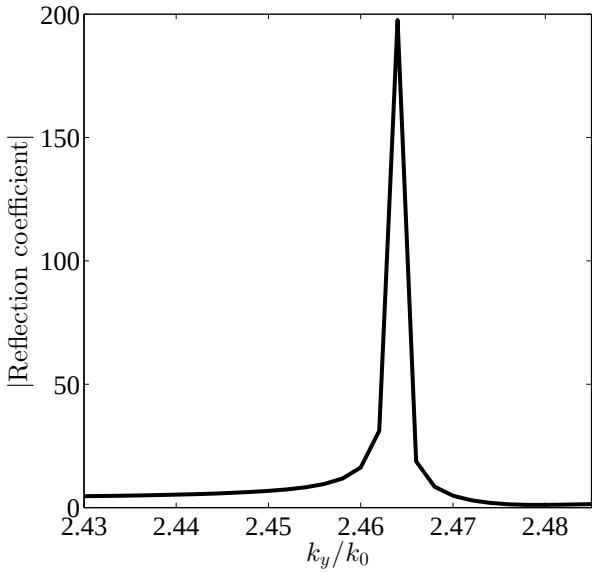

Figure 7.19.: The reflection coefficient of the fundamental Floquet mode from the AMC structure excited by evanescent waves.

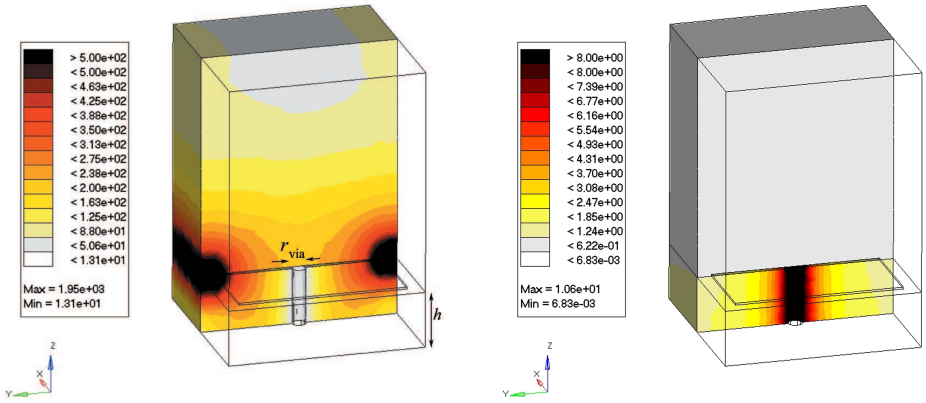

(a) E_y (b) H_x

Figure 7.20.: Field distribution of the excited TM_0 mode of the AMC structure by illuminating evanescent plane waves in the slow wave region.

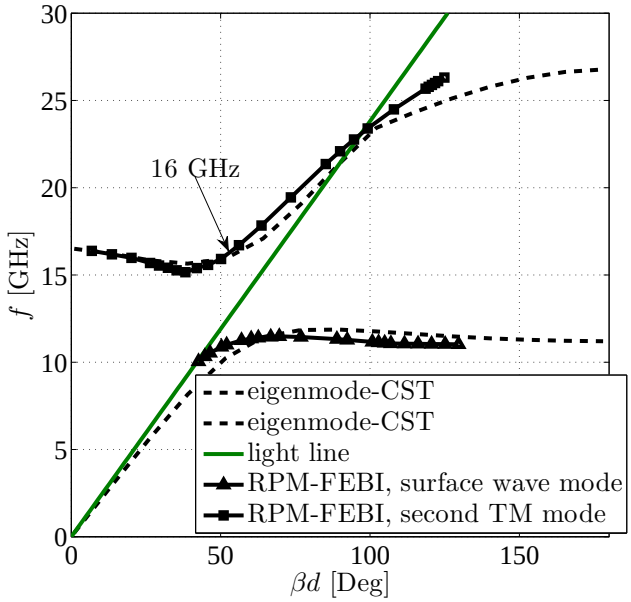

Figure 7.21.: The dispersion diagram of the mushroom structure in Fig. 7.17.

this method it will be easier to compute for the complex dispersion diagram. The dispersion diagram of the mushroom structure has been computed by the introduced method as shown in Fig. 7.21. To compute the dispersion diagram by CST Eigenmode solution, since CST Eigenmode solution does not support the open boundary, the open boundary at the top is approximated by placing a PEC boundary condition at a distance away from the top of the unit cell to not affect the field distribution and eigenvalues. Usually, a distance of quarter wavelength would suffice.

The mushroom structures, like other grounded periodic structures, have complex eigenvalues in the fast wave region. Therefore, these complex eigenvalues should be in conjugate pair. The reflection coefficient of inhomogeneous plane waves from the unit cell of the mushroom has been computed around 16 GHz in Fig. 7.22. Since the mode is behaving as a right handed mode, $(k_{real}k_{imag}) < 0$. Since the k_{imag} is always considered as a negative value, the real part of the wavenumber for the excited right handed mode is greater than zero. By this observation, it is clear that the definition of the high impedance region and band gap is not complete and the complex eigenvalues and scattering behavior of the AMC or EBG structures have to be studied more carefully. On the other

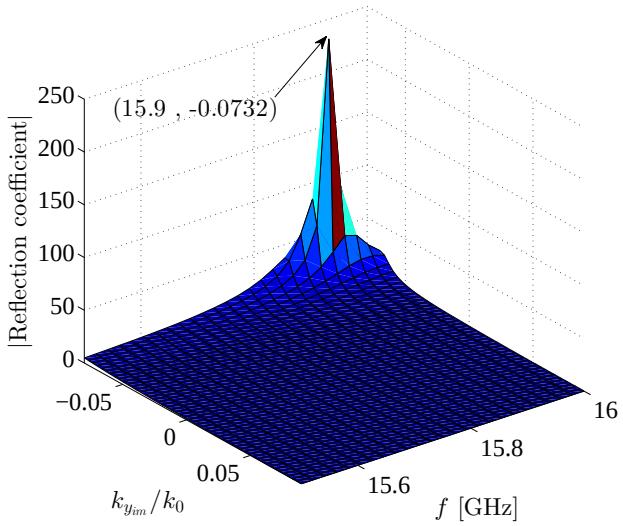

(a) Reflection amplitude

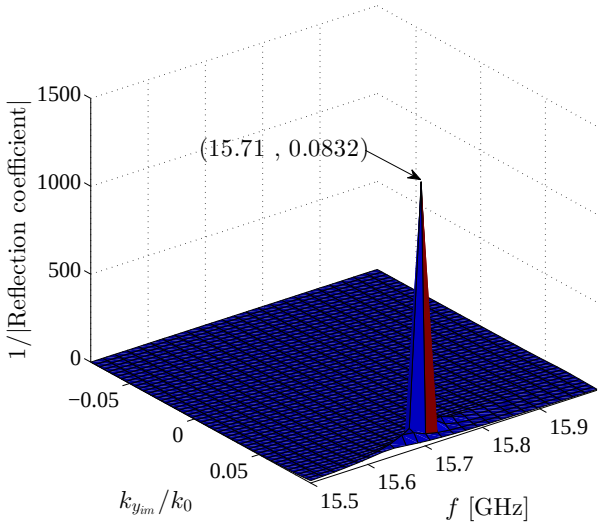

(b) 1/(Reflection amplitude)

Figure 7.22.: Observation of the pole and zero from the scattered field in the fast wave region for incident wavenumber of $k_y/k_0 = 0.75$.

hand, computing the S-parameters, in frequencies where the mode is in the fast wave region, in these periodic structures, will result in very low S_{21} as well as S_{11} which is due to the highly radiating nature of the modes in fast wave region. Therefore, this part of the dispersion diagram is not working as a band gap and can affect he radiation performance of antennas strongly when they are utilized as the artificial grounds. Comparing this dispersion diagram with the one obtained by SMA method, Fig. 4.13, the complex mode resulted from the coupling of the left handed mode with the background mode is removed which is due to the open boundary modeling using the boundary integral method.

7.7. Simulation speed of the FEBI method

To estimate the required time for computing the eigenvalues in every iteration by FEBI method, the number of discretizations for some unit cells and the simulation time for the FEBI method are demonstrated in Tab. 7.1. The computations have been performed on a computer with the system configuration of Intel Core i5 CPU with 3:30 GHz and 8:0 GB RAM.

Simulation speed of FEBI method		
Unit cell configuration	Number of tetrahedra	Simulation time
Grounded slab waveguide	8508	8 sec
Interdigital leaky wave antenna	175517	3.4 min
AMC mushroom	14775	7 sec

Table 7.1.: Simulation time of the FEBI method required for one plane wave excitation.

The speed of the convergence depends on the initial guess and the parameters of the Nelder-Mead acceleration method. For the typical values used in this thesis, usually twenty iterations are enough to have a relative error being less than 10^{-5}.

7.8. Double sided radiating leaky wave antenna

The slab waveguides in free space are media with the possibility to carry the surface waves. However, adding inhomogeneity to the slabs will result in the capability of carrying complex modes. Periodic double sided open structures

are usually employed as superstrate for resonant antennas or lens structures to concentrate the field intensity in a desired point. To investigate the radiation and scattering properties of double sided open periodic structures, we have employed the same procedure for the homogeneous slab waveguides in section 7.2. The periodic unit cell considered is the same as the one in Fig. 7.12 with inversed one of the unit cells. Therefore, as is shown in Fig. 7.23, the total unit cell has slots both at the top and bottom, which make it a transparent in some frequencies and allow the wave to pass through it.

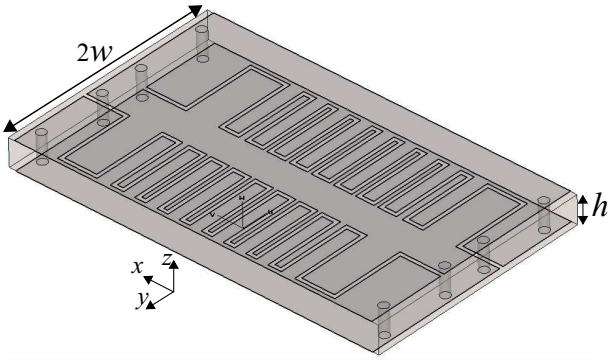

Figure 7.23.: Unit cell of a double sided open leaky wave antenna, h =1.524 mm, l = 20 mm, w = 5.9 mm, r_{via} = 0.25 mm, slot width = 0.2 mm and ε_r = 3.38. The unit cell is periodic in y direction and open in other directions. Along the cell, two interdigital slots one in the top conductor and one in the bottom conductor exist. At every side, four vias connect the top and bottom conductors.

The antenna unit cell has a composite right/left handed behavior between 3 and 6 GHz. The transition frequency is at 3.7 GHz. Since the leaky structure has complex eigenvalues, the excitations are inhomogeneous plane waves. By computing the singularities of reflection or transmission coefficient, the dispersion diagram is computed as in Fig. 7.24. The result from SMA method is computed for four mode excitation. The slight difference between the results is mostly due to the number of tetrahedra for discretizing the unit cell.

In the slow wave region, at 3.05 GHz, the transmission coefficient of the plane wave has been plotted for complex spectrum in Fig. 7.25. Since the swept wavenumbers are after the light line, both complex conjugate poles are observable.

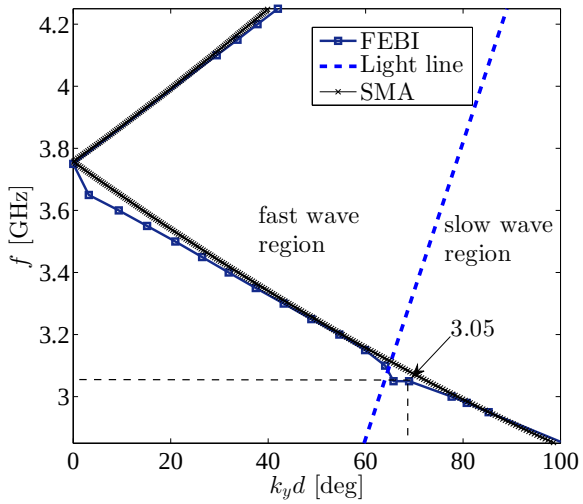

Figure 7.24.: The dispersion diagram of the leaky double sided open structure in Fig. 7.23.

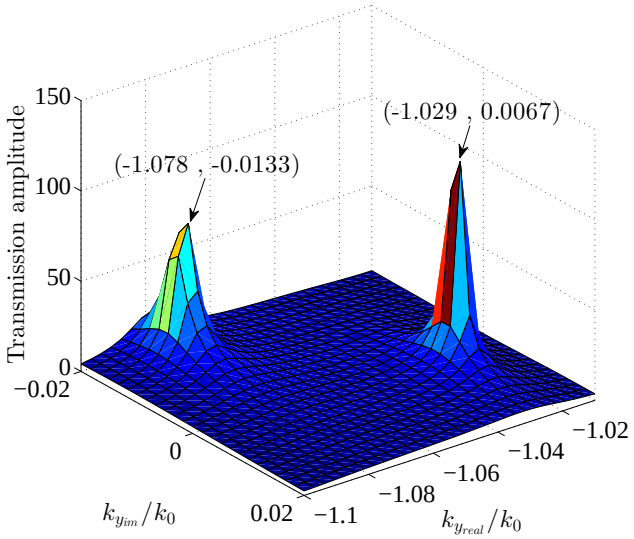

Figure 7.25.: The dispersion diagram of the mushroom structure in Fig. 7.17.

7.8.1. Absorption in double sided open structures

As it was explained, for grounded structures, there is always the point of complete absorption. For two sided open structures, investigation of the zeros of both the reflection and transmission coefficients are needed to be known.

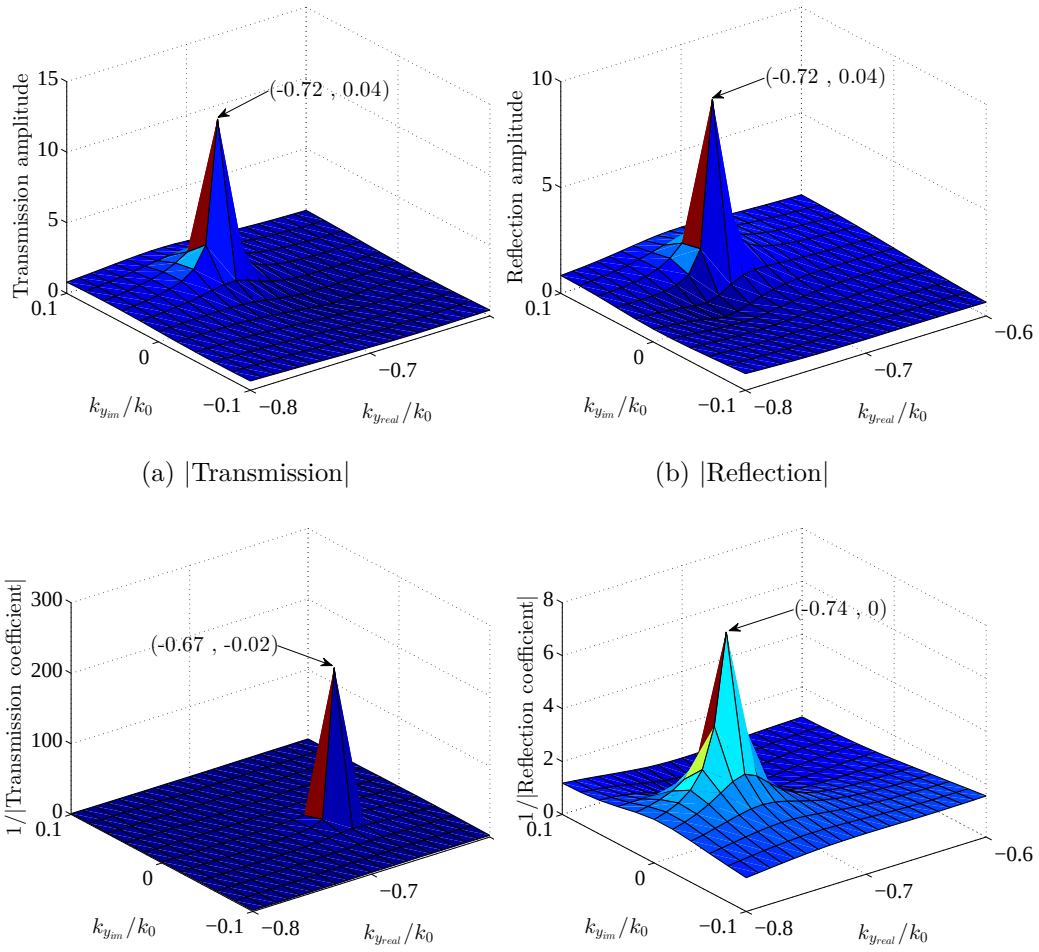

(a) |Transmission| (b) |Reflection|

(c) 1/|Transmission| (d) 1/|Reflection|

Figure 7.26.: The location of poles and zeros in re ection and transmission coefficients from leaky antenna unit cell at 3.25 GHz.

Consider the numerator of the reflection and transmission coefficients of a

slab waveguide in Eq.s (6.17) and (6.18)

$$r(1-\mathrm{e}^{-2\mathrm{j}k_{z1}d}) \quad \text{reflection,} \tag{7.10}$$

$$(1-r^2)\mathrm{e}^{-2\mathrm{j}k_{z1}d} \quad \text{transmission.} \tag{7.11}$$

By a careful attention to the reflection numerator, it is observed that that the zeros of the reflation are at points where $k_{z1}d = n\pi$ which means the zeros are only existing for real value wavenumbers. The transmission coefficient has, on the other hand, zeros where $r^2 = 1$ which are not coincident with the zeros of the reflection. Therefore, it cannot be expected to have complete absorption for lossless non-chiral stratified structures. For periodic structures, we have computed the reflection and transmission coefficients of the leaky unit cell of the Fig. 7.23 at frequency 3.25 GHz. To show the zeros of the reflection and transmission, the inverse of them is also depicted, see Fig. 7.26.

As it is expected the poles of reflection and transmission are at the same locations. Since the mode is left handed at 3.25 GHz, the proper modes are the one with $k_{y_{real}}k_{y_{imag}} > 0$ and the improper one has been rejected by the imposed condition on wavenumbers. Instead, the zeros of the reflection and transmission are observable as shown in Fig.s 7.26d and 7.26c. The zero of the reflection as it was predicted, is on real wavenumbers, while the zero of the transmission is located on complex wavenumbers. To make both zeros coincident and realize the complete absorption there are two methods, adding the loss or chirality to the structure.

7.9. Near field subwavelength super resolution imaging

The other interesting phenomenon in scattering problems is the construction of the image of the non radiating sources. In the first chapter of this thesis, the material properties of the resonant metamaterial particles is investigated. The resonant particle have the dispersion diagram of Lorentz type [Oughstun and Cartwright, 2003, Smith et al., 2005], while a group of other metamaterials are made up of non-resonant unit cells. The dispersion diagram of the non-resonant unit cells is of the Drude type [Simovski et al., 2012].

To analyze the wire medium, we start with a surface wave 1D periodic structure of Fig. 7.27. The structure is made up of an array of metallic plates periodic in y direction with a limited length in z direction and infinite in x direction. The unit cell is excited by evanescent plane waves for $k_y/k_0 = 3$ in Fig. 7.28. As it is considered in this thesis, the unit cell is excited by a TM plane wave with E_y, E_z and H_x components. The field distribution of the excited mode inside the considered unit cell is depicted in Fig. 7.29. For the

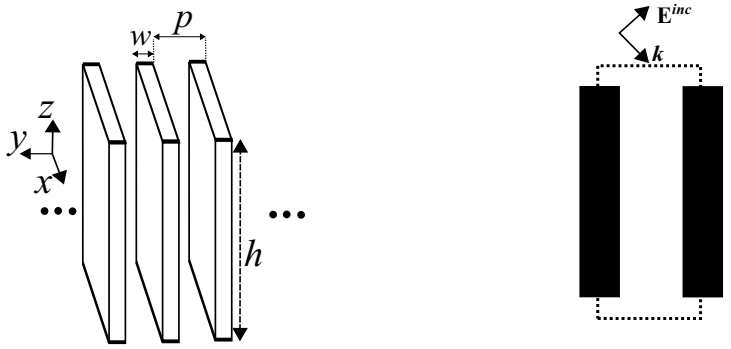

(a) Array of plates (b) Unit cell of the metallic array

Figure 7.27.: An array of metallic plates in free space, unit cell length $p = 3$ mm, $w = 0.2$ mm, $h = 10$ mm and infinite in x direction.

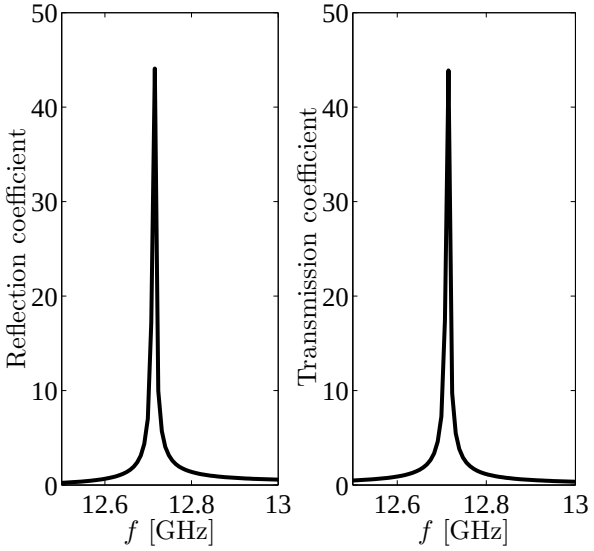

Figure 7.28.: The reflection and transmission coefficients of an incident plane wave with $k_y/k_0 = 3$ onto a unit cell of Fig. 7.27.

field distribution it can be seen that the excited mode inside the unit cell can be as a non-radiating TEM mode. By the method of excitation the dispersion diagram of the first mode of the unit cell is computed as shown in Fig. 7.30. As it is observed, at $\beta d = \pi$, the dispersion curve is becoming flat which is equiv-

alent to an standing wave resonating in z direction. With respect to the field distribution, this structure is ideal for near field imaging applications. However this structure is still 1D and is not the perfect one for near field imaging application.

The result from FEBI computations is compared with the result computed by eigenmode solution in CST MWS. Since the eigenmode solution of CST does not support open boundary conditions, to model the open boundary at the top and bottom of the unit cell, a perfect electric conductor (PEC) boundary condition is considered around $\lambda/4$ away from the metal. However, this spacing strongly affects the eigenvalue and the slight difference between the results from CST and FEBI is because of this distance.

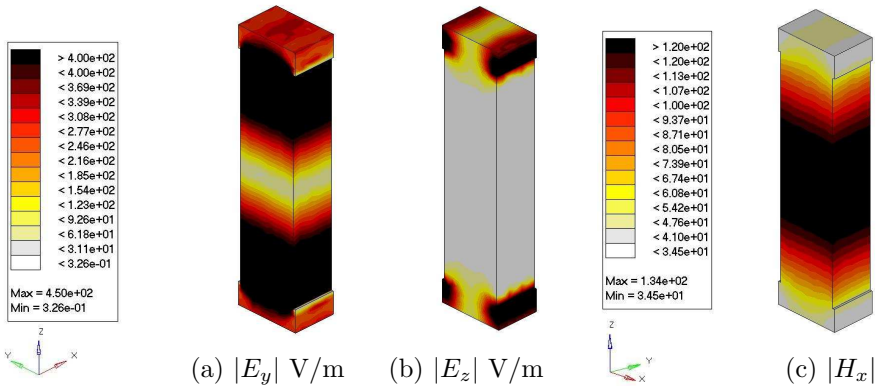

(a) $|E_y|$ V/m (b) $|E_z|$ V/m (c) $|H_x|$ A/m

Figure 7.29.: Distribution of the field in between two metal plates of Fig. 7.27b in free space at 12.72 GHz and k_y/k_0=3.

With respect to the field distribution inside the slits, the best excitation method for this surface wave mode is to put a voltage source in y direction between two plates. The S-parameters of the resulting band pass in Fig. 7.31 show the first and second surface wave modes excited by discrete ports in CST MWS for an array of 11 plates. To truncate the length of the plate in x direction it is enough to set the boundary condition in x direction as perfect magnetic conductor (PMC). The port impedance for the CST simulation by discrete port excitation in Fig. 7.31 is considered as 500 Ohm. As it is observed from the dispersion diagram of Fig. 7.30, the curve is becoming flat around 14.5 GHz which is close to the resonant frequency of a transmission line of length of 10 mm.

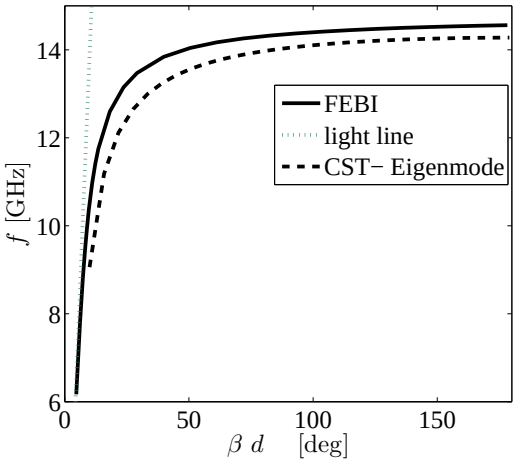

Figure 7.30.: The dispersion diagram of the first mode of the unit cell in Fig. 7.27b with w= 0.4 mm and p = 0.6 mm.

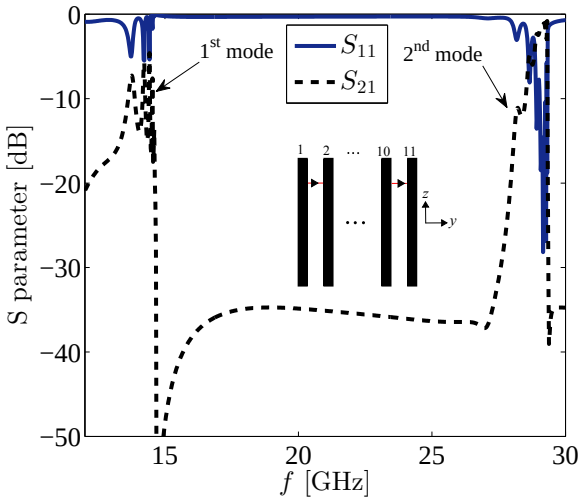

Figure 7.31.: Scattering parameters of periodic arrangement of 11 unit cells of metallic plates excited by discrete ports in CST MWS, w= 0.4 mm, p = 0.6 mm, h = 10 mm.

7.9.1. Wire medium

To extend the 1D array of metallic structures into 2D and enabling the isotropic near field imaging, the wire medium [Belov and Simovski, 2006] is a good candidate. In this purpose, a unit cell is one wire at the center with radius of 1 mm and 15 cm length with period of 1 cm in transverse direction, Fig. 7.32.

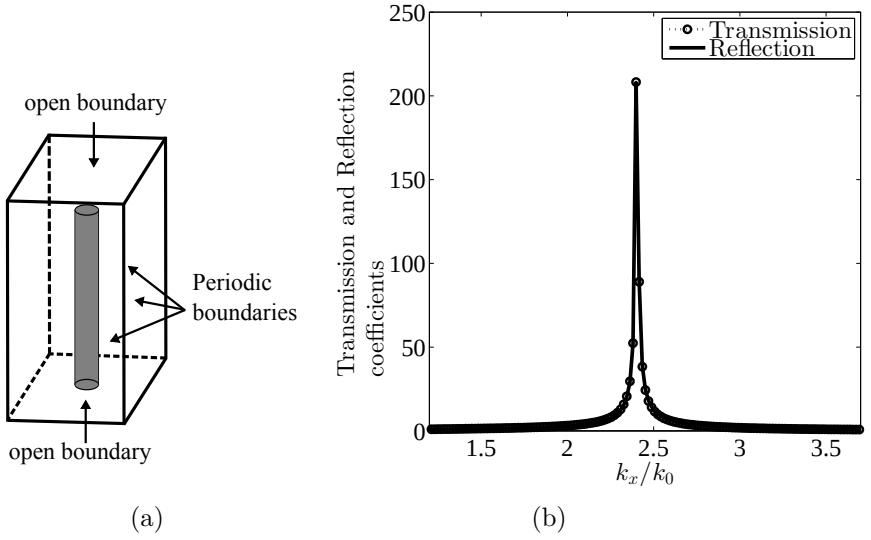

Figure 7.32.: (a) The unit cell of a wire with corresponding boundary conditions with $r_{\text{wire}} = 1$ mm, length = 15 cm and period = 1 cm at frequency 761 MHz, (b) Transmission and reflection coefficients of incident inhomogeneous plane wave for a wire medium unit cell.

The periodic arrangement of the cell creates a slab in free space. This slab supports surface wave modes and to excite the eigenmode, an evanescent plane wave with a tangential wavenumber in x direction is considered with $k_x > k_0$. The reflection and transmission coefficients of the zeroth order Floquet mode are computed and the eigenvalue is derived from the singularities. Transmission and reflection coefficients of the plane wave impinging on the unit cell at the frequency 761 MHz are shown in Fig. 7.32b, which confirm the surface wave mode excitation.

The electric field intensity in one unit cell has been illustrated in Fig. 7.33. As it is observed, the field intensity has a high value at both ends of the wire while the excitation is an evanescent wave. The dispersion diagram of the first two modes in the $\Gamma - X$ path in the Brillouin zone of the dispersion diagram in Fig. 7.34 are compared with the result achieved from a CST Microwave Studio

Eigenmode solution. The slight difference between the FEBI and the CST results is due to the approximation of the open boundary in CST by the PEC boundary with a quarter wavelength distance away from the wire ends what would be justified by the assumption of a bound mode.

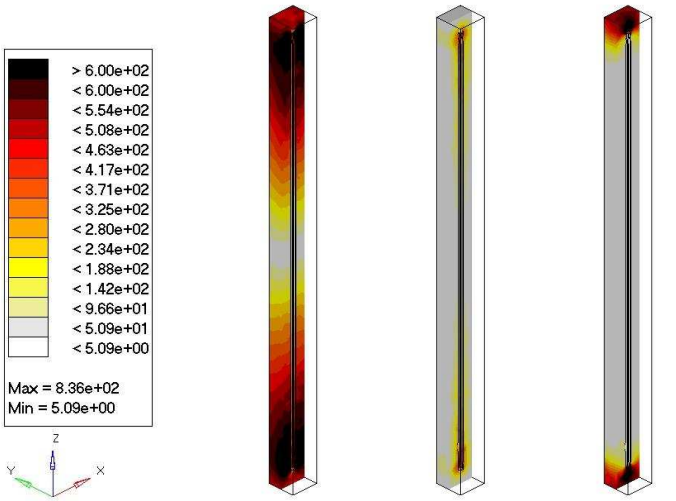

(a) $|E|$ V/m (b) $|E_x|$ (c) $|E_y|$ (d) $|E_z|$

Figure 7.33.: Distribution of electric field (in V/m) in a unit cell of the wire medium in free space at 761 MHz and k_x/k_0=2.4.

Every source placed very close to the surface of a slab of wires will excite evanescent waves as found in the dispersion diagram. These evanescent waves will be amplified according to their eigenvalues. The best resolution of the image reconstruction will be achieved at the end of the Brillouin zone in the dispersion diagram. At this frequency, the wavenumber reaches $k_x a = \pi$ and the dispersion diagram is becoming flat, so that the group velocity is zero while the phase velocity is nonzero. Consequently, there is no surface wave mode but the mode can be considered as a standing wave and the highest resolution is achieved [Simovski et al., 2005].

7.9.2. Slots loaded by resonators

The resonant particles when placed in an electromagnetic field in appropriate configuration can be represented as an effective homogeneous medium described by a single negative material property which is equivalent to a stop band in the direction of wave propagation or a pass band below the cutoff frequency of the host waveguide [Hrabar et al., 2005]. In [Malyuskin and Fusco, 2014], the

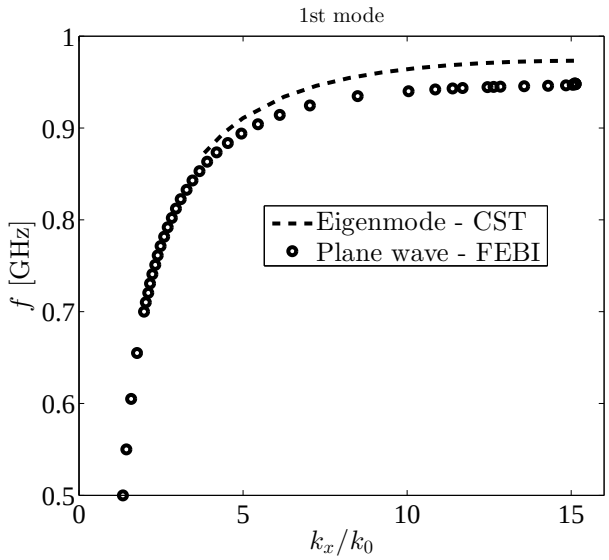

(a) 1^{st} mode

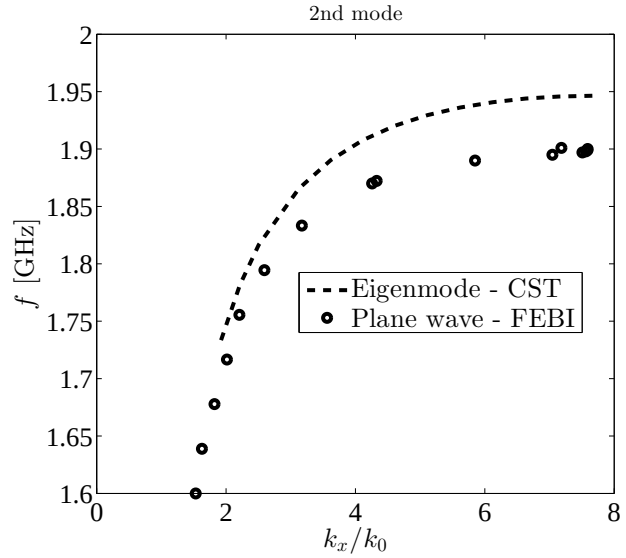

(b) 2^{nd} mode

Figure 7.34.: Two first surface modes of the wire medium computed by proposed method and CST Eigenmode solver.

zero of the reflection coefficient of a loaded slot is considered as the reason for improved imaging capabilities.

In this subsection, the zeros of the reflection in the fast wave region for a general form of slots is investigated to show the exact reason of the near field imaging in slots loaded by resonators. In this regard, we first explore the zeros of a homogeneous slab waveguide. As it was discussed in (7.11), the zeros of the reflection coefficient are occurring at the locations of $k_{z1}d = \pi$ where transmission becomes unity and reflection is zero.

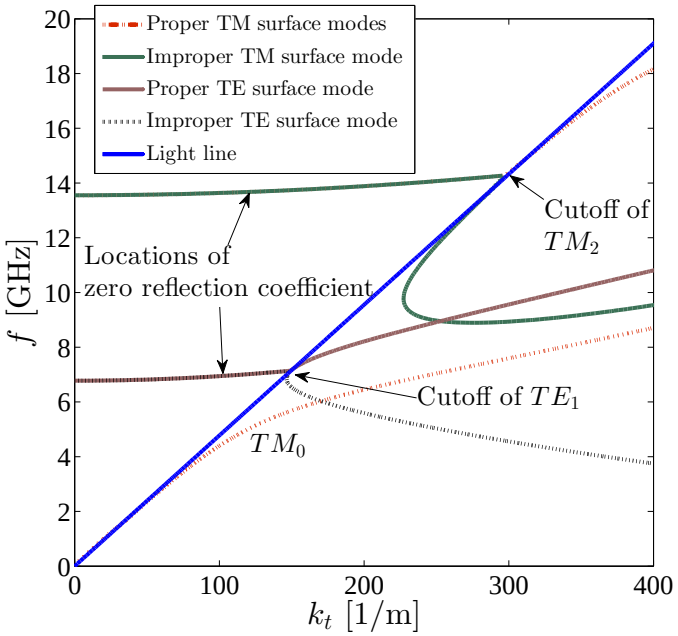

Figure 7.35.: Dispersion diagram of surface modes and the location of zero reflection coefficient in a dielectric slab waveguide with thickness 7 mm and ε_r=10.

On the other hand, for tangential incidence, $k_t = k_0$, the normal wavenumber inside the slab is $k_{z1} = k_0\sqrt{\varepsilon_r - 1}$ which results in $f_c = \frac{nc}{2d\sqrt{\varepsilon_r - 1}}$, c is the velocity of light in free space. This condition is the same as the cutoff condition of surface modes in dielectric slab waveguides.

Therefore, the point at which the reflection coefficient becomes zero for tangential incidence is the same as the cutoff frequency of surface modes. It should be noted, for zero reflection the slab thickness in vertical direction is resonating while at the poles the slab is resonating together with the impedance of the surrounding media producing a guided mode along the slab. Therefore, the zeros of the reflection might be utilized as a tool to indicate the corresponding

surface modes.

The locations of the zero reflection coefficients are observed in the fast wave region in Fig. 7.35. As it is observed the curves of zero reflection meet the dispersion diagram at the cutoff. The slab is resonating both at the poles and zeros. This is the reason why the field distribution for every zero curve is similar to the curve of the corresponding pole inside the slab.

To investigate the slots loaded by resonator, the periodic array of metallic plates in Fig. 7.27 can be considered. As was shown in Fig. 7.29, the magnetic field inside the slot, H_x, has the maximum value at the center. This field distribution can be an appropriate candidate for exciting split ring resonator (SRR) metamaterial particles.

7.9.3. Loading the unit cell by metamaterial resonators

AS it was explained in section 3.3, to compute the resonant frequency of metamaterial particles in a periodic arrangement, usually the TEM field distribution is modeled by PEC/PMC (perfect electric and magnetic) boundary conditions in the transverse directions.

The resonant frequency of a split ring resonator of Fig. 7.36 is computed by the PEC/PMC boundary at 7.4 GHz. The unit cell size in y direction is the same as the metallic plates separation, 3 mm, and in x direction is 5 mm. The reflection coefficient from the unit cell of Fig. 7.27 for both loaded and unloaded by the resonator of Fig. 7.36 is computed in Fig. 7.37 by using the frequency domain analysis of CST Micorwave Studio.

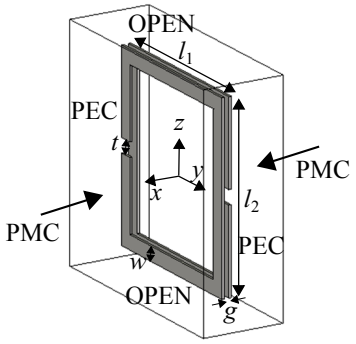

Figure 7.36.: Split ring resonator, $l_1 = 2.4$ mm, $l_2 = 2.6$ mm, $t = 0.2$ mm, $g = 0.066$ mm, $w = 0.2$ mm, metal thickness = 0.034 mm, unit cell dimensions in x and y directions are 5 mm and 3 mm, respectively.

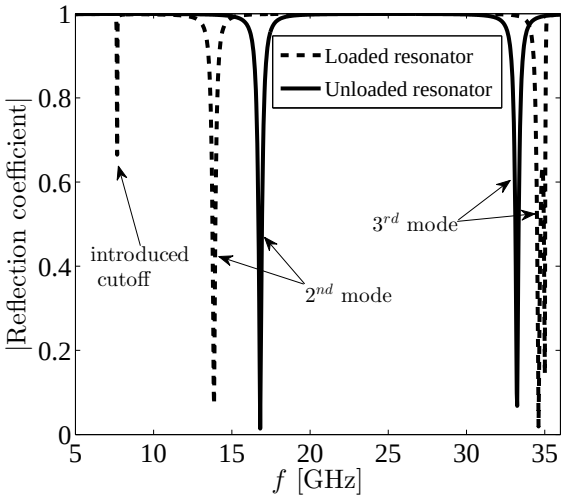

Figure 7.37.: The reflection coefficient of the tangentially incident plane wave with $k_y/k_0 \approx 0$ onto a unit cell of Fig. 7.27 when loaded and unloaded by SRR.

As is shown, the introduced cutoff is at 7.66 GHz. The cutoff of higher order modes is also affected but not strongly. In Fig. 7.38, the dispersion diagram of the first few modes is computed for the loaded and unloaded unit cell by using the Eigenmode solution of CST Microwave Studio. As is depicted, the curves at the end of the Brilluoin zone become flat. In unloaded unit cell, the end frequency of the curves is equivalent to the resonant length of parallel plate transmission line, h in Fig. 7.27, for every mode. The first surface mode in the loaded unit cell has the end frequency of 7.2 GHz and the cutoff of the next mode is at 7.66 GHz which is computed from the reflection coefficient too. Consequently, a band gap is introduced from 7.2 to 7.66 GHz due to SRR. The resulting narrow band surface mode propagating in the x direction has a very flat dispersion behavior and can be utilized for near field imaging at 7.2 GHz.

In resonator loaded applications which are vastly used for reducing the size of cavity resonators [Engheta, 2002a], the purpose of using the resonant particles is to reduce the size of the resonator by introducing a new material parameter. In current paper, it is shown that resonant particles do not strongly disturb the modes of the individual cavity, but they introduce a very narrowband surface mode. However, the field distribution in this new surface mode is very similar to the first mode of the individual open unit cell loaded by resonator, as is shown

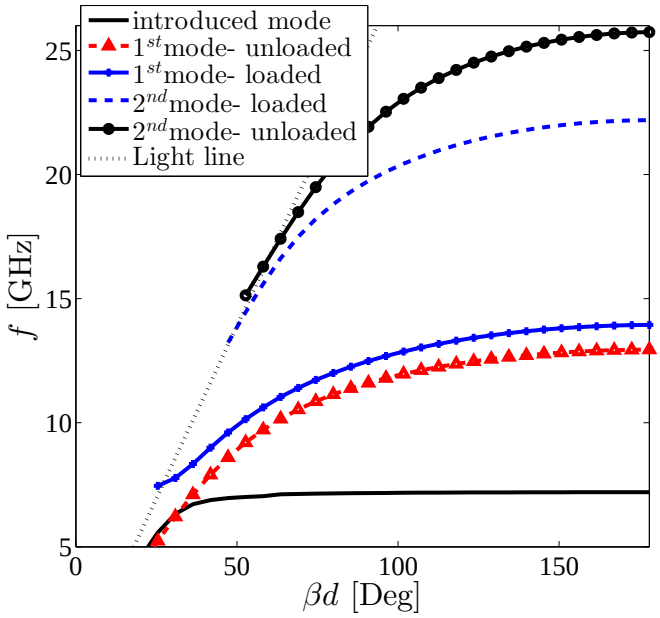

Figure 7.38.: Dispersion diagram of the loaded and unloaded unit cell in Fig. 7.27.

in Fig. 7.39. In Fig. 7.39, the magnetic field distribution of two first modes of the loaded unit cell are shown, which are indicated as the resonant mode of the SRR and the first mode of the waveguide. As it is seen, the magnetic field of SRR mode is very similar to the first mode of the loaded wavegudie. On the other hand, the first mode of the wavegudie does not change strongly due to the loaded resonator. Therefore, it can be concluded that the SRR mode is a new mode introduced to the structure where in the literature it is mentioned as reducing the resonance length in z direction. It should be noted that the transverse spacing between the resonators in y direction affects the dispersion diagram which in this paper a large enough distance, 3 mm, is considered to omit this effect. Consequently, this new surface mode can only be controlled by the resonance frequency of the metamaterial resonator.

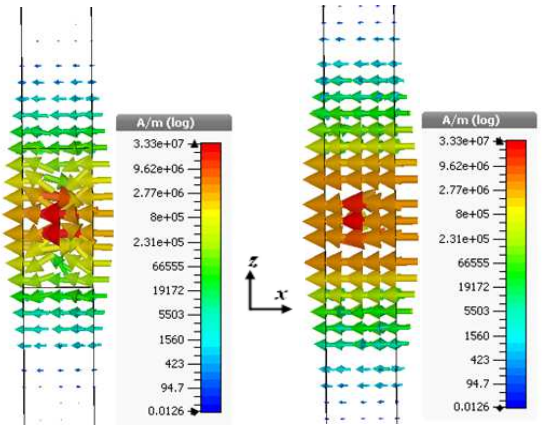

Figure 7.39.: Magnetic field (H_x) distribution of the resonant mode of SRR and first mode of the periodic plates inside the unit cell loaded by SRR, left: SRR resonant mode (f = 7.2 GHz), right: first mode of the loaded waveguide (f = 13.93 GHz).

A. Appendix

A.1. Nelder-Mead

The simplex Nelder-Mead compares function values at the three vertices of a triangle and rejects the worst vertex over which the function has the largest value and replaces it with a new value [Nelder and Mead, 1965]. The new triangle is formed and the search is continued until the threshold for the error is met. For a function of N variables, the generalized triangle in N dimension is formed.

To start, three vertices of a triangle are given. The function $f(x, y)$ is then evaluated on three points: $z_k = f(x_k, y_k)$ for $k = 1, 2, 3$. By reordering the subscripts for the best to worst value one has

$$\boldsymbol{B} = (x_1, y_1), \quad \boldsymbol{G} = (x_2, y_2), \quad \boldsymbol{W} = (x_3, y_3) \tag{A.1}$$

such that $\boldsymbol{B}$ is the best point, $\boldsymbol{G}$ is good and $\boldsymbol{W}$ is the worst point.

Th mid point of the good side is defined as

$$\boldsymbol{M} = \frac{\boldsymbol{B} + \boldsymbol{G}}{2} = \left(\frac{x_1 + x_2}{2}, \frac{y_1 + y_2}{2} \right). \tag{A.2}$$

A.1.1. Reflection

Since the function decreases from $\boldsymbol{W}$ towards $\boldsymbol{B}$ and $\boldsymbol{G}$ along the triangle edges, it is desired to move away from the $\boldsymbol{W}$ point. Therefore the reflection point $\boldsymbol{R}$ is defined as the reflection of $\boldsymbol{W}$ with respect to the midpoint of the line $\overline{BG}$ which is the new vertex to be utilized instead of $\boldsymbol{W}$. The vector formula for $\boldsymbol{R}$ is

$$\boldsymbol{R} = 2\boldsymbol{M} - \boldsymbol{W}. \tag{A.3}$$

A.1.2. Expansion

If the function in $\boldsymbol{R}$ has a smaller value than the value in $\boldsymbol{W}$ then the algorithm is moving towards the minimum in the right direction. Therefore, the vertex

$\boldsymbol{R}$ is moved further away in that direction to the point $\boldsymbol{E}$ by the same length as $\overline{MR}$

$$\boldsymbol{E} = 2\boldsymbol{R} - \boldsymbol{M}. \tag{A.4}$$

A.1.3. Contraction

If the function has the same values at $\boldsymbol{R}$ and $\boldsymbol{W}$ then a new point has to be tested. The point $\boldsymbol{M}$ cannot be considered as a vertex since then $\boldsymbol{BMG}$ is not making any triangle. Two midpoints c_1 and c_2 of two line segments $\overline{WM}$ and $\overline{MR}$. The point with the lowest function value is named as $\boldsymbol{C}$. Then the new triangle is $\boldsymbol{BGC}$.

A.1.4. Shrink

If the unction value at $\boldsymbol{C}$ is not less than the value at $\boldsymbol{W}$ then the points $\boldsymbol{G}$ and $\boldsymbol{W}$ are shrunk toward $\boldsymbol{B}$. In this regard, $\boldsymbol{G}$ is replaced with $\boldsymbol{M}$ and $\boldsymbol{W}$ is replaced with $\boldsymbol{S}$ which is the midpoint of $\overline{BW}$.

The schematic representations of these operations are shown in Fig. A.1.

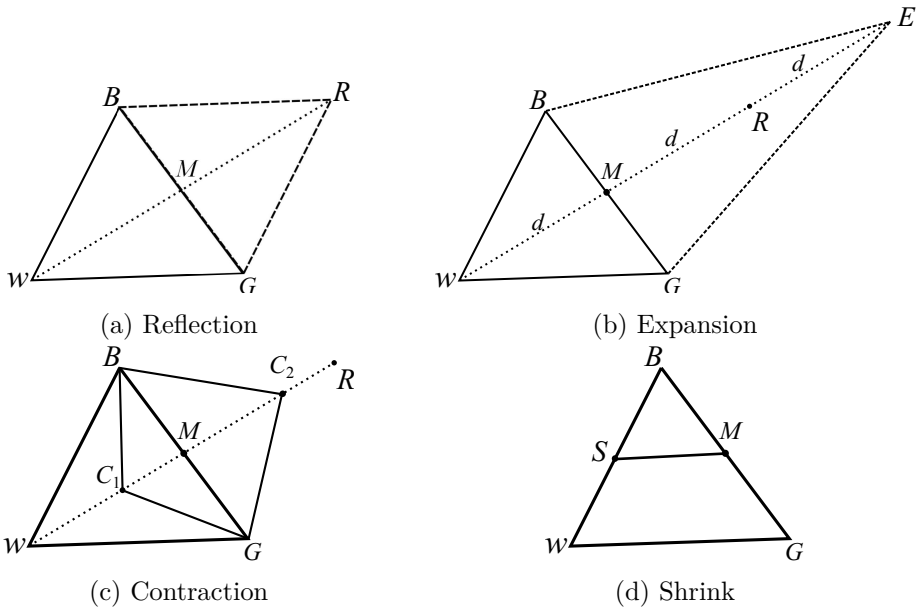

(a) Reflection (b) Expansion

(c) Contraction (d) Shrink

Figure A.1.: Four triangle construction methods for searching by the Nelder-Mead method.

The speed of Nelder-Mead method can be modified by four parameters in four triangle construction methods. coefficients are

1. ρ : reflection coefficient, applied to the reflection of the point as

$$\boldsymbol{R} = \boldsymbol{M} + \rho(\boldsymbol{M} - \boldsymbol{W}). \tag{A.5}$$

2. κ : expansion coefficient, applied to the expansion of the point as

$$\boldsymbol{E} = \boldsymbol{M} + \kappa(\boldsymbol{R} - \boldsymbol{M}) = \boldsymbol{M}(1 + \kappa\rho) - \kappa\rho\boldsymbol{W}. \tag{A.6}$$

3. γ : contraction coefficient, there are two types of contractions depending on the location of point $\boldsymbol{C}$.
   a) Inside contraction

$$\boldsymbol{C} = \boldsymbol{M} - \gamma(\boldsymbol{M} - \boldsymbol{W}). \tag{A.7}$$

   b) Outside contraction

$$\boldsymbol{C} = \boldsymbol{M} + \gamma(\boldsymbol{R} - \boldsymbol{M}). \tag{A.8}$$

4. σ : Shrink coefficient, applied to the shrinking of the triangle as

$$\boldsymbol{S} = \boldsymbol{W} + \sigma(\boldsymbol{B} - \boldsymbol{W}). \tag{A.9}$$

The standard values for the Nelder-Mead algorithm are

$$\rho = 1, \kappa = 2, \gamma = 1/2, \sigma = 1/2. \tag{A.10}$$

A.2. Newton-Raphson iteration

The Newton-Raphson iteration method is a method for solving a system of nonlinear equations. This method can be generalized to a multivariate case to solve n algebraic equations simultaneously as

$$\begin{cases} f_1(x_1, x_2, \ldots, x_n) = f_1(\boldsymbol{x}) = 0, \\ f_n(x_1, x_2, \ldots, x_n) = f_n(\boldsymbol{x}) = 0. \end{cases} \tag{A.11}$$

where $\boldsymbol{x} = [x_1, x_2, \ldots, x_n]^T$ is the vector of n variables. Then the Newton-Raphson formula for multivariate function is

$$\boldsymbol{x} \Leftarrow \boldsymbol{x} - J_f^{-1}(\boldsymbol{x}) f(\boldsymbol{x}). \tag{A.12}$$

where J_f is the Jacobin of function f

$$J_f(\boldsymbol{x}) = \begin{bmatrix} \frac{\partial f_1}{\partial x_1} & \cdots & \frac{\partial f_1}{\partial x_n} \\ \cdots & \cdots & \cdots \\ \frac{\partial f_n}{\partial x_1} & \cdots & \frac{\partial f_n}{\partial x_n} \end{bmatrix}. \tag{A.13}$$

To derive this equation, the higher order terms of the following Taylor expansion are ignored

$$f_i(\boldsymbol{x} + \delta\boldsymbol{x}) = f_i(\boldsymbol{x}) + \sum_j \frac{\partial f_i}{\partial x_j} \delta x_j + \mathcal{O}\delta(\boldsymbol{x}^2), \quad (i = 1, 2, \ldots, n). \tag{A.14}$$

References

Alu, A. and Engheta, N. (2008). Plasmonic and metamaterial cloaking: physical mechanisms and potentials. *Journal of Optics A: Pure and Applied Optics*, 10(9):093002.

Bandlow, B., Schuhmann, R., Lubkowski, G., and Weiland, T. (2008). Analysis of single-cell modeling of periodic metamaterial structures. *IEEE Transactions on Magnetics*, 44(6):1662–1665.

Belov, P. A. and Simovski, C. (2006). Sub-wavelength metallic waveguides loaded by uniaxial resonant scatterers. In *IEEE Mediterranean Electrotechnical Conference, 2006. MELECON 2006.*, pages 229–232.

Belov, P. A. and Simovski, C. R. (2005). Subwavelength metallic waveguides loaded by uniaxial resonant scatterers. *Phys. Rev. E*, 72:036618.

Bongard, F., Perruisseau-Carrier, J., and Mosig, J. (2009). Enhanced periodic structure analysis based on a multiconductor transmission line model and application to metamaterials. *IEEE Transactions on Microwave Theory and Techniques*, 57(11):2715–2726.

Cakoni, F. and Haddar, H. (2012). Transmission eigenvalues in inverse scattering theory. *Inside Out II*, 60:527–578.

Caloz, C. and Itoh, T. (2004). Transmission line approach of left-handed (lh) materials and microstrip implementation of an artificial lh transmission line. *IEEE Transactions on Antennas and Propagation*, 52(5):1159–1166.

Caloz, C. and Itoh, T. (2005). *Electromagnetic metamaterials: transmission line theory and microwave applications*. John Wiley & Sons.

Cao, Q., Lalanne, P., and Hugonin, J.-P. (2002). Stable and efficient bloch-mode computational method for one-dimensional grating waveguides. *J. Opt. Soc. Am. A*, 19(2):335–338.

Chen, Y. (1989). A mathematical formulation of the equivalence principle. *IEEE Transactions on Microwave Theory and Techniques*, 37(10):1576–1581.

Chew, W. C., Jin, J. M., and Michielssen, E. (1997). Complex coordinate stretching as a generalized absorbing boundary condition. *Microwave and Optical Technology Letters*, 15(6):363–369.

Chew, W. C. and Weedon, W. H. (1994). A 3d perfectly matched medium from modified maxwell's equations with stretched coordinates. *Microwave and Optical Technology Letters*, 7(13):599–604.

Clarricoats, P. and Slinn, K. (1965). Complex modes of propagation in dielectric-loaded circular waveguide. *Electronics Letters*, 1(5):145–146.

Clarricoats, P. and Taylor, B. (1964). Evanescent and propagating modes of dielectric-loaded circular waveguide. *Proceedings of the Institution of Electrical Engineers*, 111(12):1951–1956.

Collin, R. E. (1991). *Field theory of guided waves.* Wiley-IEEE Press.

CST (2014). Computer Simulation Technology: Microwave Studio.

Derudder, H., Olyslager, F., De Zutter, D., and Van den Berghe, S. (2001a). Efficient mode-matching analysis of discontinuities in finite planar substrates using perfectly matched layers. *IEEE Transactions on Antennas and Propagation*, 49(2):185–195.

Derudder, H., Olyslager, F., De Zutter, D., and Van den Berghe, S. (2001b). Efficient mode-matching analysis of discontinuities in finite planar substrates using perfectly matched layers. *IEEE Transactions on Antennas and Propagation*, 49(2):185–195.

Dudley, D. G. (1994). *Mathematical foundations for electromagnetic theory.* IEEE press New York.

Dural, G. and Aksun, M. (1995). Closed-form green's functions for general sources and stratified media. *IEEE Transactions on Microwave Theory and Techniques*, 43(7):1545–1552.

Eibert, T. and Hansen, V. (1995). On the calculation of potential integrals for linear source distributions on triangular domains. *IEEE Transactions on Antennas and Propagation*, 43(12):1499–1502.

Eibert, T., Volakis, J., Wilton, D., and Jackson, D. (1999). Hybrid fe/bi modeling of 3-d doubly periodic structures utilizing triangular prismatic elements and an mpie formulation accelerated by the ewald transformation. *IEEE Transactions on Antennas and Propagation*, 47(5).

Eibert, T. F. (1997). *Verknüpfung der Methode der Finiten Elemente mit einem Integralgleichungsverfahren für ebene geschichtete Strukturen.* PhD thesis, Bergischen Universität/Gesamthochschule Wuppertal.

Eibert, T. F., Weitsch, Y., Chen, H., and Gruber, M. (2012). Solving periodic eigenproblems by solving corresponding excitation problems in the domain of the eigenvalue. *Progress In Electromagnetics Research*, 126:65–84.

Eleftheriades, G., Iyer, A., and Kremer, P. (2002). Planar negative refractive index media using periodically l-c loaded transmission lines. *IEEE Transactions on Microwave Theory and Techniques*, 50(12):2702–2712.

Engheta, N. (2002a). An idea for thin subwavelength cavity resonators using metamaterials with negative permittivity and permeability. *Antennas and Wireless Propagation Letters, IEEE*, 1(1):10–13.

Engheta, N. (2002b). Thin absorbing screens using metamaterial surfaces. In *IEEE Antennas and Propagation Society International Symposium*, volume 2, pages 392–395 vol.2.

Engheta, N., Alu, A., Silveirinha, M. G., Salandrino, A., and Li, J. (2006). Dng, sng, enz and mnz metamaterials and their potential applications. In *IEEE Mediterranean Electrotechnical Conference, MELECON 2006.*, pages 258–261. IEEE.

Fang, D., Yang, J., and Delisle, G. (1988). Discrete image theory for horizontal electric dipoles in a multilayered medium. *IEE Proceedings H, Microwaves, Antennas and Propagation*, 135(5):297–303.

Felsen, L. B. and Marcuvitz, N. (1994). *Radiation and scattering of waves*, volume 31. John Wiley & Sons.

Gedney, S. D. (1996). An anisotropic pml absorbing media for the fdtd simulation of fields in lossy and dispersive media. *Electromagnetics*, 16(4):399–415.

Graglia, R. (1993). On the numerical integration of the linear shape functions times the 3-d green's function or its gradient on a plane triangle. *IEEE Transactions on Antennas and Propagation*, 41(10):1448–1455.

Grbic, A. and Eleftheriades, G. V. (2005). An isotropic three-dimensional negative-refractive-index transmission-line metamaterial. *Journal of Applied Physics*, 98(4):–.

Hanson, G. W. and Yakovlev, A. B. (1998). An analysis of leaky-wave dispersion phenomena in the vicinity of cutoff using complex frequency plane singularities. *Radio Science*, 33(4):803–819.

Harrington, R. F. (1961). *Time harmonic electromagnetic fields*. McGraw-Hill.

Harrington, R. F. and Harrington, J. L. (1996). *Field computation by moment methods*. Oxford University Press.

HFSS (2014). 3-D Electromagnetic Simulation Software. Ansoft corp.,Pittsburgh, PA.

Hrabar, S., Bartolic, J., and Sipus, Z. (2005). Waveguide miniaturization using uniaxial negative permeability metamaterial. *IEEE Transactions on Antennas and Propagation*, 53(1):110–119.

Hua, Y. and Sarkar, T. (1989). Generalized pencil-of-function method for extracting poles of an em system from its transient response. *IEEE Transactions on Antennas and Propagation*, 37(2):229–234.

Islam, R. and Eleftheriades, G. (2010). On the independence of the excitation of complex modes in isotropic structures. *IEEE Transactions on Antennas and Propagation*, 58(5):1567–1578.

Jin, J. (2014). *The finite element method in electromagnetics*. John Wiley & Sons.

Kunz, K. S. and Luebbers, R. J. (1993). *The finite difference time domain method for electromagnetics*. CRC press.

Ling, F. and Jin, J.-M. (2000). Discrete complex image method for green's functions of general multilayer media. *IEEE Microwave and Guided Wave Letters*, 10(10):400–402.

Maci, S., Caiazzo, M., Cucini, A., and Casaletti, M. (2005). A pole-zero matching method for ebg surfaces composed of a dipole fss printed on a grounded dielectric slab. *IEEE Transactions on Antennas and Propagation*, 53(1):70–81.

Malyuskin, O. and Fusco, V. (2014). Near field enhancement and subwavelength imaging using resonantly loaded apertures. *IEEE Transactions on Antennas and Propagation*, 62(6):3130–3140.

Matthaei, G. L., Young, L., and Jones, E. M. (1963). *Microwave Filters, Impedance-Matching Networks, and Coupling Structures*. McGraw-Hill.

Mautz, J. R. and Harrington, R. F. (1977). H-field, e-field, and combined field solutions for bodies of revolution. Technical report, DTIC Document.

McGrath, D. and Pyati, V. (1994). Phased array antenna analysis with the hybrid finite element method. *IEEE Transactions on Antennas and Propagation*, 42(12):1625–1630.

Michalski, K. and Zheng, D. (1990). Electromagnetic scattering and radiation by surfaces of arbitrary shape in layered media. i. theory. *IEEE Transactions on Antennas and Propagation*, 38(3):335–344.

Mittra, R., Hou, Y.-L., and Jamnejad, V. (1980). Analysis of open dielectric waveguides using mode-matching technique and variational methods. *IEEE Transactions on Microwave Theory and Techniques*, 28(1):36–43.

Nelder, J. A. and Mead, R. (1965). A simplex method for function minimization. *The computer journal*, 7(4):308–313.

Oliner, A. (2003). A planar negative-refractive-index medium without resonant elements. In *IEEE MTT-S International Microwave Symposium Digest, 2003*, volume 1, pages 191–194 vol.1.

Olyslager, F. (2004). Discretization of continuous spectra based on perfectly matched layers. *SIAM Journal on Applied Mathematics*, 64(4):1408–1433.

Omar, A. and Schonemann, K. (1986). Formulation of the singular integral equation technique for planar transmission lines (correction). *IEEE Transactions on Microwave Theory and Techniques*, 34(1):196–196.

Oughstun, K. and Cartwright, N. (2003). On the lorentz-lorenz formula and the lorentz model of dielectric dispersion. *Optics express*, 11(13):1541–1546.

Pendry, J., Holden, A., Robbins, D., and Stewart, W. (1999). Magnetism from conductors and enhanced nonlinear phenomena. *IEEE Transactions on Microwave Theory and Techniques*, 47(11):2075–2084.

Pendry, J., Holden, A., Stewart, W., and Youngs, I. (1996). Extremely low frequency plasmons in metallic mesostructures. *Physical review letters*, 76(25):4773.

Pendry, J., Smith, D., and Schurig, D. (2008). Electromagnetic cloaking method. US Patent App. 11/459,728.

Peterson, A. F., Ray, S. L., Mittra, R., of Electrical, I., and Engineers, E. (1998). *Computational methods for electromagnetics*, volume 2. IEEE press New York.

Rao, S., Wilton, D., and Glisson, A. (1982). Electromagnetic scattering by surfaces of arbitrary shape. *IEEE Transactions on Antennas and Propagation*, 30(3):409–418.

Reutskiy, S. (2010). The method of external excitation for solving generalized sturm liouville problems. *Journal of Computational and Applied Mathematics*, 233(9):2374 – 2386.

Reutskiy, S. Y. (2008). The methods of external excitation for analysis of arbitrarily shaped hollow conducting waveguides. *Progress In Electromagnetics Research*, 82:203–226.

Rogier, H. and De Zutter, D. (2001). Berenger and leaky modes in microstrip substrates terminated by a perfectly matched layer. *IEEE Transactions on Microwave Theory and Techniques*, 49(4):712–715.

Rozzi, T., Pierantoni, L., and Farina, M. (1998). General constraints on the propagation of complex waves in closed lossless isotropic waveguides. *IEEE Transactions on Microwave Theory and Techniques*, 46(5):512–516.

Schurig, D., Mock, J. J., Justice, B. J., Cummer, S. A., Pendry, J. B., Starr, A. F., and Smith, D. R. (2006a). Metamaterial electromagnetic cloak at microwave frequencies. *Science*, 314(5801):977–980.

Schurig, D., Mock, J. J., and Smith, D. R. (2006b). Electric-field-coupled resonators for negative permittivity metamaterials. *Applied Physics Letters*, 88(4).

Shelby, R. A., Smith, D. R., Nemat-Nasser, S. C., and Schultz, S. (2001a). Microwave transmission through a two-dimensional, isotropic, left-handed metamaterial. *Applied Physics Letters*, 78(4).

Shelby, R. A., Smith, D. R., and Schultz, S. (2001b). Experimental verification of a negative index of refraction. *science*, 292(5514):77–79.

Sheng, X., Jin, J.-M., Song, J., Chew, W. C., and Lu, C.-C. (1998). Solution of combined-field integral equation using multilevel fast multipole algorithm for scattering by homogeneous bodies. *IEEE Transactions on Antennas and Propagation*, 46(11):1718–1726.

Sievenpiper, D., Zhang, L., Broas, R., Alexopolous, N., and Yablonovitch, E. (1999). High-impedance electromagnetic surfaces with a forbidden frequency band. *IEEE Transactions on Microwave Theory and Techniques*, 47(11):2059–2074.

Sihvola, A., Tretyakov, S., and de Baas, A. (2007). Metamaterials with extreme material parameters. *Journal of Communications Technology and Electronics*, 52(9):986–990.

Silveirinha, M. and Engheta, N. (2006). Tunneling of electromagnetic energy through subwavelength channels and bends using ϵ-near-zero materials. *Physical review letters*, 97:157403.

Silvester, P. and Hsieh, M.-S. (1971). Finite-element solution of 2-dimensional exterior-field problems. *Proceedings of the Institution of Electrical Engineers*, 118(12):1743–1747.

Simovski, C. R. (2011). On electromagnetic characterization and homogenization of nanostructured metamaterials. *Journal of Optics*, 13(1):013001.

Simovski, C. R., Belov, P. A., Atrashchenko, A. V., and Kivshar, Y. S. (2012). Wire metamaterials: Physics and applications. *Advanced Materials*, 24(31):4229–4248.

Simovski, C. R., Viitanen, A. J., and Tretyakov, S. A. (2005). Resonator mode in chains of silver spheres and its possible application. *Phys. Rev. E*, 72:066606.

Sjöberg, D., Engström, C., Kristensson, G., Wall, D. J., and Wellander, N. (2005). A floquet–bloch decomposition of maxwell's equations applied to homogenization. *Multiscale Modeling & Simulation*, 4(1):149–171.

Smith, D. R., Padilla, W. J., Vier, D. C., Nemat-Nasser, S. C., and Schultz, S. (2000a). Composite medium with simultaneously negative permeability and permittivity. *Phys. Rev. Lett.*, 84:4184–4187.

Smith, D. R., Vier, D. C., Koschny, T., and Soukoulis, C. M. (2005). Electromagnetic parameter retrieval from inhomogeneous metamaterials. *Phys. Rev. E*, 71:036617.

Smith, D. R., Vier, D. C., Kroll, N., and Schultz, S. (2000b). Direct calculation of permeability and permittivity for a left-handed metamaterial. *Applied Physics Letters*, 77(14).

So, P., Du, H., and Hoefer, W. (2005). Modeling of metamaterials with negative refractive index using 2-d shunt and 3-d scn tlm networks. *IEEE Transactions on Microwave Theory and Techniques*, 53(4):1496–1505.

Solbach, K. and Wolff, I. (1978). The electromagnetic fields and the phase constants of dielectric image lines. *IEEE Transactions on Microwave Theory and Techniques*, 26(4):266–274.

Sommerfeld, A. (1949). *Partial differential equations in physics*, volume 1. Academic press.

Szabo, Z., Park, G.-H., Hedge, R., and Li, E.-P. (2010). A unique extraction of metamaterial parameters based on kramers-kronig relationship. *IEEE Transactions on Microwave Theory and Techniques*, 58(10):2646–2653.

Taflove, A. and Hagness, S. C. (2005). *Computational electrodynamics*. Artech house.

Tzoulis, A. (2009). *Numerical modeling of electromagnetic problems with the hybrid finite element - boundary integral - multilevel fast multipole - uniform geometrical theory of diffraction method*. PhD thesis, Technischen Universität Darmstadt.

Valerio, G., Paulotto, S., Baccarelli, P., Burghignoli, P., and Galli, A. (2011). Accurate bloch analysis of 1-d periodic lines through the simulation of truncated structures. *IEEE Transactions on Antennas and Propagation*, 59(6):2188–2195.

Veselago, V. and Narimanov, E. (2006). The left hand of brightness: past, present and future of negative index materials. *Nature materials*, 5(10):759–762.

Veselago, V. G. (1968). The electrodynamics of substances with simulaneously negative values of ϵ and μ. *Physics-Uspekhi*, 10(4):509–514.

Weitsch, Y. and Eibert, T. (2010). Composite right-/left-handed interdigital leaky-wave antenna on a substrate integrated waveguide. In *Antennas and Propagation (EuCAP), 2010 Proceedings of the Fourth European Conference on*, pages 1–5.

Weitsch, Y. and Eibert, T. (2011). Eigenvalue computation of open periodically composed waveguides by series expansion. In *2011 IEEE International Symposium on Antennas and Propagation (APSURSI)*, pages 321–324.

Wilton, D., Rao, S., Glisson, A., Schaubert, D., Al-Bundak, O., and Butler, C. (1984). Potential integrals for uniform and linear source distributions on polygonal and polyhedral domains. *IEEE Transactions on Antennas and Propagation*, 32(3):276–281.

Xu, F., Zhang, Y., Hong, W., Wu, K., and Cui, T. J. (2003). Finite-difference frequency-domain algorithm for modeling guided-wave properties of substrate integrated waveguide. *IEEE Transactions on Microwave Theory and Techniques*, 51(11):2221–2227.

Yla-Oijala, P. and Taskinen, M. (2003). Calculation of cfie impedance matrix elements with rwg and n times;rwg functions. *IEEE Transactions on Antennas and Propagation*, 51(8):1837–1846.